Fabrication of transition-metal oxide thin films with atomically smooth surface for spintronics application

Tomohiko Matoba

2013

Contents

General Introduction

G.1 Background

There is no other era than today when people have recognized the importance and significant influence of ‘information’. Thanks to the recent developments in the internet and mobile phone system, people can know what is happening in the world anytime-anywhere, and communicate their families or friends immediately even if they live abroad. Digital multimedia, in which information is represented by the assemble of discrete value such as “0” or “1” bit, can avoid noises and deterioration of recorded information in contrast to previous analog system. This enables one to enjoy much clearer and beautiful music, pictures, movies and so on. There is no questions that today’s information technology has contributed to the better quality of human life.

Up to the present, the enormous efforts have been dedicated to these developments in information technology by researchers and manufacturers, and they have often overcome the problems in their products and technologies. For example, in semiconductor field, the well-known ‘Moore’s Law’, in which the integration density of transistor tends to double in almost every 18 months, sometimes has faced the limit of increasing the integrate density and it has been said that it is impossible to maintain further growth. However, thanks to the manufactures’ great efforts to create advanced microfabrication processes including photolithography and dicing finer year by year, Moore’s Law could endure up to now.

In addition to the improvements in manufacture engineering fields, much exertion also has been made to find or create novel materials and phenomena which enable devices to handle much more information and have further added value. Among various kinds of them, today’s solid-state physics in metal oxides, especially transition-metal oxides, has attracted considerable attention of researchers all over the world. So far, many interesting and/or useful materials and phenomena from a point of view of applied physics have been found, and some of them have been already in practical use in the field of electronics. For example, indium-tin-oxide (ITO)

is widely utilized as transparent conductive films in flat-screen televisions and display panels of various kinds of electronic devices including computers, mobile phones, video game machines, and so on [1, 2]. Ferroelectric materials such as $BaTiO_3$, $Pb(Zr_x, Ti_{1-x})O_3$ and $LiNbO_3$ are utilized as capacitors as well as piezoelectric sensor such as actuators and speakers. In addition, an attempt has been made to apply the materials as ferroelectric random access memory due to their large electric polarization [3, 4]. Ferrites AFe_2O_4 (A = Mn, Ni, Cu, Zn, etc.) are magnetic core materials of transformers because their high magnetic permeability and high electric resistivity resulting in smaller eddy-current loss [5].

As mentioned above, the development of practicable metal oxides is indispensable for better human life, and researchers have tried to find novel phenomena and materials in order to contribute to the further development of practical devices. Above all, the discovery of high-temperature superconductors has triggered the intense researches toward the electronics devices based on metal oxides. In 1986, Bednorz and Müller found that cuprate Ba–La–Cu–O system is converted into superconducting phase at 30 K [6] which is higher than the transition temperature (T_C) of existing metals or alloys (e.g. 23 K of Nb_3Ge [7]). After their report, the interest in superconducting oxides has soared, and subsequently, cuprate Y–Ba–Cu–O system (YBCO) was found to exhibit T_C of 93 K by Wu *et al.* in 1987 [8]. The T_C of YBCO, that is higher than liquid nitrogen temperature (77 K), impelled many researchers to search for new superconducting oxides with higher T_C, aiming at practical applications of the materials [9–12].

I stress the impact of discovery of YBCO in terms of the following two meanings.

First, YBCO has demonstrated that transition-metal oxides are intriguing and important materials from both fundamental and practical points of view, the latter being relevant to electronic devices. Since the discovery of YBCO, many interesting physical properties have been found in transition-metal oxides such as colossal magnetoresistance effect in manganese-based perovskite oxides [13] and high-mobility two-dimensional electron gas at the interface between $LaAlO_3$ and $SrTiO_3$ [14].

Secondly, enormous efforts have been made in order to fabricate high-quality YBCO thin films for application, and it has greatly contributed to the development of today's thin film fabrication techniques. Indeed, there are many reports on fabrication of YBCO thin film via several thin film growth methods including sputtering [15, 16], molecular beam epitaxy [17, 18] and

pulsed laser deposition (PLD) methods [19, 20]. Besides these growth methods, structural analysis methods of thin films have been developed as well. For example, the development of high-resolution transmission electron microscope (TEM) has enabled one to evaluate not only crystallinity of thin films but also the sharpness of the interface between thin films and substrates, grain boundaries or density of dislocations in atomic scale [21–23]. Thanks to developments in both growth and analysis methods for thin films, researchers can fabricate high-quality functional transition-metal oxides thin films [24].

G.2 The outline of this thesis

My studies described in this thesis are mainly dedicated to the better information-dependent society through the fabrication of novel transition-metal oxide thin films. Among various kinds of research fields and materials sustaining today's information-dependent society, I have especially focused on the research area called 'spintronics' and propose an Fe–Ti–O transition-metal oxide system called 'ilmenite-hematite ($FeTiO_3$–Fe_2O_3) solid solution' as a promising candidate for a novel functional material. The word of 'spintronics' derives from 'spin' and 'electronics', and spintronics utilizes not only electrical properties of materials but also magnetic properties simultaneously. Indeed, spintronics is one of the hot topics in today's solid state physics and has already contributed to high-density storage such as hard-disc drive system. Recently, many researchers have attempted to apply spintronics materials to the next-generation non-volatile memory called 'magnetoresistive random access memory (MRAM)'. My goal in the thesis is to prepare high-quality thin films of the ilmenite-hematite solid solution and to achieve excellent magnetic and electrical properties, eventually leading to the development of magnetic memory device based on $FeTiO_3$–Fe_2O_3 solid solution system which consists of the abundant elements on the earth. The details of spintronics and $FeTiO_3$–Fe_2O_3 solid solution will be introduced in the initial part of this thesis (see Chapter 1).

I especially pay attention to the fabrication of $FeTiO_3$–Fe_2O_3 solid solution thin films with smooth surface in atomic scale. Devices usually consist of multi-layers of functional materials, and their interface between layers is required to be sharp enough to prevent the degrading of carrier transport properties. Therefore, the surface of underlying substrates and each layer

should be smooth in atomic scale. In this study, I have successfully fabricated $FeTiO_3$–Fe_2O_3 solid solution thin films with atomically smooth surface on sapphire (α–Al_2O_3) substrates by PLD method.

In this thesis, the following contests are described in the individual chapter;

In Chapter 1, the outline of spintronics and $FeTiO_3$–Fe_2O_3 solid solution is briefly mentioned. Because it is almost impossible to explain all kinds of materials, those essential to explain the background of this study will be taken into account. First, I will provide a brief overview of giant magnetoresistive effect, tunneling magnetoresistive effect and the operating principle of MRAM. Secondly, I will review the research background, crystal structure and physical properties of $FeTiO_3$–Fe_2O_3 solid solution, and explain why this material can be considered as promising candidate for spintronics device.

In Chapter 2, the low-temperature growth of $FeTiO_3$–Fe_2O_3 solid solution thin films on C-plane sapphire, α–Al_2O_3 (0001), substrates is shown. This low-temperature growth method is one of the directions toward the achievement of high-quality thin films suitable for device application. In Chapter 2, I will demonstrate that highly crystallized thin films without deep pits can be fabricated though low-temperature growth method by comparing the results with those of thin films grown at higher substrate temperature (such as 700 ºC).

In Chapter 3, I have fabricated high-quality $FeTiO_3$–Fe_2O_3 solid solution thin films on α–Al_2O_3 (0001) substrates by extremely high-growth temperature over 850 ºC. Although there is a large lattice mismatch (about 6%) between C-plane thin film and substrate, thin films with ‘atomically’ flat surface have been grown epitaxially. Those thin films are considered to be grown via one of the step-flow growth modes called “Domain-Matching Epitaxy (DME)”. I will mention the concept of DME growth with the result from high-resolution transmission electron microscopic observation of $FeTiO_3$–Fe_2O_3/α–Al_2O_3 (0001) interface.

In Chapter 4, the growth of $FeTiO_3$–Fe_2O_3 solid solution thin films on A-plane sapphire, α–Al_2O_3 $(11\bar{2}0)$, substrates is reported. Because the A-plane lattice mismatch between thin film and substrate is more than 7%, epitaxial thin films have never demonstrated with usual growth temperature such as 700 ºC. However, I have successfully fabricated $FeTiO_3$–Fe_2O_3 solid solution thin films with atomically flat surface epitaxially on α–Al_2O_3 $(11\bar{2}0)$ substrates at the growth temperature of 850 ºC. I consider that the thin films are also grown by DME mode

just the same as the phenomenon described in Chapter 3. It is particularly worth noting that this epitaxial growth of $FeTiO_3$–Fe_2O_3 solid solution on α–Al_2O_3 $(11\bar{2}0)$ substrates has been realized for the first time.

In Chapter 5, in order to understand the mechanism of electrical conduction in $FeTiO_3$–Fe_2O_3 solid solution, a hard X-ray photoemission spectroscopy has been carried out. Although the end members of solid solution ($FeTiO_3$ and Fe_2O_3) are both insulators, the solid solution is a semiconductor. This difference has not been investigated experimentally yet. Based on the results obtained, I will propose the mechanism for electrical conduction in $FeTiO_3$–Fe_2O_3 solid solution.

Finally, the study performed in this thesis is summarized, and future prospects of $FeTiO_3$–Fe_2O_3 solid solution thin films for spintronics device application is described.

G.3 References

1. J. C. Manifacier and L. Szepessy, *Appl. Phys. Lett.* **31**, 459 (1977).
2. Y. Wu, C. H. M. Marée, R. F. Haglund, J. D. Hamilton, M. A. Morales Paliza, M. B. Huang, L. C. Feldman, and R. A. Weller, *J. Appl. Phys.* **86**, 991 (1999).
3. N. Setter, D. Damjanovic, L. Eng, G. Fox, S. Gevorgian, S. Hong, A. Kingon, H. Kohlstedt, N. Y. Park, G. B. Stephenson, I. Stolitchnov, A. K. Taganstev, D. V. Taylor, T. Yamada, and S. Streiffer, *J. Appl. Phys.* **100**, 051606 (2006).
4. J. F. Scott and C. A. Paz de Araujo, *Science* **246**, 1400 (1989).
5. C. R. Vestal and Z. J. Zhang, *J. Am. Chem. Soc*, **125**, 9828 (2003).
6. J. G. Bednorz and K. A. Müller, *Z. Phys. B* **64**, 189 (1986).
7. J. R. Gavaler, *Appl. Phys. Lett.* **23**, 480 (1973).
8. M. K. Wu, J. R. Ashburn, and C. J. Torng, P. H. Hor, R. L. Meng, L. Gao, Z. J. Huang, Y. Q. Wang, and C. W. Chu, *Phys. Rev. Lett.* **58**, 908 (1987).
9. Z. Z. Sheng and A. M. Hermann, *Nature* **332**, 138 (1988).
10. L. Gao, Y. Y. Xue, F. Chen, Q. Xiong, R. L. Meng, D. Ramirez, and C. W. Chu, *Phys. Rev. B* **50**, 4260 (1994).
11. Y. Kamihara, H. Hiramatsu, M. Hirano, R. Kawamura, H. Yanagi, T. Kamiya, and H. Hosono, *J. Am. Chem. Soc.* **128**, 10012 (2006).
12. http://global-sei.com/super/index.en.html
13. Y. Tokura, and N. Nagaosa, *Science* **288**, 462 (2000).
14. A. Ohtomo, and H. Y. Hwang, *Nature* **427**, 423 (2004).
15. X.Z Liu, B.W Tao, A Luo, S.M He, and Y.R Li, *Thin Solid Films* **396**, 226 (2001).
16. S.K.H Lam, and B Sankrithyan, *Physica C: Supercond.* **377**, 36 (2002).
17. J. Wang, B. Han, F. Chen, T. Zhao, F. Xu, Y. Zhou, G. Chen, H. Lu, Q. Yang, and T. Cui, *Solid State Comm.* **126** 431 (2003).
18. M.R. Cimberle, A. Diaspro, C. Ferdeghini, E. Giannini, G. Grassano, D. Marré, I. Pallecchi, M. Putti, R. Rolandi, and A.S. Siri, *Physica C: Supercond.* **282**, 679 (1997).
19. V. Boffa, T. Petrisor, L. Ciontea, U. Gambardella, and S. Barbanera, *Physica C: Supercond.* **276**, 218 (1997).
20. J.H. Park, and S.Y. Lee, *Sur. Coat. Tech.* **113**, 274 (1999).

21. Z. L. Zhang, U. Kaiser, S. Soltan, H.-U. Habermeier, and B. Keimer, *Appl. Phys. Lett.* **95**, 242505 (2009).
22. F. J. Baca, P. N. Barnes, R. L. S. Emergo, T. J. Haugan, J. N. Reichart, and J. Z. Wu, *Appl. Phys. Lett.* **94**, 102512 (2009).
23. J. Wang, J. H. Kwon, J. Yoon, H. Wang, T. J. Haugan, F. J. Baca, N. A. Pierce, and P. N. Barnes, *Appl. Phys. Lett.* **92**, 082507 (2008).
24. C. Ratcliff, T. J. Grassman, J. A. Carlin, and S. A. Ringel, *Appl. Phys. Lett.* **99**, 141905 (2011).

Chapter 1. Spintronics and ilmenite-hematite solid solution

1.1 Spintronics

1.1.1 Introduction to spintronics

Electrons possess both charge and spin degrees of freedom. As explained in General Introduction, spintronics which derives from the words ‘spin’ and ‘electronics’ is the electronics using both conducting and magnetic properties of materials and has contributed to today’s information technology. Because it is almost impossible to give explanations about all kinds of spintronics-related phenomena and my study has been dedicated to the development of practicable spintronics device based on transition-metal oxides, we limit the explanation to ‘giant magnetoresistive (GMR) effect’ and ‘tunneling magnetoresistive (TMR) effect’ which are key phenomena for today’s or next-generation spintronics device applications. In particular, the latter phenomenon has attracted considerable attention of many researchers aiming for the development of a next-generation non-volatile magnetic memory called ‘magnetoresistive random access memory (MRAM)’. In this chapter, we will also explain about the basic operating principle of MRAM and the relationship between the performance of MRAM and the spin polarization of materials.

1.1.2 Giant magnetoresistive (GMR) effect

Magnetoresistive (MR) effect is the phenomenon where the electric resistivity in materials is varied by applying external magnetic field to them. The magnitude of variation in the electric resistivity is called MR ratio which is described as,

$$\text{MR ratio} = \frac{R_h - R_l}{R_l} \tag{1}$$

where R_l and R_h are the lower and higher electric resistivity resulting from before and after the application of external magnetic field to the material. Although this phenomenon has been found in many metals, alloys and semiconductors, the reported MR ratio is only several % [1–3] and these MR ratios are not enough for the spintronics device application.

In contrast to these MR effects, the giant magnetoresistive (GMR) effect reported by Fert and Grünberg independently in 1988 exhibited more than tens % of MR ratio, that is, one digit higher than previously reported MR effects [4, 5]. Fig. 1.1.1 is the schematic model for the GMR device in which ferromagnetic metal such as Fe (notated as 'F' in Fig. 1.1.1) and nonmagnetic metal such as Cu (notated as 'NM') thin films are stacked alternately. The transport property of electrons depends on the relationship between the direction of magnetic moment due to the spin of conductive electrons and the direction of magnetization in conductive ferromagnetic materials. When these two directions are aligned parallel to each other, the electrons can be transported without being scattered. However, the electrons tend to be scattered during transportation when these two directions are not aligned parallel to each other and the scattering probability is maximum when they are aligned anti-parallel to each other. In Fig. 1.1.1 (a), the magnetizations of all three F layers (described as white arrow) are facing to the right. In this case, the conductive electrons whose direction of magnetic moment (described as black arrow) faces to the right are aligned parallel to the magnetization direction of all three F layers, and can pass through the device without being scattered. On the other hand, in the case the magnetization of one of three F layers faces to the left as illustrated in Fig. 1.1.1 (b), the electrons whose direction of magnetic moment faces to the right are scattered by that F layer. In this manner, the number of electrons which can pass through the whole device without being scattered depends on whether the magnetizations of all F layers are aligned parallel to each other or not, and the electric resistivity of GMR device in Fig. 1.1.1 (a) is lower than that of GMR device in Fig. 1.1.1 (b). The GMR ratio is evaluated as,

$$\text{GMR ratio} = \frac{R_{ap} - R_a}{R_a} \tag{2}$$

where R_p and R_{ap} mean the electric resistivity corresponding to the situations in which the magnetizations in F layers are parallel and anti-parallel to each other, respectively.

The most famous and significant application of GMR effect is hard-disk drive (HDD) system. The schematic illustration of HDD is shown in Fig. 1.1.2 (a). HDD consists of the disk whose surface is covered with ferromagnetic alloy layer and the heads located immediately above the disk. Fig. 1.1.2 (b) is the illustration of the way to write and read the information of HDD. The heads comprise both writing and reading parts discretely. First, the information is written on the recording media as the direction of magnetization in ferromagnetic alloy by magnetic field generated with electric current running through the coil in the writing head. For example, as in Fig. 1.1.2 (b), the magnetization in one division of recording media, where magnetic field generated from the writing head is applied, is facing to the left. The directions of magnetization in each division of recording media (arrows pointing to the right or left in Fig. 1.1.2) correspond to one binary bit (‘0’ or ‘1’). Subsequently, the information recorded on the media is read by reading head (GMR head) as follows. GMR head consists of one nonmagnetic and two ferromagnetic layers where the magnetization in one of the two ferromagnetic layers is fixed (hereafter, fixed layer) but another one is free (free layer). In Fig. 1.1.2. (b), the upper and lower ferromagnetic layers correspond to the fixed and free layers, respectively. When the GMR head approaches the surface of the media, the direction of magnetization in free layer can be changed by the magnetic field generated from each division of the recorded media, and the electric resistivity is also changed depending on whether the magnetization in each division of the media faces to the right or left. In this manner, the GMR head can discriminate each division of the media as it is ‘0’ or ‘1’.

1.1.3 Tunneling magnetoresistive (TMR) effect

Another important MR effect is tunneling magnetoresistive (TMR) effect whose MR ratio is even higher than GMR effect. Similarly to GMR effect, TMR-effect-based device called magnetic tunnel junction (MTJ) consists of two ferromagnetic conductive layers and one nonmagnetic insulator layer and utilizes the variation in tunneling electric current passing through the insulator layers. Generally, tunneling electric current can run easily when these

two magnetizations in ferromagnetic layers are aligned parallel to each other, and the TMR ratio is also evaluated by equation (2) just the same as GMR ratio. Although the first TMR effect was found in Fe/Ge/Co trilayer system by Julliere in 1975, the TMR ratio of that system was only 14% below 4.2 K [6]. The remarkable improvement in TMR effect was achieved by Miyazaki and Moodera independently in 1995 [7, 8]. They both found the TMR ratio in Fe/amorphous Al_2O_3/Fe MTJ device to be about 20% in ambient temperature. In 2001, Butler *et al.* predicted that TMR ratio in Fe (001)/single crystal MgO (001)/Fe (001) MTJ device would be over 1,000% using first-principles calculations [9], and Yuasa *et al.* have successfully fabricated the Fe/MgO/Fe MTJ device, which exhibits the TMR ratio of 88% in ambient temperature, via molecular beam epitaxy [10] in 2004 and raised the TMR ratio to 180% in ambient temperature by optimizing the growth condition to obtain higher crystalline quality of MgO insulate layer [11] in the same year, i.e., in 2004. After their report, the motivation for the exploration of larger TMR ratio has soared in order to develop next-generation spintronics device including TMR head for HDD and MRAM (see next section 1.1.4). Up to now, the reported TMR ratio has become to be over 500% in ambient temperature in MTJ devices based on full-Heusler alloys [12, 13] (see Section 1.1.6).

1.1.4 Magnetoresistive Random Access Memory (MRAM)

As noted repeatedly, magnetoresistive random access memory (MRAM) is one of the promising next-generation spintronics devices. Fig. 1.1.3 is the schematic illustrations for the structure and operating principle of MRAM. In MRAM, lots of MTJ devices corresponding to binery bits are arranged as Fig. 1.1.3 (a). One of the magnetizations in ferromagnetic layers of each MTJ device is fixed and another one is free. Each MTJ device is attached to one bit line and two word lines. The operating principle of MRAM is very similar to that of HDD. In writing information on MRAM, the electric current runs along writing word line as well as bit line and generates magnetic field which can change the magnetization in free layer of each MTJ device. The binary bit information is recorded in each MTJ device in this way. On the other hand, in the case of reading information, the electric current runs through the MTJ device and the magnitude of electric resistivity, which depends on the alignment of two magnetizations in

ferromagnetic layers, is measured.

There are some merits in MRAM compared to the current dynamic random access memory (DRAM). First, MRAM is a non-volatile memory. Because the information is recorded by injecting electric charge into the condensers, the information stored in DRAM disappears completely by losing electric charge from the condensers when one turns off the computer. The computer must rewrite information on DRAM again when it is rebooted, which is waste of time and electricity. On the other hand, MRAM stores information as magnetizations of ferromagnetic materials which do not disappear even after the computers are turned off. Therefore, the computer can be rebooted more quickly and one can suppress the consummation of electricity.

1.1.5 Spin polarization and two-current model

As described in section 1.1.3. and 1.1.4., both GMR and TMR effects utilize the spin-dependent electron transport, and electrons can be transported easily when magnetizations of ferromagnetic layers in GMR or TMR device point to the same direction. The coherence between the directions of magnetization is important not only in macroscopic sense as explained above but also in microscopic sense. The latter is discussed in relation to a proportion of 'spin polarization'. Spin polarization P is defined as,

$$P = \frac{D_{\uparrow}(E_F) - D_{\downarrow}(E_F)}{D_{\uparrow}(E_F) + D_{\downarrow}(E_F)} \tag{3}$$

where $D_{\uparrow}(E_F)$ and $D_{\downarrow}(E_F)$ are the density of states (DOS) of the up (↑) and down (↓) spin electrons at Fermi level (E_F). Materials can be classified into three groups (paramagnets, ferromagnets, and half-metals) in terms of spin polarization as illustrated in Fig. 1.1.4. In paramagnets, the band structure of up and down spin electrons can be described symmetrically as in Fig. 1.1.4 (a) and the DOS of the up and down spins at E_F is the same as each other, resulting in $P = 0$ as found from the equation (3). On the other hand, in ferromagnets such as Fe, Co, or Ni, the bands of up and down spin electrons are splitting due to exchange interactions

and P becomes non-zero ($0 < P < 1$). In contrast to these two materials, half-metals possess unique band structure. Fig. 1.1.4 (c) is the schematic band structure of half-metals where the DOS of up spin electrons is metallic but that of down spin electrons is similar to semiconductors at E_F. Spin-dependent electron transport is generally explained by two-current model [6] where electric current is considered to consist of up and down spin electrons and electric charge is transported by them separately as illustrated in Fig. 1.1.5. Therefore, only up spin electrons can contribute to the electric conductivity in half-metals and $P = 1$ due to $D_{\downarrow}(E_F) = 0$. Spin polarization directly affects the TMR ratio as following equation proposed by Jullier [6],

$$\text{TMR ratio} = \frac{R_{ap} - R_a}{R_a} = \frac{2P_1P_2}{1 - P_1P_2} \tag{4}$$

where P_1 and P_2 are spin polarization of two materials which constitute top and bottom ferromagnetic layers in MTJ device. From equation (4), one can see that ideal TMR ratio is infinite if $P_1 = P_2 = 1$ according to the theory. Therefore, it is desirable that materials such as half-metals are applied to MTJ device in order to realize high-performance devices including MRAM.

1.1.6 The candidates for promising half-metals

As mentioned above, half-metals are considered to be promising candidates for high-performance MRAM due to their high spin polarization (theoretically, 100%). Up to now, there have been lots of studies on half-metals from both theoretical and experimental approaches. The first report on half-metal was given by de Groot *et al.* In 1983, they calculated the band structure of Mn-based Heusler alloys with the $C1_b$ crystal structure (half-Heusler alloys) such as NiMnSb and PtMnSb by the augmented-spherical-wave method and predicted that these Heusler alloys would be half-metals [14]. Since then, many materials have been predicted to be half-metals. For example, Ishida *et al.* predicted that $Co_2Cr_{1-x}Fe_xAl$ alloy system which is Co-based Heusler alloys with the $L2_1$ crystal structure (full-Heusler alloys) would be half-metals in 1995 [15], and not only Heusler alloys but also some other

materials including zinc blende structure compounds (CrAs [16]) and transition-metal oxides (CrO_2 [17], Fe_3O_4 [18] and perovskite La–Sr–Mn–O system (LSMO) [19]) are considered to be half-metals.

Along with the theoretical calculations, some of them (especially full-Heusler alloys) have been experimentally confirmed to be half-metals, and MTJ device based on them have been also demonstrated. For example, Wang *et al.* have fabricated Co_2FeAl/MgO/CoFe MTJ device based on full-Heusler alloy Co_2FeAl by simple sputter-deposition techniques, and demonstrated the TMR ratio up to 330% at room temperature (700% at 10 K) in their MTJ device [20]. As noted in the section 1.1.3, up to now, the TMR ratio of over 500% in ambient temperature has been realized in MTJ devices based on full-Heusler alloys of CoFeB system [12, 13]. In this way, Heusler alloys are promising half-metals for spintronics device application.

On the other hand, Soulen *et al.* measured spin polarization at Fermi level of some materials using superconducting point contact method and found that perovskite LSMO and CrO_2 showed spin polarization of 78 $\pm$ 4.0 and 90 $\pm$ 3.6% at liquid helium temperature, respectively [21]. In 2003, Bowen *et al.* demonstrated huge TMR ratio of more than 1800% at 4 K in LSMO/$SrTiO_3$/LSMO MTJ device [22]. Although their huge TMR ratio can be obtained only at liquid helium temperature and drastically decreases to 12% at 270 K, their demonstration sheds light on the possibility of transition-metal oxides to be promising candidates for half-metals in order to realize high-performance MRAM.

Among these transition-metal oxides, ilmenite-hematite solid solution is also theoretically predicted to be a half-metal [23], and this is why I have paid attention to this material in this study. In addition to this fact, ilmenite-hematite solid solution possesses high ferrimagnetic Curie temperature [24] and finds unique property in its carrier which can be varied so that the material becomes both *n*- and *p*- types with controlling the composition of solid solution [25]. The details of these properties of ilmenite-hematite solid solution are discussed in the next section.

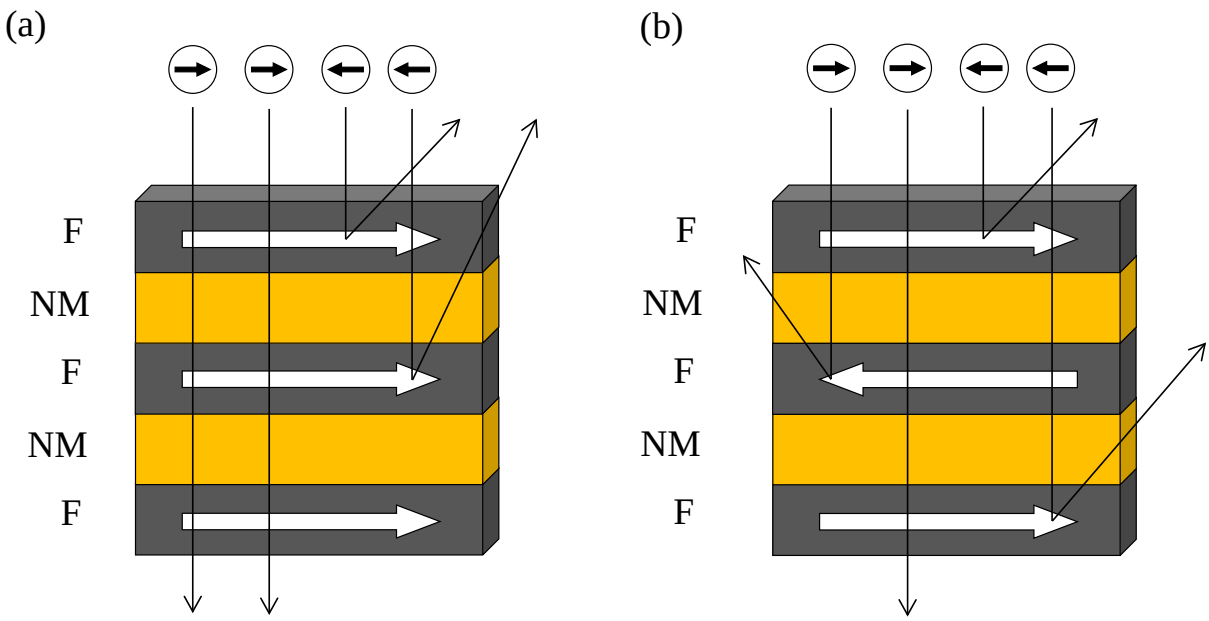

Fig. 1.1.1 The schematic images of giant magnetoresistive effect in the case of the magnetizations in all three ferromagnetic layers are aligned parallel to each other (a), and one of them is aligned to anti-parallel to remained two layers (b). The ‘F’ and ‘NM’ descriptions mean ‘ferromagnetic’ and ‘nonmagnetic’ layers, respectively. The directions of magnetic moment due to spin in conducting electrons and magnetization in ferromagnetic layers are indicated by black and white arrows, respectively.

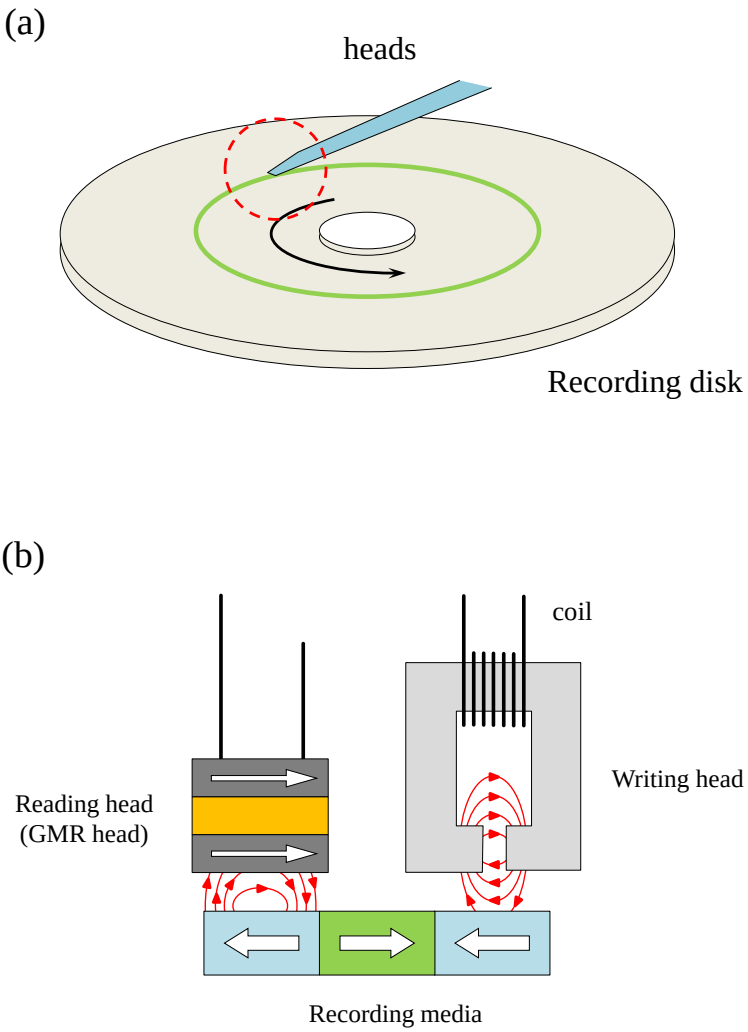

Fig. 1.1.2 (a) The schematic illustration of recording media and heads of hard disk drive (HDD) system. The light-green circle in the recording disk corresponds to the part where the heads are writing or reading information of the media. (b) The schematic illustration of wring and reading (GMR) heads. This illustration corresponds to the region encircled by red dash-line in Fig. 1.1 (a). The write arrows indicate the direction of magnetization in the divisions of recording media and the ferromagnetic layer in GMR head. The magnetic field from writing head and one of the divisions of recording media is indicated by red arrow.

(a)

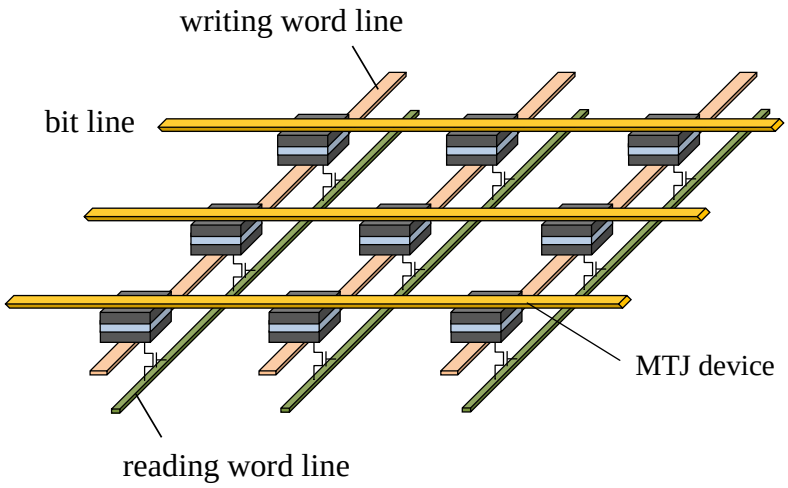

(b)

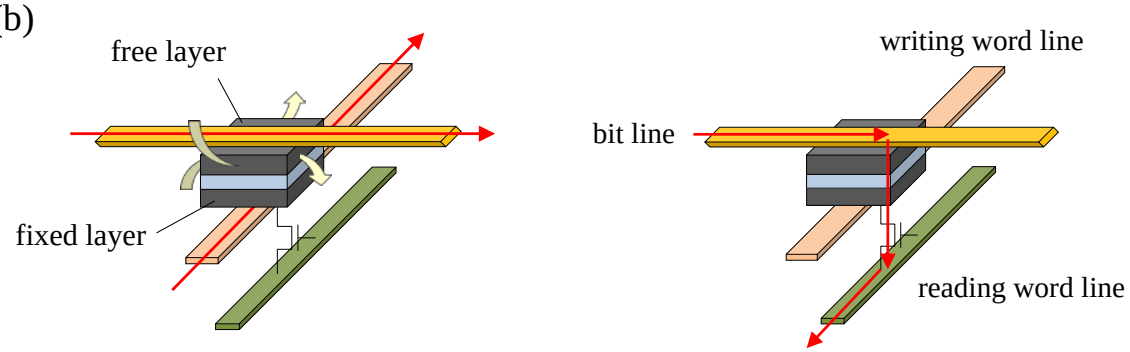

Fig. 1.1.3 (a) The schematic illustration of the structure in MRAM. (b) The schematic illustration of wring and reading operating principle in MRAM. The left side shows how to write information on MRAM. The white arrows indicate the magnetic field generated by electric current running along bit line and writing word line (denoted by red arrows). The right side shows how to read information from MRAM. The red arrows also indicate electric current running lines and MTJ device just the same as the left side image.

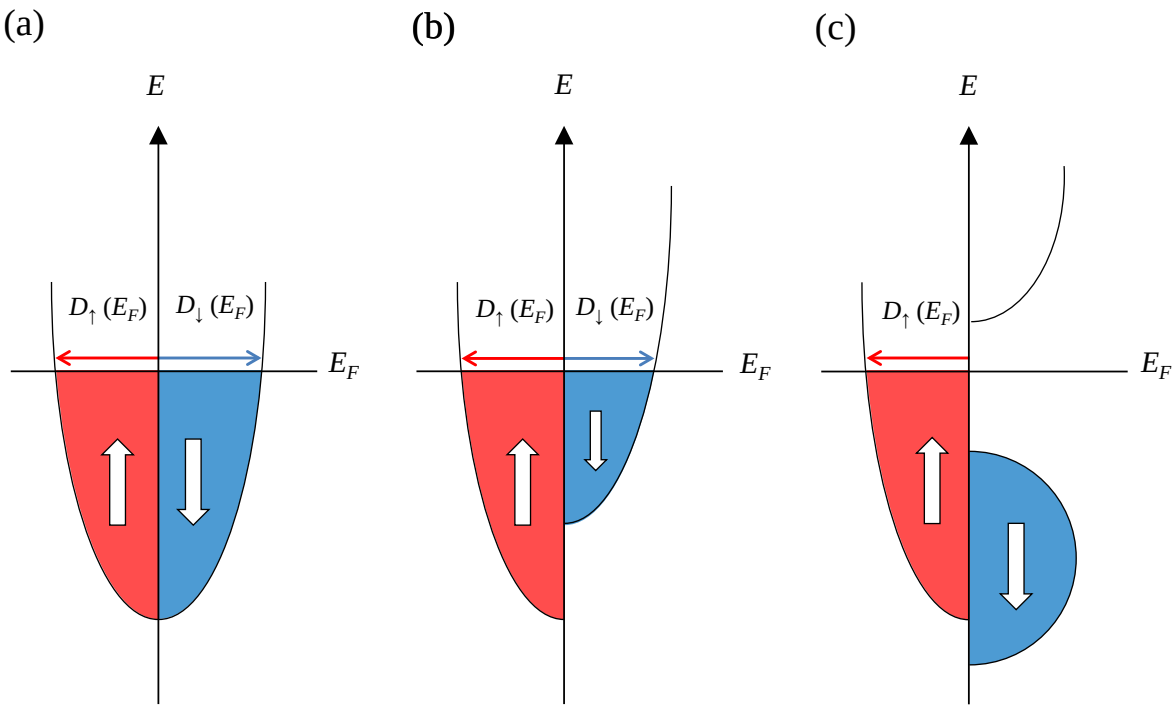

Fig. 1.1.4 The schematic illustrations of the band structure in paramagnets (a), ferromagnets (b), and half-metals (c). In each illustration, the band structures of up and down spin electrons are denoted by red and blue regions, and E_F indicates the Fermi level. $D_\uparrow(E_F)$ and $D_\downarrow(E_F)$ indicate the density of states of the up and down spin electrons at E_F, respectively.

(a)

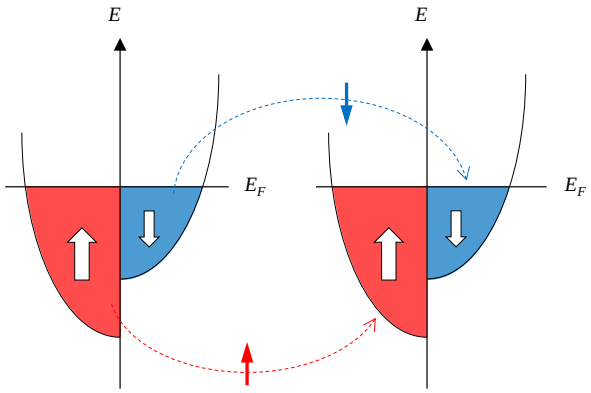

(b)

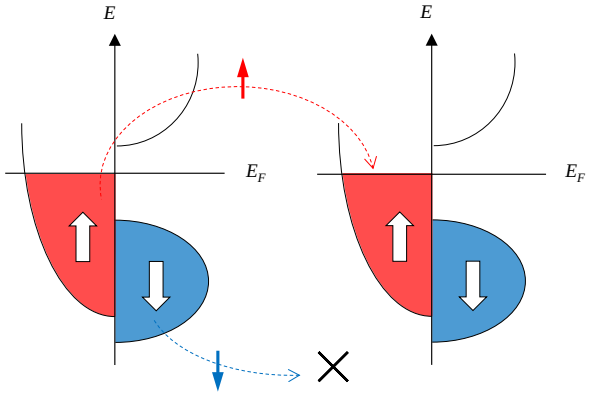

Fig. 1.1.5 The schematic illustrations of two-current model in the same materials of ferromagnets (a), and half-metals (b). As in the Fig. 1.1.4, the band structures of up and down spin electrons are denoted by red and blue regions, and E_F indicates the Fermi level. The red and blue arrows indicate the transfer of up and down spin electrons in the same materials. In Fig. 1.1.5 (a), both up and down spin electrons can transfer but the former can transfer easily than the latter because of the difference in the density of states at E_F between them. In Fig. 1.1.5 (b), only up spin electrons can transfer reflecting the characteristic of half-metal in this case where the density of states at E_F of the down spin electrons is zero.

1.1.7 References

1. H. W. Lehmann, and M. Robbins, *J. Appl. Phys.* **37**, 1389 (1966).
2. H. W. Lehmann, *Phys. Rev.***163**, 488 (1967).
3. A. Amith, and G. L.Gunsalus, *J.Appl.Phys.***40**, 1020 (1969).
4. M. Baibich, J. M. Broto, A. Fert, F. Nguyen Van Dau, F. Petroff, P. Eitenne, G. Creuzet, A. Friederich, and J. Chazelas, *Phys. Rev. Lett*. **61**, 2472 (1988).
5. G. Binasch, P. Grünberg, F. Saurenbach, and W. Zinn, P*hys. Rev. B* **39**, 4828 (1989).
6. M. Julliere, *Phys. Lett*. **54A**, 225 (1975).
7. T. Miyazaki, and N. Tezuka, *J. Magn. Magn. Mater.* **139**, L231 (1995).
8. J. S. Moodera, Lisa R. Kinder, Terrilyn M. Wong, and R. Meservey, *Phys. Rev. Lett.* **74**, 3273 (1995).
9. W. H. Butler, X. –G. Zhang, T. C. Schulthess, and J. M. Maclaren, *Phys. Rev. B* **63**, 054416 (2001).
10. S. Yuasa, A. Fukushima, T. Nagahama, K. Ando, and Y. Suzuki, *Jpn. J. Appl. Phys.* **43**, L588 (2004).
11. S. Yuasa, T. Nagahama, A. Fukushima, Y. Suzuki, and K. Ando, *Natue Mater.* **3**, 868 (2004).
12. Y. M. Lee, J. Hayakawa, S. Ikeda, F. Matsukura, and H. Ohno, *Appl. Phys. Lett.* **90**, 212507 (2007).
13. S. Ikeda, J. Hayakawa, Y. Ashizawa, Y. M. Lee, K. Miura, H. Hasegawa, M. Tsunoda, F. Matsukura, and H. Ohno, , *Appl. Phys. Lett.* **93**, 082508 (2008).
14. R. A. de Groot, F. M. Mueller, P. G. van Engen, and K. H. J. Buschow, *Phys. Rev. Lett.* **50**, 2024 (1983).
15. S. Ishida, S. Fujii, S. Kashiwagi, and S. Asano, *J. Phys. Soc. Jpn.* **64**, 2152 (1995).
16. H. Akinaga, T. Manago, and M. Shirai, *Jpn. J. Appl. Phys.* **39**, L1118 (2000).
17. K. Schwarz, *J. Phys. F: Met. Phys* **16**, L211 (1986).
18. A. Yamase, and K. Shiratori, *J. Phys. Soc. Jpn.* **53**, 312 (1984).
19. Y. Okimoto, T. Katsufuji, T. Ishikawa, A. Urushibara, T. Arima, and Y. Tokura, *Phys. Rev. Lett.* **75**, 109 (1995).

20. Wenhong Wang, Hiroaki Sukegawa, Rong Shan, Seiji Mitani, and Koichiro Inomata, *Appl. Phys. Lett.* **95**, 182502 (2009).
21. R. J. Soulen, Jr., J. M. Byers, M. S. Osofsky, B. Nadgorny, T. Ambrose, S. F. Cheng, P. R. Broussard, C. T. Tanaka, J. Nowak, J. S. Moodera, A. Barry, and J. M. D. Coey, *Science* **282**, 85 (1998).
22. M. Bowen, M. Bibes, A. Barthélémy, J.-P. Contour, A. Anane, Y. Lemaître, and A. Fert, *Appl. Phys. Lett.* **82**, 233 (2003).
23. W. H. Butler, A. Bandyopadhyay, and R. Srinivasan, *J. App. Phys.* **93**, 7882 (2003).
24. Y. Ishikawa, *J. Phys. Soc. Jpn.* **12** 1083 (1957).
25. Y. Ishikawa, *J. Phys. Soc. Jpn.* **13**, 37 (1958).

1.2 Ilmenite-hematite solid solution

1.2.1 Crystal structure and research background of ilmenite-hematite solid solution

Before we introduce detailed physical properties of ilmenite-hematite solid solution and the reason why we consider this material to be promising candidate for spintronics application, the crystal structure and research background of it including its end members, ilmenite and hematite, are overviewed.

First, the crystal structure of ilmenite ($FeTiO_3$) and hematite (α–Fe_2O_3) are shown in Fig. 1.2.1 which is depicted with VESTA software [1] and the crystallographic information listed in reference [2] and [3]. Both of them have a corundum-based structure where oxide anions are arranged into a distorted hexagonal close packed sublattice, and the two-third of their octahedral interstices are occupied by cations. From Fig. 1.2.1, one can see that α–Fe_2O_3 has alternately stacked Fe and O layers along its *c*-axis. On the other hand, $FeTiO_3$ has two kinds of cation layers (Fe and Ti layers) and these two cation layers between O layers also appear alternately along *c*-axis of $FeTiO_3$. This difference of cation layer between $FeTiO_3$ and α–Fe_2O_3 results in the difference of the crystallographic space group of them; $FeTiO_3$ belongs to the space group of $R\bar{3}$ whereas α–Fe_2O_3 belongs to that of $R\bar{3}c$. They constitute complete solid solution [4] due to the similarity in crystallographic characteristics including lattice constant; $FeTiO_3$ (a = 5.087 Å, c = 14.082 Å), α–Fe_2O_3 (a = 5.038 Å, c = 13.772 Å). Hereafter, the author denotes ilmenite-hematite ($FeTiO_3$–Fe_2O_3) solid solution as $x FeTiO_3 \cdot (1–x) Fe_2O_3$ ($0 < x < 1$), where x means the molar fraction of $FeTiO_3$.

Although both end members are antiferromagnetic insulators, specific crystal phase of $FeTiO_3$–Fe_2O_3 solid solution called ‘ordered phase’ becomes a ferrimagnetic semiconductor whereas the phase called ‘disordered phase’ still remains an antiferromagnet [5, 6]. Fig. 1.2.2 shows schematic illustrations of $FeTiO_3$–Fe_2O_3 solid solution of both ordered and disordered phases. First, in disordered phase, Fe and Ti cations are distributed randomly in each cation layer. In $FeTiO_3$–Fe_2O_3 solid solution, ferromagnetic interaction occurs within each layer whereas antiferromagnetic interaction occurs between adjacent two cation layers. As a result, the magnetic moments in Fe cations which are indicated by black arrow are aligned as Fig. 1.2.2 (a), where the number of magnetic moments in Fe cations pointing to the right and left is almost the same and the magnitude of net magnetization in the whole disordered phase becomes almost

zero. On the other hand, ordered phase has alternating Fe-only and Ti-rich cation layers (noted as layer A and B respectively in Fig. 1.2.2) stacking alternately along *c*-axis just the same as $FeTiO_3$. In this case, antiferromagnetic coupling of magnetic moments between adjacent two cation layers results in ferrimagnetism due to the difference in the number of Fe cations between layers A and B. Ordered phase is a semiconductor where electrons are considered to transfer between Fe^{2+} and Fe^{3+} cations in layer A (the detailed mechanism of this electron transfer will be discussed in Chapter 5). This order-disorder transition in $FeTiO_3$–Fe_2O_3 solid solution depends on its composition and temperature as indicated in a phase diagram of Fig. 1.2.3 [7], indicating that ordered-phase of $FeTiO_3$–Fe_2O_3 solid solution can be obtained within the limited ranges of composition and temperature. As will be mentioned in Section 1.2.3., this limitation also affects the growth condition for thin films of ordered-phase of $FeTiO_3$–Fe_2O_3 solid solution.

$FeTiO_3$–Fe_2O_3 solid solution is a mineral and has been researched in paleomagnetics where researchers investigate the history of geomagnetism by examining remanent magnetization preserved in minerals of various ages. $FeTiO_3$–Fe_2O_3 solid solutions are especially important minerals for these studies because they bear magnetic Fe cations and abundantly exist on the earth. $FeTiO_3$–Fe_2O_3 solid solution can be transformed into other crystalline phase such as the solid solution of magnetite (Fe_3O_4) and ulvospinel (Fe_2TiO_4) (titanomagnetite) depending on the temperature and oxygen fugacity around them during its crystallization and cooling process. Fig. 1.2.4 is TiO_2–FeO–Fe_2O_3 ternary diagram where vertical and horizontal arrowed lines indicate compositional Fe/Ti ratio and the valence of Fe cations [8], and one can see that the crystalline phase is varied with the valence of Fe cations which depends on the temperature and oxygen fugacity. Therefore, $FeTiO_3$–Fe_2O_3 solid solution is also important mineral in petrology because researchers can evaluate the ancient environment of the place in which those minerals are obtained by analyzing the crystalline phase. In 1964, Buddington and Lindsley have established the concept of ‘geothermometer’; one can estimate the formation temperature and oxygen fugacity of minerals from their composition and valence of cations [9].

1.2.2 Physical properties of ilmenite-hematite solid solution

1.2.2.1 Magnetic properties of ilmenite-hematite solid solution

One of the comprehensive studies on the magnetic properties of $FeTiO_3$–Fe_2O_3 solid solution has been conducted by Ishikawa *et al.* [5] They prepared $x$$FeTiO_3$·(1–$x$)$Fe_2O_3$ bulk specimens with the whole composition range of $0 \leq x \leq 1$ and investigated their magnetic properties systematically.

First, they found that the strong ferrimagnetism could be observed in the solid solution with the composition range of $0.5 < x \leq 0.95$ which were prepared by quenching the mixture of $FeTiO_3$ and α–Fe_2O_3 from 1200 ºC after it was sintered and maintained at that temperature for 6 to 12 h. As seen from Fig. 1.2.3, $FeTiO_3$–Fe_2O_3 solid solution with ordered phase can be obtained in the limited temperature range, and it has a miscibility gap (indicated by '$R\bar{3}c$ + $R\bar{3}$') in the composition and temperature ranges of $0.25 < x < 0.85$ and 800 K < T < 950 K where it exsolves into its end members; this means quenching specimens from high temperature to ambient temperature is a key factor to obtain ordered phase with strong ferrimagnetism.

Fig. 1.2.5 is the temperature-dependence of the magnetization of $x$$FeTiO_3$·(1–$x$)$Fe_2O_3$ bulk specimens. The magnetization increases almost linearly with a decrease in temperature from their Curie temperature (T_C) to lower temperature where T_C is evaluated by extrapolating the linear part of the curve to the abscissa axis (the dashed lines). The inset of Fig. 1.2.5 is a composition-dependence of T_C in the solid solution. The T_C varies almost linearly between 55 and 950 K which are Néel temperature of $FeTiO_3$ and α–Fe_2O_3 respectively, following the equation,

$$T_C = 55x + 950 \times (1 - x) \quad (1)$$

T_C is 99.7 K which is higher than liquid nitrogen temperature (77 K) when x = 0.95, and is over room temperature when $x < 0.73$. Therefore, it can safely be said that $FeTiO_3$–Fe_2O_3 solid solution is practical ferrimagnet with high T_C.

1.2.2.2 Electric properties of ilmenite-hematite solid solution

Ishikawa *et al.* have also systematically investigated the electric properties of bulk $x$$FeTiO_3$·(1–$x$)$Fe_2O_3$ specimens with the composition range of $0.33 \leq x \leq 1$ [6], which were

prepared by the same method as their report on magnetic properties of $FeTiO_3$–Fe_2O_3 solid solution [5].

Fig. 1.2.6 (a) is the temperature-dependence of electric resistivity ρ of $FeTiO_3$–Fe_2O_3 solid solution with various compositions. Although the curves have some bending points because of the porosity in their bulk specimens which affects the electric property measurement, they show similar gradient except for $FeTiO_3$ end member. This means that the activation energy E of all specimens is estimated to be almost the same as each other (0.25 – 0.40 eV) from the following equation.

$$\rho = \rho_0 \exp (E/2kT) \tag{2}$$

The electric resistivity of $FeTiO_3$ significantly decreases when it forms solid solution with α–Fe_2O_3 and also decreases with an increase in the ratio of α–Fe_2O_3. Fig. 1.2.6 (b) is the composition-dependence of the electric resistivity and one can see that the electric resistivity becomes minimum when $x = 0.5$.

Fig. 1.2.7 is the composition-dependence of Seebeck coefficient of $FeTiO_3$–Fe_2O_3 solid solution series where Seebeck coefficient changes systematically with the composition of $FeTiO_3$–Fe_2O_3 solid solution. Its sign is negative (corresponding to *n*-type carrier) when $x < 0.73$ whereas it is positive (*p*-type carrier) when $x > 0.73$. This means that the carrier type can be tuned as either *p*- or *n*-type by simply changing the composition. This controllability of carrier type has a possibility to realize homo *p*-*n* junction device based on $FeTiO_3$–Fe_2O_3 solid solution thin films with different compositions.

The authors also discussed the valence states of cations and the electric conduction mechanism in $FeTiO_3$–Fe_2O_3 solid solution. I will introduce their proposal and further discuss the mechanism of electric conduction in $FeTiO_3$–Fe_2O_3 solid solution in Chapter 5 where I present data of hard X-ray photoemission spectroscopy in order to analyze electronic structure of the solid solution and compare the spectrum to theoretical reports by another groups including Ishikawa *et al*.

1.2.2.3 Spin polarization of ilmenite-hematite solid solution

As mentioned before, materials with high spin polarization are required in order to realize high-performance MRAM, and half-metals are considered to be promising candidates for such materials. Butler *et al.* calculated the density of states (DOS) of α–Fe_2O_3 and $x$$FeTiO_3$·(1–$x$)$Fe_2O_3$ ($x \leq 0.5$) using full potential density functional theory implemented in the generalized gradient approximation, and suggested that the latter is a half-metal up to 1000 K [10]. Fig. 1.2.8 is the DOS of 0.5$FeTiO_3$·0.5Fe_2O_3 and one can see that the DOS near Fermi level shows half-metallic characteristics. In this calculation model of 0.5$FeTiO_3$·0.5Fe_2O_3, the authors substituted 25% of Fe cations in α–Fe_2O_3 by Ti cations. This substitution results in the ordered-phase with alternating Fe-only layer and Fe-Ti layer which include 50% of Fe cations, and ferrimagnetism in the ordered-phase due to the same mechanism as described in the Section 1.2.1 and Fig. 1.2.2. The substitution also affects the electronic structure of α–Fe_2O_3. The calculated DOS diagram of α–Fe_2O_3 shows the band gap of 0.43 eV at Fermi level in both up- and down-spin channel (not shown). Although one of two spin channels still remains insulating, the other spin channel becomes conducting after the substitution. Similar effect could be observed in solid solutions with lower Ti substitution.

Although the authors' results indicate that $x$$FeTiO_3$·(1–$x$)$Fe_2O_3$ with only the composition range of $x \leq 0.5$ can be half-metals, high spin polarization is also expected in the solid solution with $x > 0.5$ and it is worth investigating experimentally their spin polarization in order to realize magnetic tunneling junction device based on $FeTiO_3$–Fe_2O_3 solid solution.

1.2.3 Previous studies on ilmenite-hematite solid solution thin films

As discussed in the Section 1.2.2., $FeTiO_3$–Fe_2O_3 solid solution possesses unique physical properties including controllability of its carrier-type, practicable ferrimagnetism with high T_C, and its high spin polarization, and is considered to be one of the promising materials for spintronics application. Up to now, many research groups have fabricated $FeTiO_3$–Fe_2O_3 solid solution thin films on corundum sapphire (α–Al_2O_3) substrates via several vacuum deposition methods and investigated their physical properties. For example, Zhou *et al.* have reported the

first study on epitaxial growth of xFeTiO$_3$·(1–x)Fe$_2$O$_3$ (x = 0.55, 0.65, 0.73, 0.80, and 0.90) thin films [11]. They fabricated those thin films on α–Al$_2$O$_3$ (0001) substrates with pulsed laser deposition (PLD) method using KrF excimer laser and post-annealing in PLD chamber. In their report, epitaxial thin films with good crystallinity can be obtained via post-annealing whereas as-deposited thin films are amorphous. Fujii *et al.* have reported similar studies in 2004. They have also fabricated xFeTiO$_3$·(1–x)Fe$_2$O$_3$ (x = 0.77) epitaxial thin films on α–Al$_2$O$_3$ (0001) substrates by helicon plasma-sputtering technique and post-annealing [12, 13]. After their reports, Hojo *et al.* have reported a direct fabrication of xFeTiO$_3$·(1–x)Fe$_2$O$_3$ (x = 0.60, 0.73, and 0.80) thin films using PLD method without post-annealing by optimizing the growth rate of thin films [14–17]. Those reports from several research groups have shown that the physical properties of their thin films are similar to those of bulk specimens reported by Ishikawa [5, 6] and that FeTiO$_3$–Fe$_2$O$_3$ solid solution thin films are expected to be promising materials for spintronics application. However, the surface structure of their thin films is not smooth enough to be applied for multi-layered device such as magnetic tunneling junction device or has not been investigated at all.

As I explained in General Introduction, atomically smooth surface is required to realize high-performance devices because the rough interface between thin films seriously degrades the transport properties of materials. The main reason why it is difficult to fabricate epitaxial FeTiO$_3$–Fe$_2$O$_3$ solid solution thin films with atomically smooth surface is the large lattice mismatch (about 7%) between thin films and α–Al$_2$O$_3$ substrates (the lattice constants of α–Al$_2$O$_3$ are as follows; a = 4.763 Å, c = 13.003 Å). However, α–Al$_2$O$_3$ is suitable substrate for the fabrication of FeTiO$_3$–Fe$_2$O$_3$ solid solution thin films because its crystal structure (space group: $R\bar{3}c$) is the same as α–Fe$_2$O$_3$ (space group: $R\bar{3}c$), and it is a thermally and chemically stable material which prevents the interdiffusion of atoms at interface between thin film and substrate during thin film growth. Therefore, it is desirable to fabricate FeTiO$_3$–Fe$_2$O$_3$ solid solution thin films with atomically smooth surface on α–Al$_2$O$_3$ substrates by optimization of growth conditions rather than exploring alternate substrate which possesses smaller lattice mismatch against FeTiO$_3$–Fe$_2$O$_3$ solid solution thin films.

In order to address this problem, I have studied the fabrication of epitaxial FeTiO$_3$–Fe$_2$O$_3$ solid solution thin films with atomically smooth surface using PLD method via optimizing their

growth conditions. I introduce the results in the following chapters. The optimization of growth conditions is testing challenge in the case of $FeTiO_3$–Fe_2O_3 solid solution thin films, because ordered-phase of $FeTiO_3$–Fe_2O_3 solid solution can be obtained within very limited formation conditions of oxygen fugacity and temperature as indicated in Fig. 1.2.3 and 1.2.4. This difficulty in the optimization of growth conditions was also reported in previous reports on fabrication of $FeTiO_3$–Fe_2O_3 solid solution thin films [11–17]. The present studies in this thesis also have faced this difficulty but I have successfully fabricated $FeTiO_3$–Fe_2O_3 solid solution thin films with atomically smooth surface.

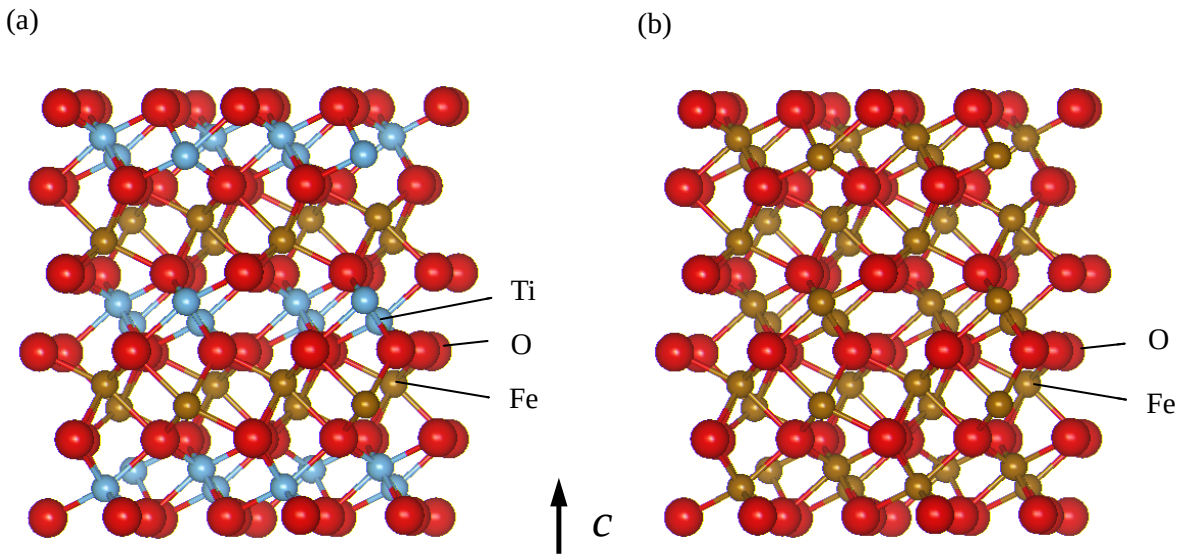

Fig. 1.2.1 The crystal structure of (a) $FeTiO_3$ (space group : $R\bar{3}$), and (b) α-Fe_2O_3 (space group : $R\bar{3}c$). The upper direction of the plane of paper is the crystallographic *c*-axis direction of them. Red, blue and brown balls indicate O, Ti and Fe ions respectively. Both crystal structures were depicted by VESTA software [1] using the crystallographic information listed in reference [2] and [3].

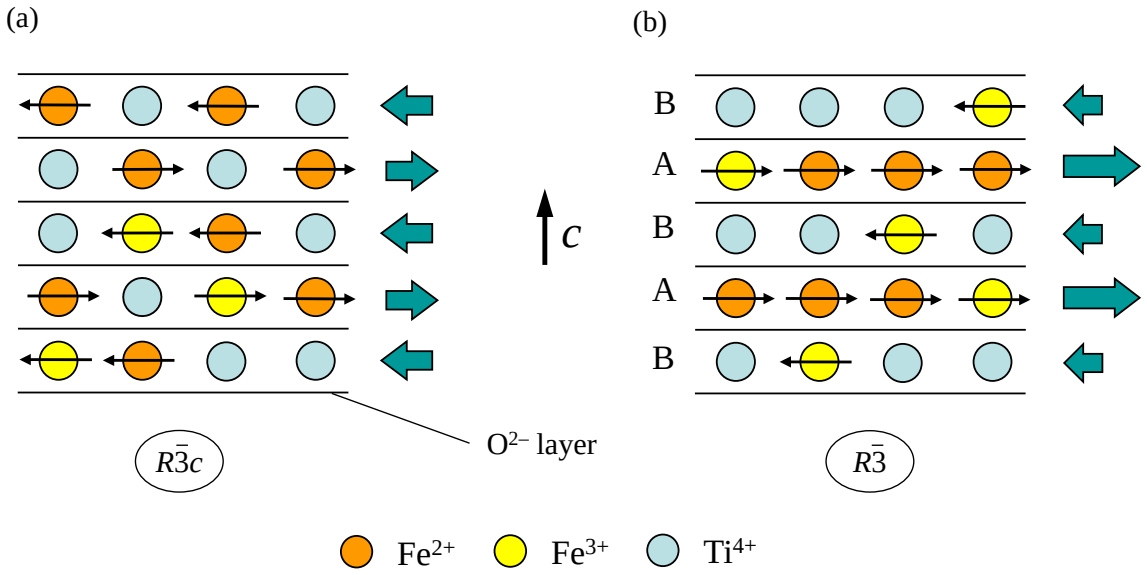

Fig. 1.2.2 The schematic illustrations of (a) disordered phase (space group: $R\bar{3}c$) and (b) ordered phase (space group: $R\bar{3}$) of $FeTiO_3$–Fe_2O_3 solid solution. The black arrow in each Fe cations is the direction of magnetic moment of them. The capitals 'A' and 'B' in Fig. 1.2.2 (b) indicate Fe-only and Ti-rich cation layers respectively. The green arrows in each cation layers indicate the magnitude and direction of magnetic moments in them.

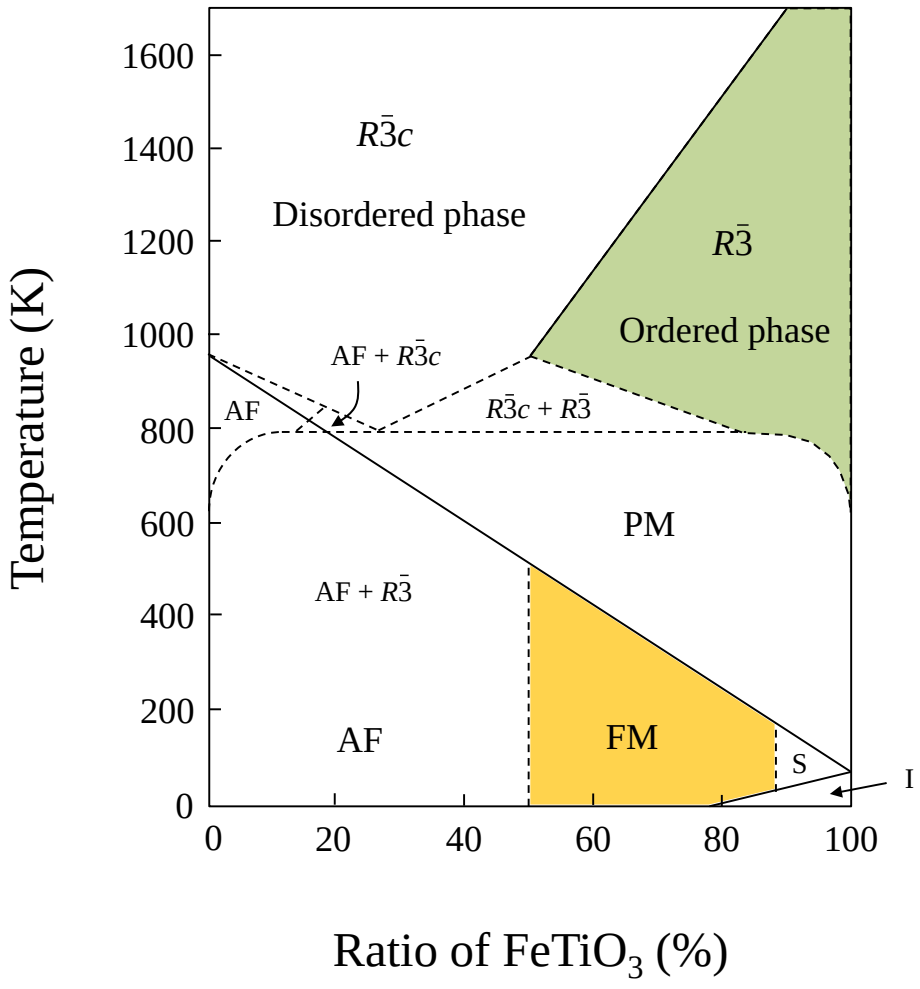

Fig. 1.2.3 The phase diagram of $FeTiO_3$–Fe_2O_3 solid solution system. The long solid line indicates the variation in Néel temperature with the composition. The notations of magnetic states indicate as follows; PM = paramagnet, AF = antiferromagnet where spins are aligned perpendicular to *c*-axis of the solid solution, FM = ferrimagnet, S = spin glass, and I = antiferromagnet where spins are aligned parallel to *c*-axis of the solid solution, respectively.

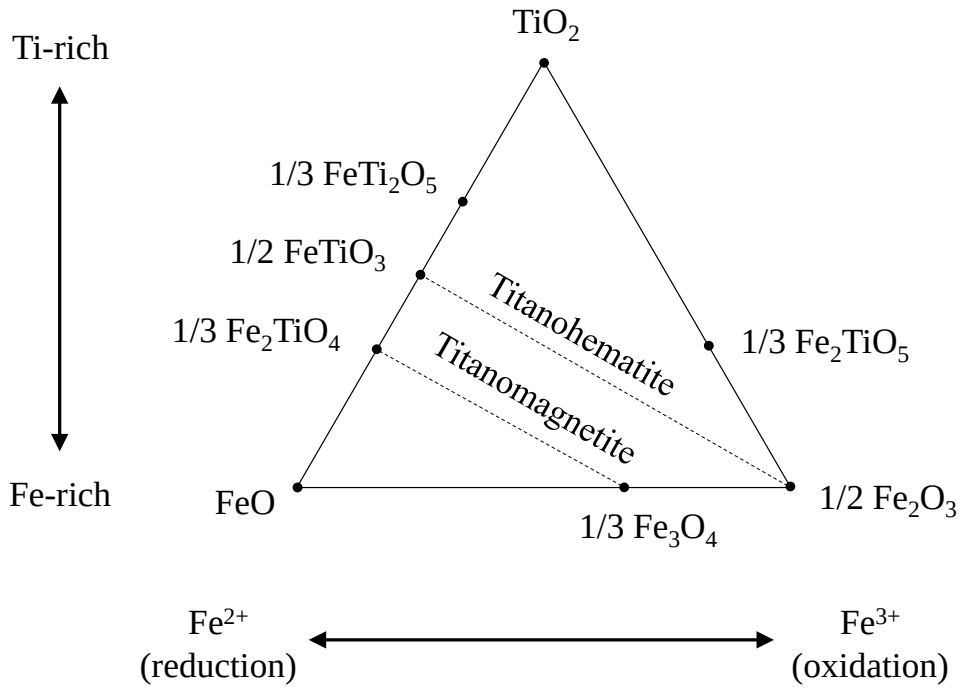

Fig. 1.2.4 TiO_2–FeO–Fe_2O_3 ternary diagram where vertical and horizontal arrowed lines indicate compositional Fe/Ti ration and the valence of Fe cations [8].

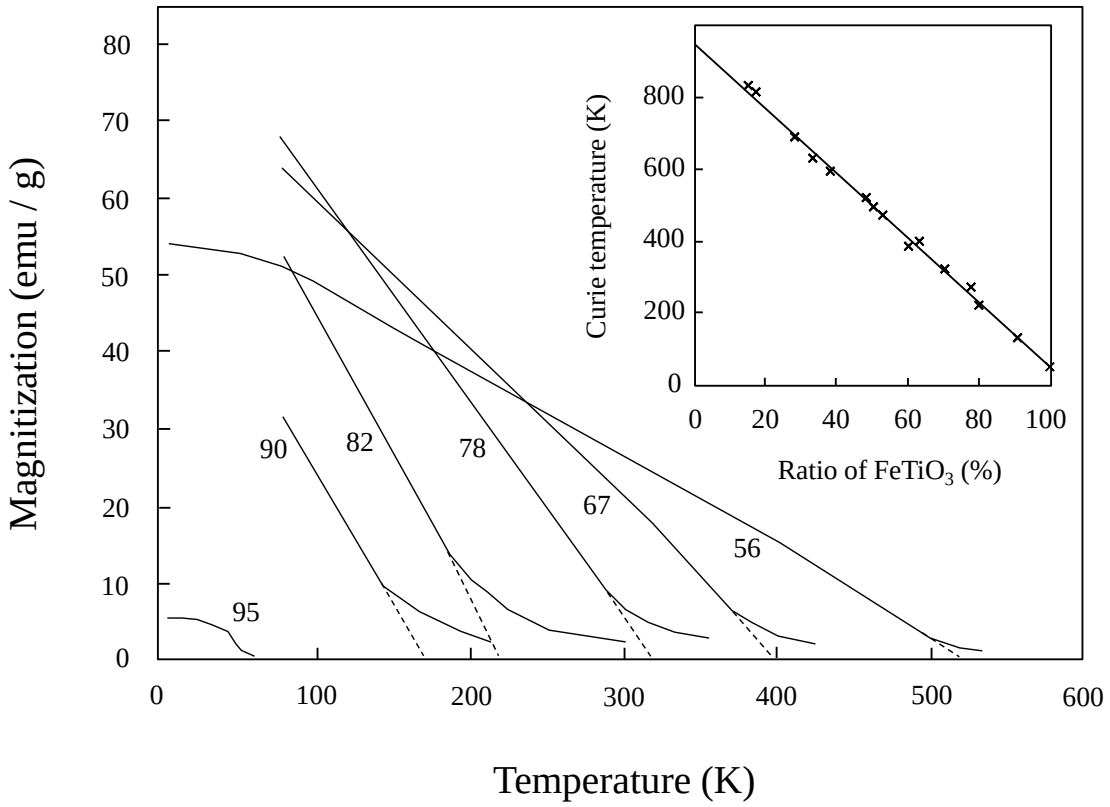

Fig. 1.2.5 The temperature-dependence of magnetization in $FeTiO_3$–Fe_2O_3 solid solution series. The subsidiary numbers of each line indicate the molar ratio of $FeTiO_3$ (%). Curie temperature of them is evaluated by extrapolating the linear part of the curve to the abscissa axis (the dashed lines). The inset shows a composition-dependence of Curie temperature in $FeTiO_3$–Fe_2O_3 solid solution series.

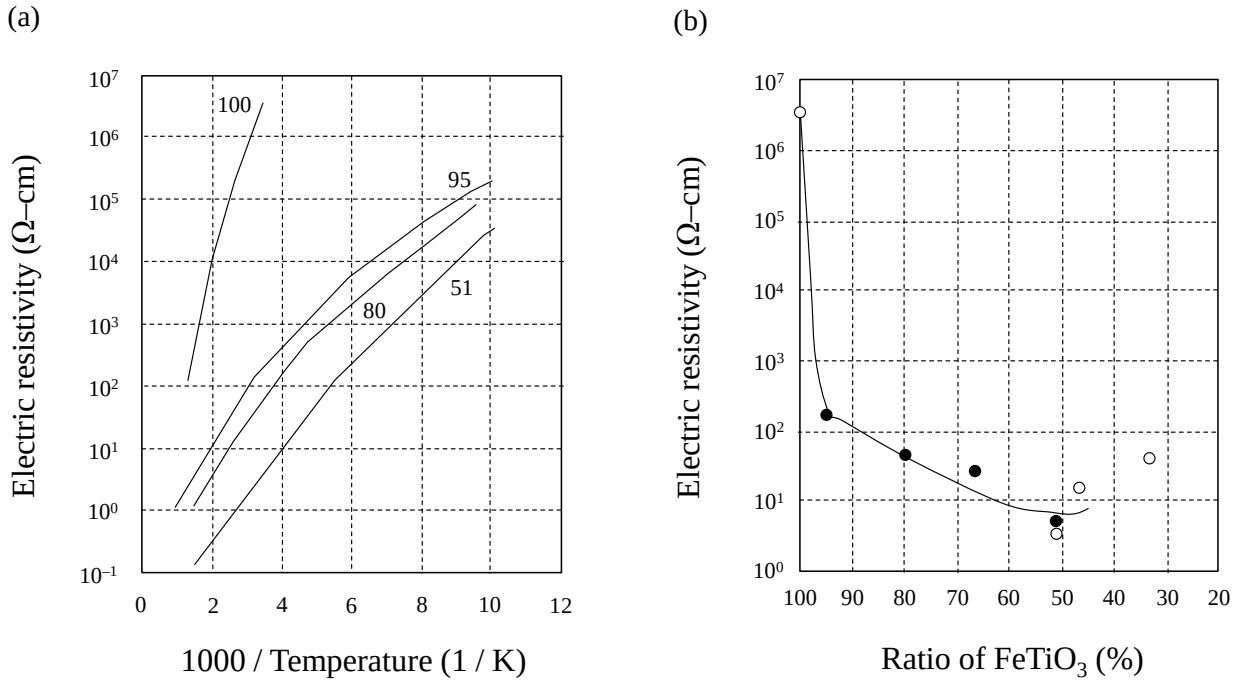

Fig. 1.2.6 (a) The temperature-dependence of electric resistivity in $FeTiO_3$–Fe_2O_3 solid solution series. The subsidiary numbers of each line indicate the molar ratio of $FeTiO_3$ (%). (b) The composition-dependence of electric resistivity in $FeTiO_3$–Fe_2O_3 solid solution series. Filled and open circles indicate ferromagnetic and antiferromagnetic specimens, respectively.

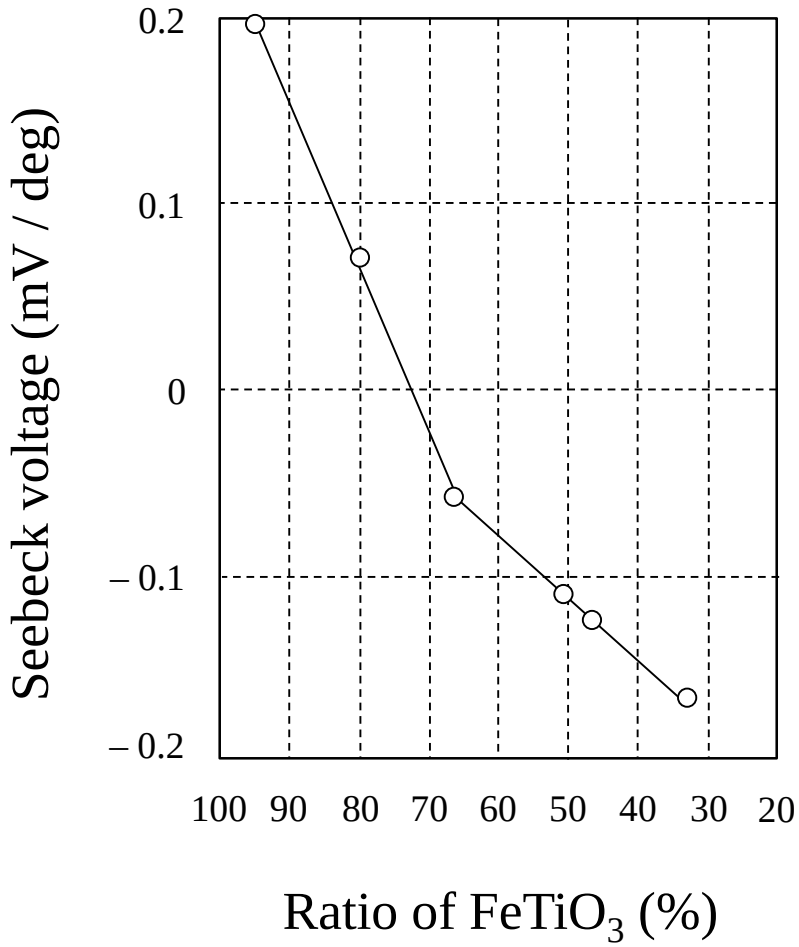

Fig. 1.2.7 The composition-dependence of Seebeck coefficient in $FeTiO_3$–Fe_2O_3 solid solution series.

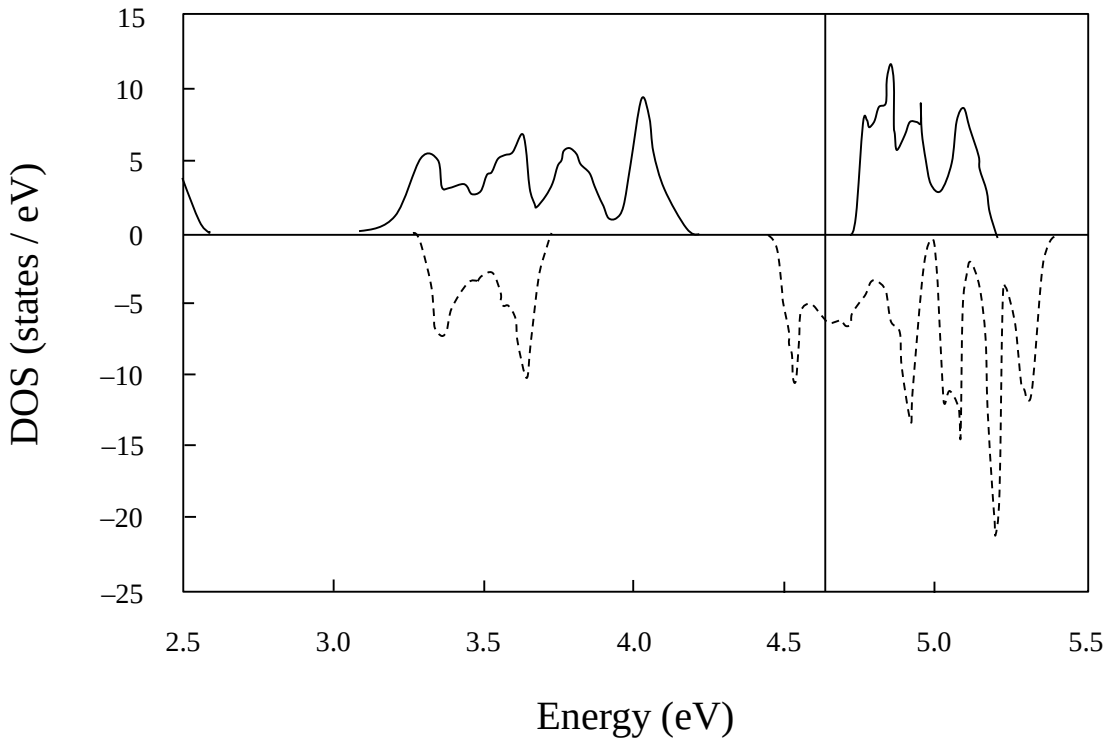

Fig. 1.2.8 The density of state diagram of $0.5FeTiO_3 \cdot 0.5Fe_2O_3$ solid solution. One spin channel shows insulating (solid line) whereas the other spin channel shows conducting (dashed line).

1.2.4. References

1. http://www.geocities.jp/kmo_mma/crystal/en/vesta.html
2. B. A. Wechsler, and C. T. Prewitt, *Am. Miner.* **69**, 176 (1984).
3. R. L. Blake, R. E. Hessevick, T. Zoltai, and L. W. Finger, *Am. Miner.* **51**, 123 (1966).
4. T. Nagata, and S. Akimoto, *Geofisica Pura e Applic. Milano* **34**, 36 (1956).
5. Y. Ishikawa, and S. Akimoto, *J. Phys. Soc. Jpn.* **12**, 1083 (1957).
6. Y. Ishikawa, *J. Phys. Soc. Jpn.* **13**, 37 (1958).
7. N.E. Brown, A. Navrotsky, G. L. Nord, and S. K. Banerjee, *Am. Miner.* **78**, 941 (1993).
8. R. F. Butler 'Paleomagnetism' http://www.geo.arizona.edu/Paleomag/book/chap02.pdf
9. A. F. Buddington, and D. H. Lindsley, *J. Petrol.* **4**, 138 (1964).
10. W. H. Butler, A. Bandyopadhyay, and R. Srinivasan, *J. App. Phys.* **93**, 7882 (2003).
11. F. Zhou, S. Kotru, and R. K. Pandy, *Thin Solid Films* **408**, 33 (2002).
12. T. Fujii, M. Kayano, Y. Takada, M. Nakanishi, and J. Takada, *J. Magn. Magn. Mater.* **272-276**, 2010 (2004).
13. T. Fujii, M. Kayano, Y. Takada, M. Nakanishi, and J. Takada, *Solid State Ionics* **172**, 289 (2004).
14. H. Hojo, K. Fujita, K. Tanaka, and K. Hirao, *Appl. Phys. Lett.* **89**, 082509 (2006).
15. H. Hojo, K. Fujita, K. Tanaka, and K. Hirao, *Appl. Phys. Lett.* **89**, 142503 (2006).
16. H. Hojo, K. Fujita, K. Tanaka, and K. Hirao, *J. Magn. Magn. Mater.* **310**, 2105 (2007).
17. K. Tanaka, K. Fujita, S. Nakashima, H. Hojo, and T. Matoba, *J. Magn. Magn. Mater.* **321**, 818 (2009).

Chapter 2. Low-temperature growth of highly crystallized ilmenite-hematite solid solution thin films with smooth surface morphology

2.1 lntroduction

As mentioned in Section 1.2.3, many studies have been already dedicated to the epitaxial growth of $FeTiO_3$–Fe_2O_3 solid solution thin films on α–Al_2O_3 (0001) substrates for spintronics device application [1–7]. However, there are no discussions on the surface morphology of prepared thin films, and/or the relationship between the deposition condition and the surface morphology of thin films has not been investigated. For device application, the smooth surface of thin films and sharp interface between thin film layers are required to realize high-performance device, because it is known that the surface roughness of thin films seriously degrades the carrier transport properties of device by scattering electrons at rough interface [8]. Therefore, the surface morphology of thin films should be smooth and the deposition condition of films also should be optimized in order to prepare thin films with smooth surface.

In this chapter, I fabricated $FeTiO_3$–Fe_2O_3 solid solution thin films with the composition ratio of 80% of $FeTiO_3$ ($0.8FeTiO_3{\cdot}0.2Fe_2O_3$) on α–$Al_2O_3$ (0001) substrates with varying the growth temperature from 700 ºC to 550 ºC, and obtained thin films with smoother surface morphology by reducing the growth temperature. The surface roughness is considered to be mainly due to the large lattice mismatch as large as around 6.2% between $0.8FeTiO_3{\cdot}0.2Fe_2O_3$ and α–Al_2O_3 (see Table. 2.1 for the lattice constants and lattice mismatch of them). When thin films with such a large lattice mismatch are fabricated at high growth temperature of 700 ºC, the deposited atoms on the substrate surface are thermally-activated and readily diffuse. This diffusion leads to relaxation of the lattice strain, resulting in a surface roughness including random dislocations and cracks. On the other hand, a reduction in growth temperature is considered to be effective to solve the surface morphology degradation, because the excess diffusion of atoms and the random lattice relaxation are expected to be suppressed at lower growth temperature. This

low-temperature growth is also considered to be suitable method for device application, because intermix of atoms at interface between thin film layers, which occur when they are exposed to high temperature during the fabrication process [11], will effectively suppressed at low temperature.

In this study, I report on the low-temperature growth of epitaxial thin films composed of $0.8FeTiO_3 \cdot 0.2Fe_2O_3$ using a PLD method. I have chosen this composition because ordered-phase of $0.8FeTiO_3 \cdot 0.2Fe_2O_3$ is stable within a wide range of temperature which is confirmed from the phase diagram of Reference [12] (see also Fig. 1.2.3 in Chapter 1). The ordered-phase epitaxial thin films having a flat surface can be fabricated by optimizing the growth temperature. Electric and magnetic properties of fabricated thin films are also discussed in comparison with those of bulk specimens.

2.2 Experimental procedure

2.2.1 Sample preparation

Thin films of $0.8FeTiO_3 \cdot 0.2Fe_2O_3$ composition were grown on α–Al_2O_3 (0001) substrates by a PLD method. The PLD targets were prepared by conventional solid-state reaction method. Powder reagents of α–Fe_2O_3 (Kojundo Chemical Laboratory Co. Ltd., purity: 99.99%) and TiO_2 (Kojundo Chemical Laboratory Co. Ltd., purity: 99.9%) were mixed with alumina mortar and pestle and heated in air at 900 ºC for 12 h. The mixture was re-grounded and pressed into pellets. The pellets were sintered in air at 1200 ºC for 24 h. In order to prepare a substrate with atomically flat surface, α–Al_2O_3 (0001) substrates (Shinkosha Co. Ltd.) are thermally annealed in air at 1000 ºC for 3h before being loaded on the PLD vacuum chamber. The high-density target and α–Al_2O_3 (0001) substrate with atomically flat surface were set in a vacuum chamber with a base pressure of 10^{-6} Pa. A KrF excimer laser (wavelength: 248 nm) was focused on the target with a fluence of 2 J/cm^2. The repetition frequency of excimer laser was fixed at 2 Hz. The oxygen partial pressure (P_{O_2}) was kept at 1.0×10^{-3} Pa, and the substrate temperature (T_S) was varied from 400 to 700 ºC. After the deposition was finished, samples were quenched from T_S to room temperature in the vacuum chamber in order to prevent them from dissolving into their end members; ilmenite ($FeTiO_3$) and hematite (α–Fe_2O_3) [12, 13].

2.2.2 Sample characterizations

The crystal phase of sintered targets was confirmed by powder X-ray diffraction (XRD) measurements with Cu Kα radiation (RINT2500, Rigaku). An energy dispersive X-ray spectrometry (EDS) (EMAX, Horiba) revealed that the composition ratio between Fe and Ti elements of the targets equaled to uniformly $0.8FeTiO_3 \cdot 0.2Fe_2O_3$ across the wide range of target surface.

The film thickness was evaluated to be about 70 nm using a surface profiler. The composition of thin films was determined by Rutherford backscattering measurement (RBS) followed by the fitting simulation using SIMNRA 5.02 software program [14]. The crystal structure was analyzed by both out-of-plane and in-plane XRD measurements with Cu Kα radiation (ATX-G, Rigaku). Fig. 2.1 (a) illustrates the crystal structure and crystallographic axes of $FeTiO_3$–Fe_2O_3 solid solution and α–Al_2O_3 and one can see that their $(11\bar{2}0)$ planes (A-planes) are perpendicular to their (0001) planes (C-planes). Therefore, *c*- and *a*-axis directions of solid solution thin films are normal and parallel to the substrate surface respectively, when they are grown on α–Al_2O_3 (0001) substrates [In contrast, *c*-axis of solid solution thin films is parallel to the substrate surface when they are grown on α–Al_2O_3 $(11\bar{2}0)$ substrates as in Chapter 4]. In this study, I have analyzed the crystal structure of both C- and A-plane of solid solution thin films in order to confirm the epitaxial growth of thin films and determine the crystallographic relationship between thin films and substrates. The surface morphology of thin films was observed using an atomic force microscope (AFM) (SII Nano Technology, SPI3800N). The measurements of magnetization were carried out using a superconducting quantum interference device (SQUID) magnetometer (MPMS, Quantum Design). The electric resistivity was measured by the van der Pauw method (Resitest8300, Toyo). Measurements of the Seebeck coefficient were carried out at room temperature.

2.3 Results and Discussion

2.3.1 XRD pattern of PLD target

Fig. 2.2 shows the powder XRD pattern of PLD target sintered in air. The target contains two crystalline phases of pseudobrookite (Fe_2TiO_5) and rutile (TiO_2). Although the target is

not a single phase of $0.8FeTiO_3 \cdot 0.2Fe_2O_3$, the Fe and Ti atoms are considered to be distributed uniformly inside the pellet and the composition ration between Fe and Ti can be regarded as almost the same as $0.8FeTiO_3 \cdot 0.2Fe_2O_3$ single phase target as revealed from EDS study. If not otherwise specified, this kind of PLD target is utilized in other experimental in this dissertation.

2.3.2 Composition, crystalline and surface analyses of fabricated thin films

Fig. 2.3 shows RBS data on the thin film grown under $P_{O_2} = 1.0 \times 10^{-3}$ Pa and T_S = 550 ºC. The composition ratio between Fe and Ti ions was estimated to be Fe : Ti = 1.467 : 1.000, and this indicates that the composition of fabricated thin film is $0.81FeTiO_3 \cdot 0.19Fe_2O_3$. The similar results were obtained on thin films grown at different T_S conditions.

Fig. 2.4 (a) shows the out-of-plane XRD patterns of $0.8FeTiO_3 \cdot 0.2Fe_2O_3$ thin films. When $T_S \geq$ 500 ºC, 0003 and 0009 reflections, which are absent in the case of disordered phase, are clearly observed in addition to 0006 and 00012 ones, indicating the formation of ordered phase of (0001)-oriented $FeTiO_3$-Fe_2O_3 solid solution (space group: $R\bar{3}$). In contrast, when T_S = 400 and 450 ºC, only 0006 and 00012 reflections ascribed to the disordered phase (space group: $R\bar{3}c$) are detected. This is probably due to the insufficient heat supply which prevents atoms from diffusing on the film surface to arrange into the ordered phase. Fig. 2.4 (b) represents a magnified image of 0006 peaks in Fig. 2.4 (a). For thin films grown at T_S = 500 and 550 ºC, Pendellösung fringes are clearly observed, indicating the high crystallinity and smooth surface morphology of these films. The 0006 reflection peaks are located at lower 2θ values relative to those of the other films. It is evident that thin films grown at T_S = 500 and 550 ºC elongate along [0001] direction, due to the in-plane compressive strain imposed by the lattice mismatch (see Table. 2.1). For films grown at higher T_S, the peak position is shifted to the higher 2θ values, which suggests the lattice relaxation. On the other hand, the peak position is also shifted to the higher 2θ values when T_S is decreased from 500 ºC. This is not due to the strain relaxation but attributable to the presence of excess Fe^{3+}, since oxidation preferentially takes place at lower temperatures. Because of the smaller ionic radius of Fe^{3+} relative to that of Fe^{2+}, it is considered that the lattice constant becomes shorter for thin films grown at lower T_S (< 500 ºC).

In-plane XRD measurements (Fig. 2.5), which were carried out along the *a*-axis of α–Al_2O_3

(0001) substrates, exhibit only $11\bar{2}0$ and $22\bar{4}0$ peaks, corresponding to A-plane reflections of the films. Namely, thin films are grown epitaxially on α–Al_2O_3 (0001) substrates. The orientation relationship is as follow; $0.8FeTiO_3 \cdot 0.2Fe_2O_3$ (0001)[$11\bar{2}0$]//α–Al_2O_3 (0001)[$11\bar{2}0$]. When T_S = 550 and 500 ºC, the $11\bar{2}0$ reflection peaks are located at higher 2θ values relative to the peak position of the thin film deposited at T_S = 700 ºC, confirming the in-plane compression as discussed in out-of-plane XRD study.

Fig. 2.6 displays the AFM images of the films. In decreasing T_S from 700 to 500 ºC, the film surface tends to be smoother without any pits; the root-mean-squared (rms) roughness decreases with decreasing the growth temperature. This tendency agrees with the result of XRD patterns as shown in Fig. 2.4 (b), where Pendellösung fringe patterns appear for the films grown at T_S = 550 and 500 ºC.

2.3.3 Physical properties of fabricated thin films

Fig. 2.7 (a) illustrates the temperature dependence of magnetization, $M(T)$, for thin films fabricated at various T_S. The measurements were performed under a field-cooled condition while an external magnetic field (H) of 8500 Oe was applied parallel to the film surface. The films with ordered phase grown at T_S = 700, 550, and 500 ºC exhibit an increase in M with a decrease in T, indicating a ferrimagnetic ordering. Both of the films grown at T_S = 500 and 550 ºC possess T_C of about 245 K, comparable to the value of bulk specimen (T_C = 234 K) [16]. On the other hand, T_C of the film grown at T_S = 700 ºC is as high as 290 K. The T_C higher than the bulk value may be ascribed to the excess amount of Fe^{2+} ions caused by higher T_S, since Fe^{2+} ions contribute to a net increase in M for the solid solution. For the film with the disordered phase (T_S = 400 ºC), M is very small and shows no T-dependence, indicating that the film is antiferromagnetic. The in-plane M-H curves measured at 100 K in Fig. 2.7 (b) also confirm the ferrimagnetic and antiferromagnetic properties of the ordered and disordered phases, respectively.

The temperature dependence of electric resistivity, $\rho(T)$, is shown in Fig. 2.8 for the thin films of ordered-phase grown at T_S = 500, 550, and 700 ºC. The log ρ vs. 1000/T plot exhibits a linear relationship which indicates an Arrhenius type dependence of $\rho(T)$, and this behavior is similar to that of the bulk specimen reported by Ishikawa [17] (see also Fig. 1.2.6). The

Seebeck coefficients were +43, +75, and +31 μVK^{-1} for the thin films of order phase grown at T_S = 500, 550, and 700 ºC, respectively. The positive Seebeck coefficients indicate the *p*-type conduction as expected from the composition [17]. Therefore, the physical properties of obtained thin films are still equivalent to those of bulk specimens even when the films have been grown at lower growth temperature.

2.4 Conclusion

$0.8FeTiO_3 \cdot 0.2Fe_2O_3$ thin films were grown on α–Al_2O_3 (0001) substrates at T_S between 400 and 700 ºC ($Po_2 = 1.0 \times 10^{-3}$ Pa). The thin films with ordered phase can be fabricated in the T_S range from 500 to 700 ºC. Especially, thin films with a smooth surface can be obtained at T_S = 500 and 550 ºC and their physical properties are similar to those of bulk specimen. The result indicates that careful control of atomic diffusion process during the growth stabilizes the ordered phase of solid solution while minimizing dislocation formation through lattice relaxation, improving the crystallinity in the film. The solid solution thin films grown at T_S = 500 and 550 ºC are expected to be more suitable for the spintronics device implementation because of their flat surfaces and the lower growth temperature which can prevent atomic intermixture at interface between different thin film layers during fabrication process.

Table. 2.1 Space group, lattice constant and lattice mismatch of $0.8FeTiO_3 \cdot 0.2Fe_2O_3$ solid solution and α–Al_2O_3.

Material	Space group	Lattice constant	Lattice mismatch against α–Al_2O_3 *
α–Al_2O_3	$R\bar{3}c$	a = 4.760 Å, c = 12.993 Å [9]	——
$0.8FeTiO_3 \cdot 0.2Fe_2O_3$	$R\bar{3}$	a = 5.078 Å, c = 13.985 Å [10]	– 6.26% (in C-plane) – 7.09% (in A-plane)

* Lattice mismatch is calculated as; $\{(a_{sub} - a_{film}) / a_{film}\} \times 100$,
where a_{sub} and a_{film} indicate the lattice constant of substrate and thin film, respectively.

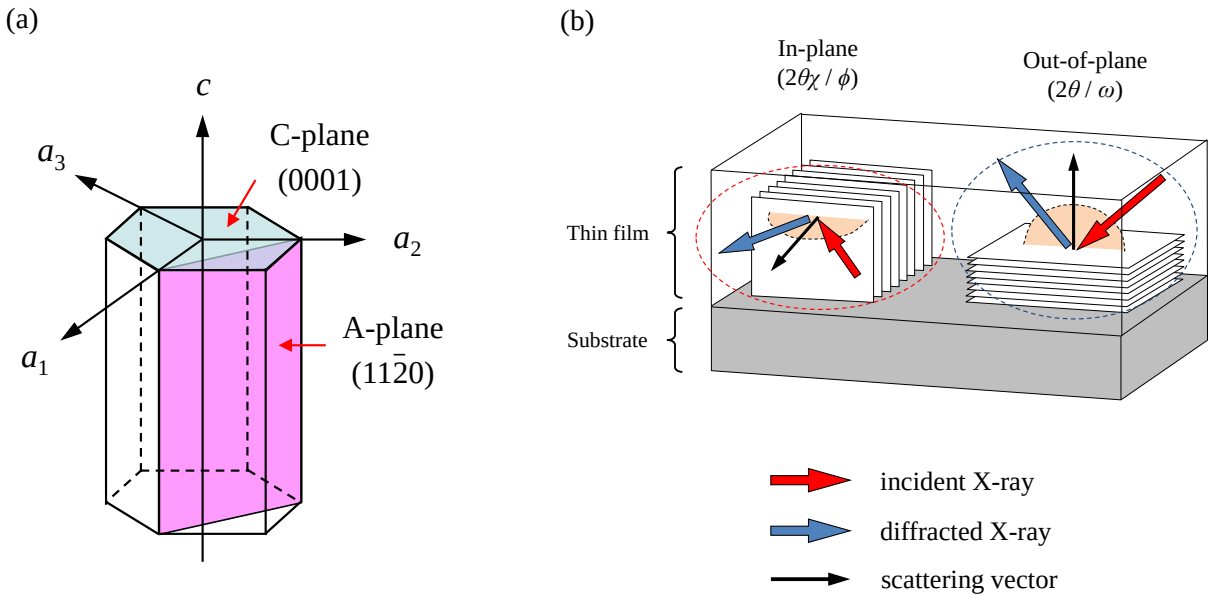

Fig. 2.1 (a) The crystal structure and crystallographic axes of $FeTiO_3$–Fe_2O_3 solid solution and α–Al_2O_3. Their (11$\bar{2}$0) planes (A-planes) and (0001) planes (C-planes) are indicated by translucent red and blue planes, respectively. (b) The schematic illustration of out-of-plane and in-plane XRD analysis carried out in this study.

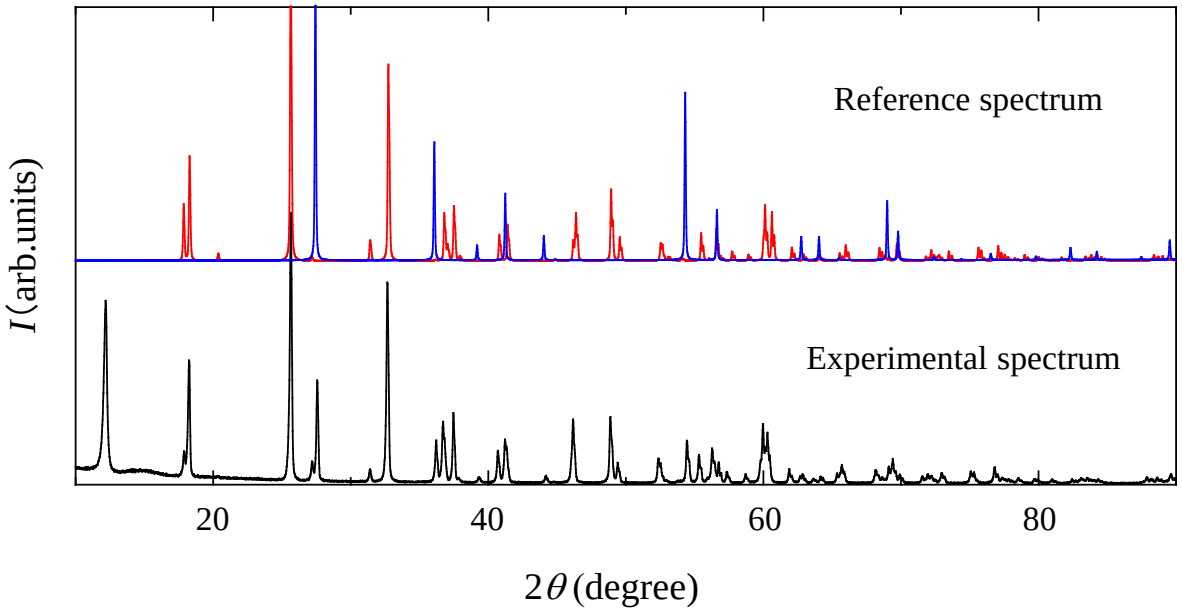

Fig. 2.2 Powder XRD pattern of PLD target sintered in air (the lower side) and reference XRD patterns of Fe_2TiO_5 (red line) and TiO_2 (blue line) (the upper side). The reference patters are cited from FindIt program [15]. The peak observed at $2\theta = 12^{o}$ in the experimental spectrum is due to a sample holder.

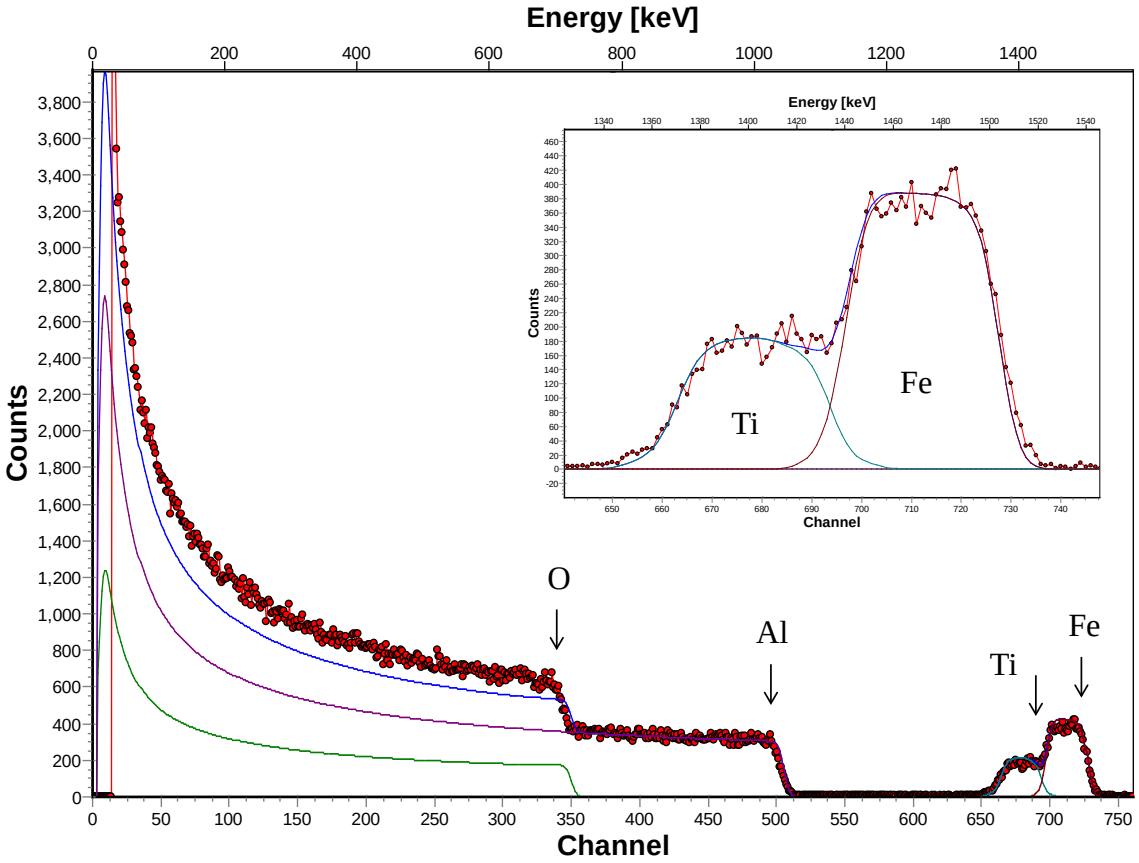

Fig. 2.3 RBS experimental spectrum (red filled-circles) of the thin film grown under Po_2 = 1.0 × 10^{-3} Pa and T_S = 550 ºC. The experimental RBS spectrum was fitted with the theoretical spectrum calculated by the SIMNRA 5.02 program (blue solid-line) [14].

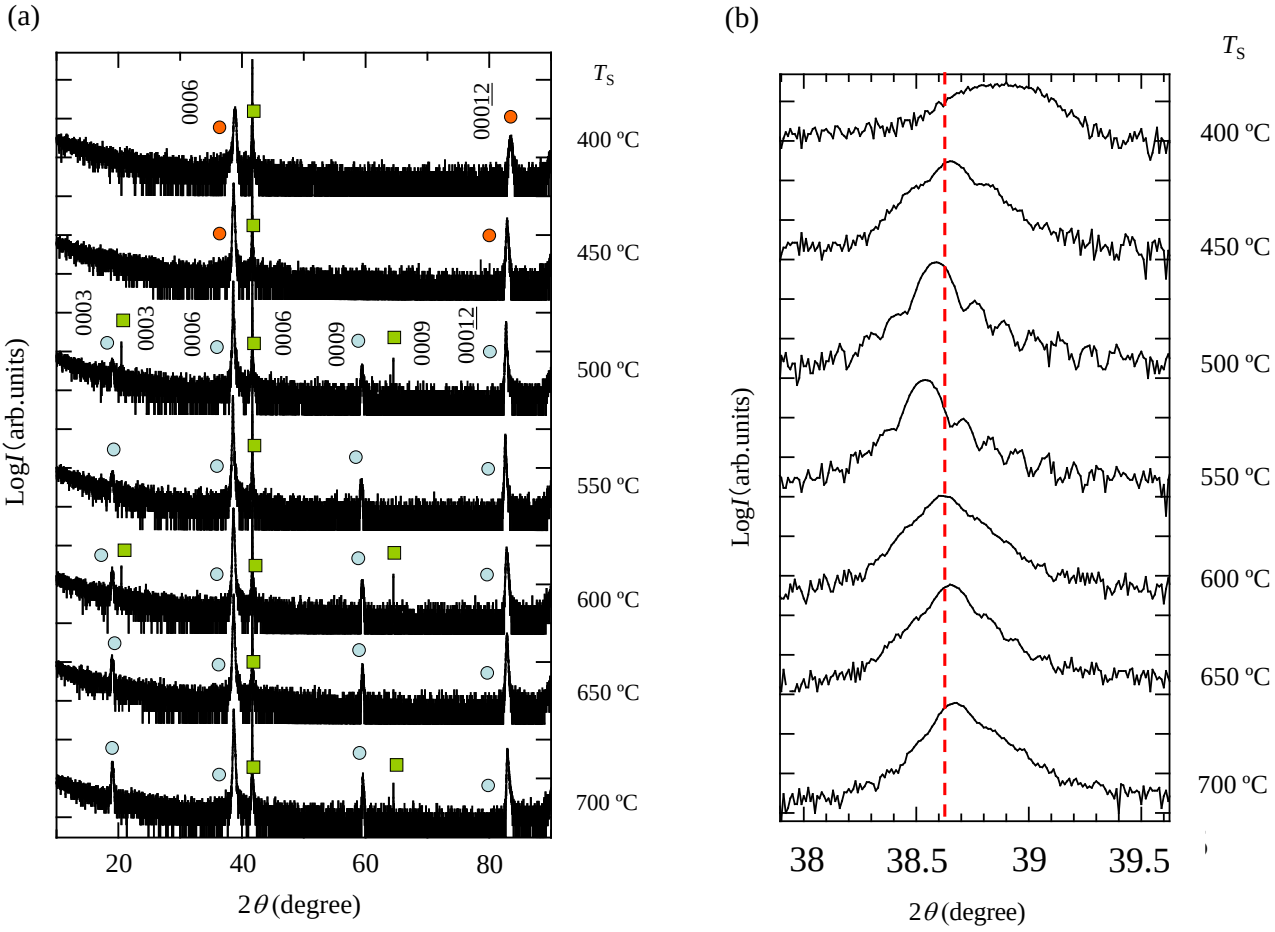

Fig. 2.4 (a) Out-of-plane XRD patterns of solid solution thin films grown at T_S = 400-700 ºC; ■ : α–Al_2O_3 substrate, ○ : ordered phase, ● : disordered phase. (b) Magnified image of 0006 peaks displayed in Fig. 2.4 (a).

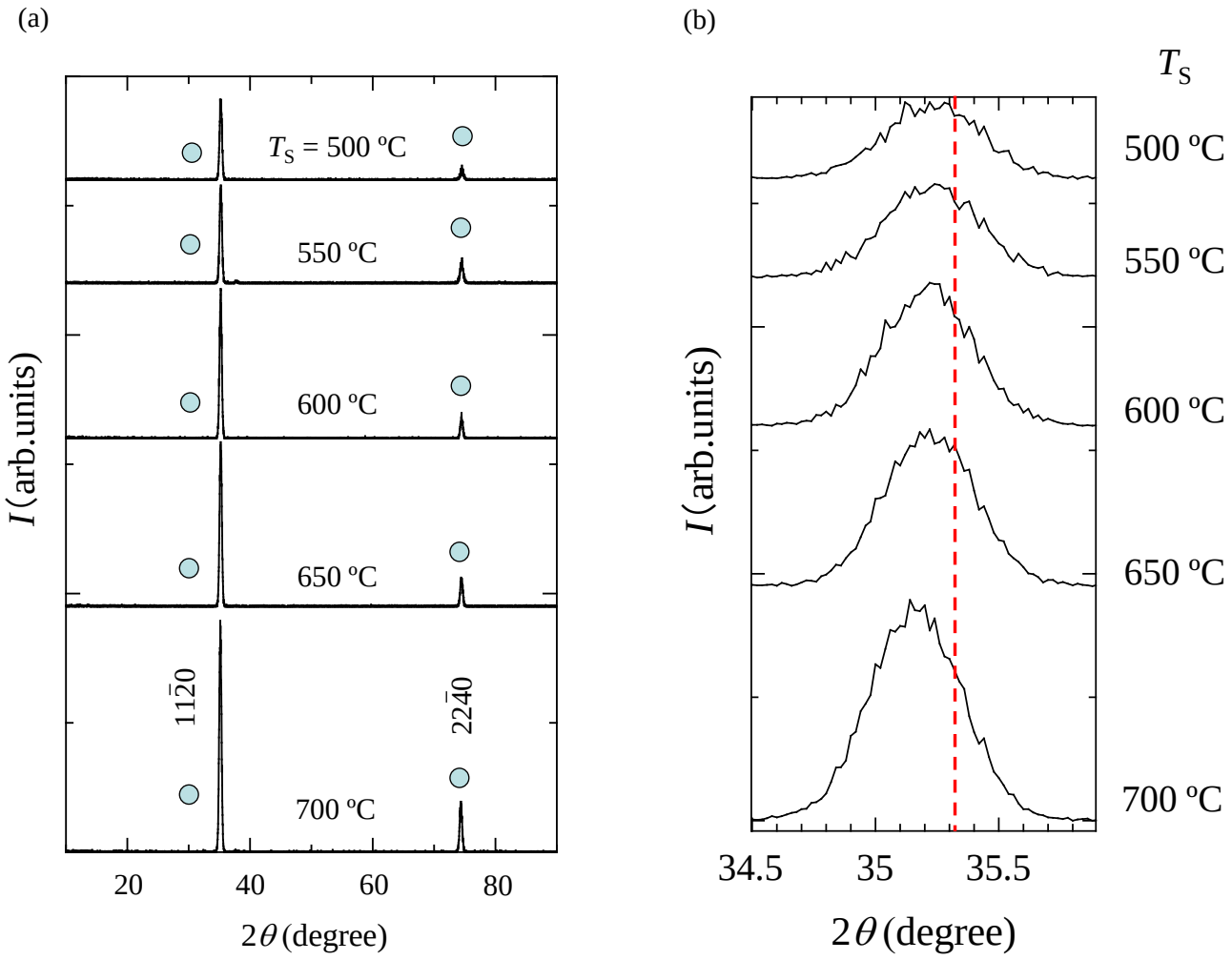

Fig. 2.5 (a) In-plane XRD patterns for solid solution thin films grown at T_S = 500–700 ºC; ○ : ordered phase. (b) Magnified image of $11\bar{2}0$ peaks displayed in Fig. 2.5 (a).

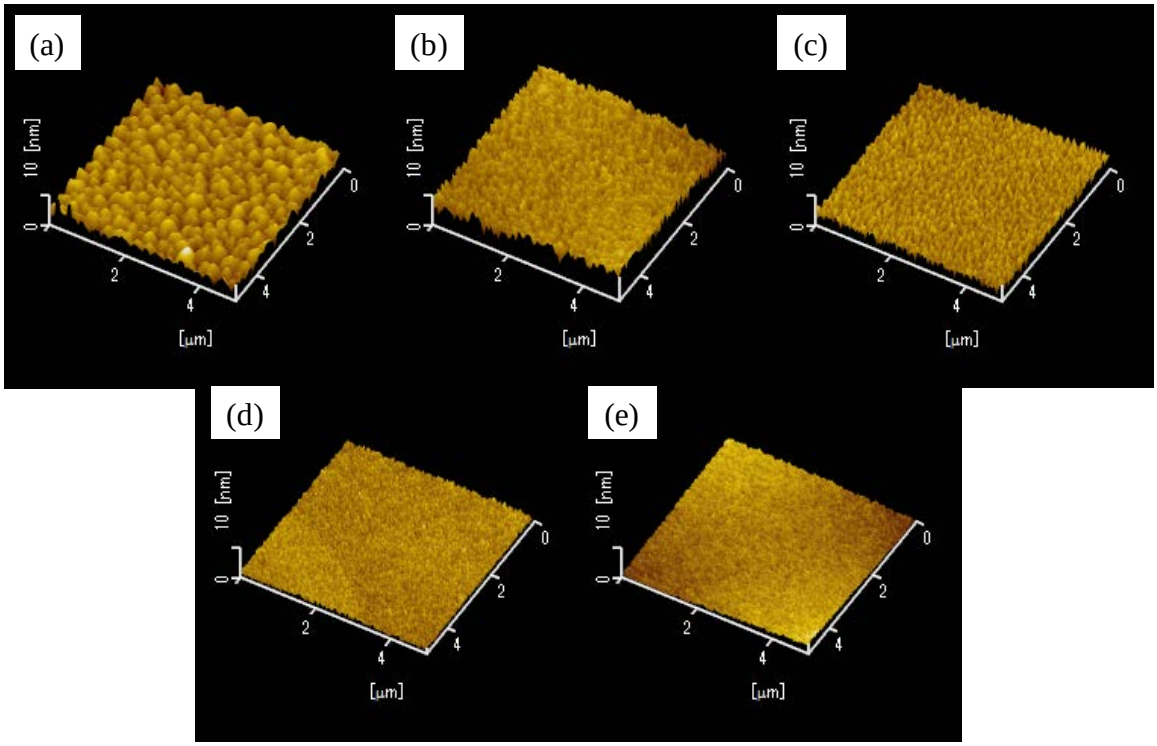

Fig. 2.6 AFM images for the solid solution thin films grown at T_S = 700 ºC (rms = 0.943 nm) (a), 650 ºC (rms = 1.42 nm) (b), 600 ºC (rms = 0.786 nm) (c), 550 ºC (rms = 0.452 nm) (d), and 500 ºC (rms = 0.486 nm) (e).

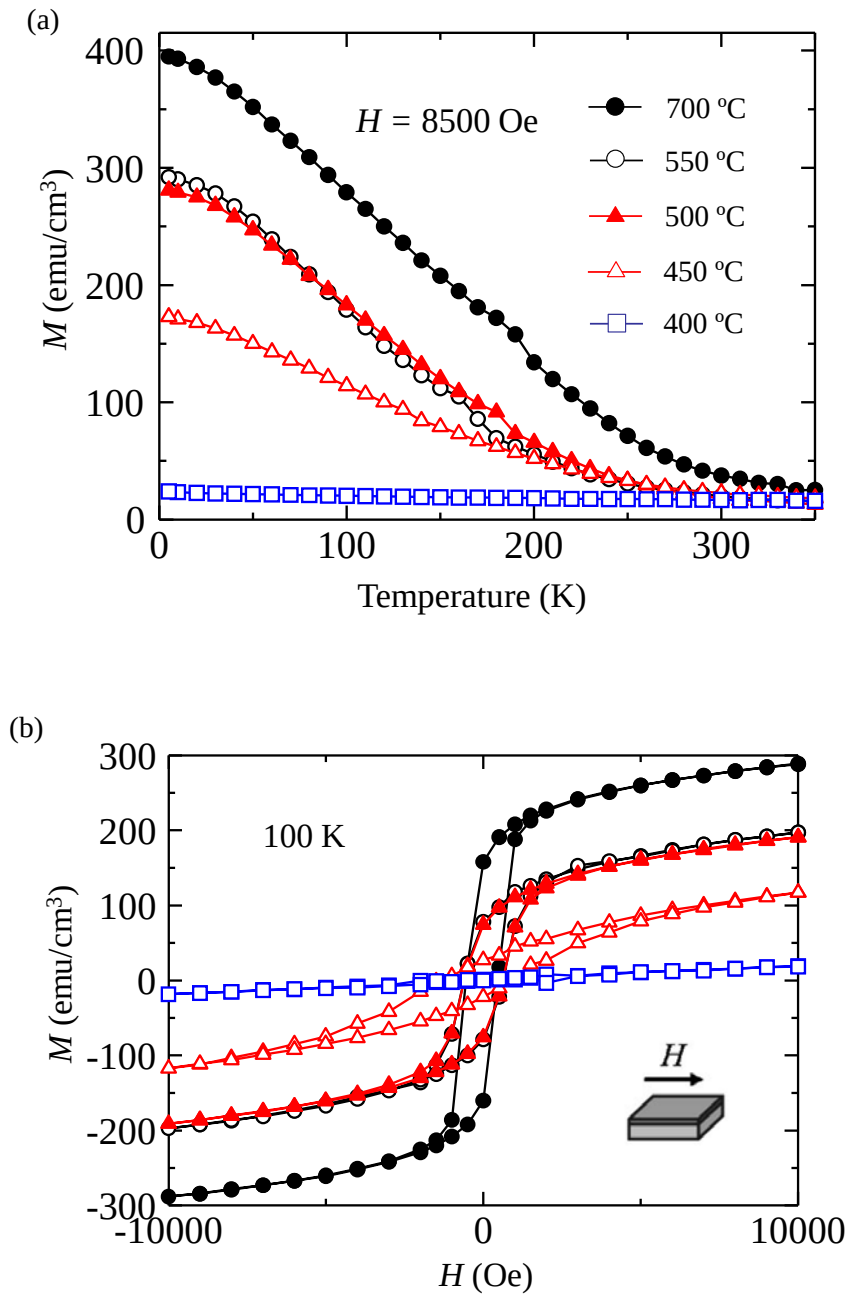

Fig. 2.7 (a) M-T curves for the thin films with ordered and disordered phases. The external magnetic field of 8500 Oe was applied parallel to the film surface. (b) M-H curves at 100 K.

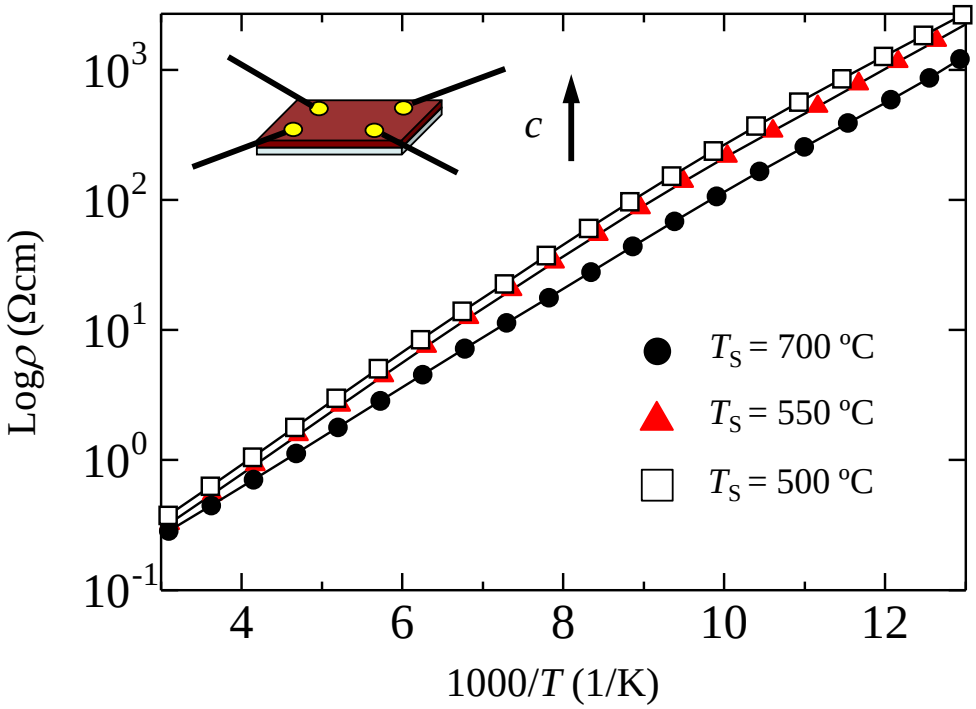

Fig. 2.8 Reciprocal T-dependence of ρ for thin films of order-phase.

2.5 References

1. F. Zhou, S. Kotru, and R. K. Pandy, *Thin Solid Films* **408**, 33 (2002).
2. T. Fujii, M. Kayano, Y. Takada, M. Nakanishi, and J. Takada, *J. Magn. Magn. Mater.* **272-276**, 2010 (2004).
3. T. Fujii, M. Kayano, Y. Takada, M. Nakanishi, and J. Takada, *Solid State Ionics* **172**, 289 (2004).
4. H. Hojo, K. Fujita, K. Tanaka, and K. Hirao, *Appl. Phys. Lett.* **89**, 082509 (2006).
5. H. Hojo, K. Fujita, K. Tanaka, and K. Hirao, *Appl. Phys. Lett.* **89**, 142503 (2006).
6. H. Hojo, K. Fujita, K. Tanaka, and K. Hirao, *J. Magn. Magn. Mater.* **310**, 2105 (2007).
7. K. Tanaka, K. Fujita, S. Nakashima, H. Hojo, and T. Matoba, *J. Magn. Magn. Mater.* **321**, 818 (2009).
8. S. Yuasa, T. Nagahama, A. Fukushima, Y. Suzuki, and K. Ando, *Natue Mater.***3**, 868 (2004).
9. J. Lewis, D. Schwarzenbach, and H. D. Flack, *Acta Cryst.* A**38** 733 (1982).
10. R. J. Harrison, S. A. T. Redfern, and R. I. Smith, *Am. Mineral.* **85**, 194 (2000).
11. G. B. Alers, D. J. Werder, Y. Chabal, H. C. Lu, E. P. Gusev, E. Garfunkel, T. Gustafsson, and R. S. Urdahl, *Appl. Phys. Lett.* **73**, 1517 (1998).
12. N.E. Brown, A. Navrotsky, G. L. Nord, and S. K. Banerjee, *Am. Miner.* **78**, 941 (1993).
13. B.P. Burton, and P.M. Davidson, *Multicritical phase relations in minerals*. in S. Ghose, J.M.D. Coey, and E. Salje, Eds., *Structural and magnetic phase transitions in minerals*, p. 60-90. Springer-Verlag, New York (1988).
14. http://home.rzg.mpg.de/~mam/index.html
15. http://www.jaici.or.jp/wcas/wcas_icsd.htm
16. Y. Ishikawa, J. Phys. Soc. Jpn. **12**, 1083 (1957).
17. Y. Ishikawa, J. Phys. Soc. Jpn. **13**, 37 (1958).

Chapter 3. Ilmenite-hematite solid solution thin films with atomically smooth surface grown on C-plane sapphire substrates

3.1 lntroduction

In Chapter 2, the low-temperature growth of thin films composed of ordered-phase of $0.8FeTiO_3 \cdot 0.2Fe_2O_3$ solid solution on C-plane sapphire [α–Al_2O_3 (0001)] substrates was introduced, and it revealed that thin films with relatively flat surface could be obtained by reducing the growth temperature due to the suppression of excess migration of atoms on thin film surface. As I mentioned there, this low-temperature growth is considered to be a useful method for fabrication of spintronics device consisting of multi-layer film structure such as magnetic tunneling junction, because it will prevent atomic intermixture at interface during the fabrication process.

On the other hand, thin films generally tend to be fabricated by step-flow growth, which can lead to thin films with 'atomically flat' step-and-terrace surface structure, at extremely high growth temperature (usually more than 800 ºC), if substrates are thermally and chemically stable even at that high growth temperature [1]. Here, I introduce one of those kinds of step-flow thin film growths called 'Domain-Matching Epitaxy' (DME) [2] for preparing high-quality $FeTiO_3$–Fe_2O_3 solid solution thin films with atomically flat surface. The combination of low-temperature and DME growth is expected to be a useful method for fabrication of flawless spintronics devices. In this chapter, I fabricated epitaxial $0.8FeTiO_3 \cdot 0.2Fe_2O_3$ solid solution thin films with atomically flat surface on α–Al_2O_3 (0001) substrates by pulsed-laser deposition (PLD) method with high-growth temperature more than 850 ºC. I have also chosen this composition due to the thermal stableness of ordered-phase of $0.8FeTiO_3 \cdot 0.2Fe_2O_3$ solid solution as the same reason in Chapter 2 [3]. I observed the crystal structure at the interface between thin film and substrate by cross-sectional high-resolution transmission electron microscopy (HR-TEM) in order to investigate DME growth mechanism in

$FeTiO_3$–Fe_2O_3/α–Al_2O_3 (0001) system. The explanation and discussion on DME will be given at Section 3.3.2. The physical properties of fabricated thin films were also investigated and compared to those of bulk specimens reported by Ishikawa [4, 5].

3.2 Experimental procedure

3.2.1 Sample preparation

Thin films were fabricated by PLD method. The preparation condition of PLD targets with $0.8FeTiO_3 \cdot 0.2Fe_2O_3$ composition and thermal annealing condition of α–Al_2O_3 (0001) substrates were the same as described in Chapter 2. KrF excimer laser (λ = 248 nm, ~2.5 J/cm^2) was focused on the targets at the repetition of 2 Hz. The oxygen partial pressure (Po_2) and substrate temperature (T_S) were varied from 1.0×10^{-3} to 1.5×10^{-3} Pa and from 850 to 925 ºC, respectively.

3.2.2 Sample characterization

The characterizations of fabricated thin films were the same as described in Chapter 2. The film thickness was evaluated to be about 75 nm using a surface profiler. The composition of thin films determined by Rutherford backscattering measurement (RBS) followed by the fitting simulation using SIMNRA 5.02 software program [6], and it was revealed that thin films fabricated from $0.8FeTiO_3 \cdot 0.2Fe_2O_3$ composition target included $0.87FeTiO_3 \cdot 0.13Fe_2O_3$ composition. The crystal structure was analyzed by both out-of-plane (for C-plane of thin films) and in-plane (for A-plane) XRD measurements with Cu Kα radiation (ATX-G, Rigaku) in order to determine the epitaxial relationship between thin films and substrates. The surface morphology of thin films was observed using an atomic force microscope (AFM) (SII Nano Technology, SPI3800N). The crystal structure at the interface between thin film and substrate was observed by cross-sectional HR-TEM (JEM-2100F, JEOL). The measurements of magnetization were carried out using a superconducting quantum interference device (SQUID) magnetometer (MPMS, Quantum Design). The electric resistivity was measured by the van der Pauw method (Resitest8300, Toyo). Measurements of the Seebeck coefficient were carried out at room temperature.

3.3 Results and Discussion

3.3.1 Crystalline and surface analyses of fabricated thin films

Fig. 3.1 shows out-of-plane (C-plane) XRD patterns of thin films grown at various deposition conditions. From Fig. 3.1 (a), no impurities were detected and all of 000*3n* (*n* = 1–4) peaks were observed along *c*-axis of α–Al_2O_3 (0001) at all described deposition conditions. As I explained in Chapter 2, the diffractions from 0003 and 0009 appear only in the case of ordered phase, and disappear in disordered phase [7–10]. Therefore, the formation of single phase of ordered $FeTiO_3$–Fe_2O_3 solid solution was confirmed. From a magnified image of 0006 peaks of thin film grown at P_{O_2} = 1.5 × 10^{-3} Pa and T_S = 925 ºC [Fig. 3.1 (b)], Pendellösung fringe, which indicates the high crystallinity and smooth surface morphology of thin films, is also observed at specific growth condition.

In-plane (A-plane) XRD patterns of corresponding thin films are shown in Fig. 3.2, and the diffraction patterns from $11\bar{2}0$ and $22\bar{4}0$ derived from A-plane of $FeTiO_3$–Fe_2O_3 were observed along *a*-axis of α–Al_2O_3 (0001) substrate. This means that thin films were grown epitaxially on the α–Al_2O_3 (0001) substrates under all deposition condition, and the epitaxial relationship is considered to be as follows; $[0001]_{film}//[0001]_{substrate}$ and $[11\bar{2}0]_{film}//[11\bar{2}0]_{substrate}$. From these out-of-plane and in-plane XRD patterns, I can safely say that thin films with single phase of ordered phase were epitaxially grown on α–Al_2O_3 (0001) substrate.

AFM images of surface structure for fabricated thin films are listed in Fig. 3.3. Although previous out-of-plane and in-plane XRD patterns indicated that epitaxial thin films with single phase of ordered-phase were grown on α–Al_2O_3 (0001) substrates with all deposition conditions, their surface structures were quite different from each other. With carefully controlling P_{O_2} and T_S, thin films with step-and-terrace surface structure could be prepared at P_{O_2} = 1.5 × 10^{-3} Pa and T_S = 925 ºC as illustrated in Fig. 3.3 (d), and this result corresponds to the Pendellösung fringe observed in out-of-plane XRD spectrum for the same thin film as in Fig. 3.1 (b). One step height of this thin film is estimated to be 0.47 nm [Fig. 3.3 (e)] which is equal to one charge-neutral unit of $FeTiO_3$ (0.45 nm) as illustrated in Fig. 3.3 (f), indicating that the surface of this thin film is said to be atomically smooth.

3.3.2 Cross-sectional HR-TEM observation at the interface and DME mechanism

From above XRD and AFM studies, ordered-phase of $FeTiO_3$–Fe_2O_3 solid solution thin films with atomically smooth surface were epitaxially grown on α–Al_2O_3 (0001) substrates, although there is a large lattice mismatch of 6.2% between thin film and substrate (lattice constants and lattice mismatch of $FeTiO_3$–Fe_2O_3 solid solution and α–Al_2O_3 are listed in Table. 2.1). I consider that the thin films were grown by DME growth introduced by Narayan *et al.* [2], in which the integer multiple of lattice constants of thin film and substrate is matching across the interface and the lattice strain is relaxed in the initial stage of thin film growth as indicated by Fig. 3.4 (a). Generally, fabrication of epitaxial thin films on substrates becomes difficult, and texture or polycrystalline thin films tend to be grown preferentially, when the lattice mismatch between thin film and substrate is more than 7–8% [12]. However, many thin film/substrate systems possessing quite large lattice mismatch, including TiN/Si (100) (lattice mismatch of 25%) [13] and ZnO/α–Al_2O_3 (0001) (17%) [14] are epitaxially grown via DME growth, and the present $FeTiO_3$–Fe_2O_3/α–Al_2O_3 (0001) system with high-quality of crystallinity and surface morphology is also considered to be grown by DME mechanism.

In order to investigate the lattice-strain relaxation mechanism in $FeTiO_3$–Fe_2O_3/α–Al_2O_3 (0001) system, I conducted a cross-sectional HR-TEM observation of the interface between thin film and substrate as shown in Fig. 3.4 (b). Fig. 3.4 (c) is the corresponding Fourier-filtered TEM image of Fig. 3.4 (b), and one can see that misfit dislocation appears every 13–16 units of thin film. This is because the 15 units of *a*-lattice constant of $FeTiO_3$–Fe_2O_3 thin film (5.078 × 15 = 76.170 Å) are well agreed to the 16 units of that of α–Al_2O_3 substrate (4.760 × 16 = 76.160 Å). The margin between the lattice lengths of these domains is 76.170 – 76.160 = 0.010 Å, which is much smaller that of single unit cell (5.078 – 4.760 = 0.318 Å). When T_S is high enough for ablated species to obtain sufficient thermal energy, thin films is considered to be grown by step-flow growth mechanism and the lattice strain from substrate is also considered to be relaxed by DME. Because the lattice strain is relaxed in the initial stage of growth, there are no random cracks or dislocations, which cause degradation of crystallinity and surface morphology of thin films, during the thin film growth process.

As I will introduce Chapter 4, $FeTiO_3$–Fe_2O_3 solid solution thin films with step-and-terrace surface morphology have been epitaxailly grown on A-plane sapphire [α–Al_2O_3 $(11\bar{2}0)$]

substrates, where the lattice mismatch is as large as 7% between thin film and substrate, by DME growth mechanism.

3.3.3 Physical properties of fabricated thin films

The temperature dependence of magnetization (*M*-*T* curve) of thin film grown at $P_{O_2} = 1.5 \times 10^{-3}$ Pa and T_S = 925 ºC is shown in Fig. 3.5 (a). The measurements were performed under a field-cooled condition while an external magnetic field (*H*) of 8500 Oe was applied parallel to the film surface (*a*-axis). As a comparison, the result of thin film grown at $P_{O_2} = 1.0 \times 10^{-3}$ Pa and T_S = 700 ºC is also listed in the same figure. An increase in *M* depending on a decrease in *T* indicates that thin film possesses a ferrimagnetic ordering. The ferrimagnetic Curie temperature (T_C) of the thin film grown at $P_{O_2} = 1.5 \times 10^{-3}$ Pa and T_S = 925 ºC is estimated to be 211 K [from the broken line in Fig. 3.5 (a)], whereas the T_C of bulk specimen estimated from the composition of $0.87FeTiO_3 \cdot 0.13Fe_2O_3$ is; $55x + 950 (1 - x) = 171$ K [4]. The higher T_C than the bulk value may be ascribed to the excess amount of Fe^{2+} ions, which contribute to a net increase in *M* for the solid solution, caused by the reductive atmosphere during the thin film growth, as I described in Chapter 2. The T_C of thin film grown at $P_{O_2} = 1.0 \times 10^{-3}$ Pa and T_S = 700 ºC and corresponding bulk specimen are estimated to be 290 K and 234 K, respectively. The deviation of T_C between thin film and corresponding bulk specimen is; 290/234 = 123.9% in the case of thin film grown at $P_{O_2} = 1.0 \times 10^{-3}$ Pa and T_S = 700 ºC, and 211/171 = 123.3% in the thin film grown at $P_{O_2} = 1.5 \times 10^{-3}$ Pa and T_S = 925 ºC. The same magnitude of deviation in T_C for those two films indicates that the excess amount of Fe^{2+} is considered to be the same in both thin films, and the higher T_C (reductive atmosphere) is considered to balance the higher P_{O_2} (oxidative atmosphere) during the growth of thin film at $P_{O_2} = 1.5 \times 10^{-3}$ Pa and T_S = 925 ºC, compared with the deposition conditions of $P_{O_2} = 1.0 \times 10^{-3}$ Pa and T_S = 700 ºC. Therefore, the larger *M* (especially, bellow 100 K) of thin film grown at $P_{O_2} = 1.5 \times 10^{-3}$ Pa and T_S = 925 ºC than that of thin film grown at $P_{O_2} = 1.0 \times 10^{-3}$ Pa and T_S = 700 ºC is not due to the excess of Fe^{2+} but the improvement of crystallinity of thin film.

The external magnetic field dependence of magnetization (*M*-*H* curves) at 100 K [Fig. 3.5 (b)] also confirms the ferrimagnetic behavior of the ordered phases. The difference in the magnitude of coercive force between two thin films is also considered to be related to the

crystallinity of those films. Thin film grown at P_{O_2} = 1.0 × 10^{-3} Pa and T_S = 700 ºC is considered to have grains whose crystallographic orientations are tilted from *c*-axis of α–Al_2O_3. The easy axis of magnetization in $FeTiO_3$–Fe_2O_3 solid solution is considered to be within its C-plane. In this study, *H* was applied parallel to the film surface, which means that *H* was applied parallel to the easy axis of magnetization in $FeTiO_3$–Fe_2O_3 solid solution. In the case of thin film grown at P_{O_2} = 1.0 × 10^{-3} Pa and T_S = 700 ºC, the easy axis of magnetization of grains, which are tilted from *c*-axis of α–Al_2O_3, were not aligned parallel to the *H*, and the higher *H* is required for the magnetic moments of those tilted grains to be reversed; resulting in the increase of coercive force than in the case of thin film grown at P_{O_2} = 1.5 × 10^{-3} Pa and T_S = 925 ºC.

The temperature dependence of electric resistivity [$\rho(T)$] is shown in Fig. 3.6 for both thin films grown at P_{O_2} = 1.0 × 10^{-3} Pa and T_S = 700 ºC, and P_{O_2} = 1.5 × 10^{-3} Pa and T_S = 925 ºC. A linear relationship in the log ρ vs. 1000/*T* plot, which is almost the same as described in Chapter 2, indicates an Arrhenius type dependence of $\rho(T)$, as reported by Ishikawa [5] (see also Fig. 1.2.6). As I will introduce in Chapter 5, the electric conduction of $FeTiO_3$–Fe_2O_3 solid solution is considered to be due to the electron hopping between Fe^{2+} and Fe^{3+}. The same magnitudes of ρ in both two thin films indicates that the ratio between Fe^{2+} and Fe^{3+} are expected to be the same in both films, and this agrees well with the same magnitude of deviation in T_C for those two films. The Seebeck coefficients were +31.08 and +71.34 μVK^{-1} for the thin films of order phase grown at P_{O_2} = 1.0 × 10^{-3} Pa and T_S = 700 ºC, and P_{O_2} = 1.5 × 10^{-3} Pa and T_S = 925 ºC, respectively. The positive Seebeck coefficients indicate the *p*-type conduction as expected from the composition [5].

3.4 Conclusion

I have fabricated high-quality $FeTiO_3$–Fe_2O_3 solid solution thin films on α–Al_2O_3 (0001) substrates by extremely high growth temperature over 850 ºC. Although there is a large lattice mismatch (about 6.2%) between thin film and substrate in their C-planes, thin films with atomically flat step-and-terrace surface have been grown epitaxially by careful control of the deposition conditions. Those thin films are considered to be grown via one of the step-flow

growth called Domain-Matching Epitaxy where the integer multiple of lattice constants of thin film and substrate is matching across the interface and the lattice strain is relaxed in the initial stage of thin film growth. From the magnetic and electric properties measurements, fabricated thin films are considered to possess a high crystallinity and a suitable Fe^{2+}/Fe^{3+} ratio, which result in high magnetization and low electric resistivity. Current study reveals that fabricated thin films are expected to be applicable for spintronics devices not only in terms of crystallinity and surface morphology but also physical properties.

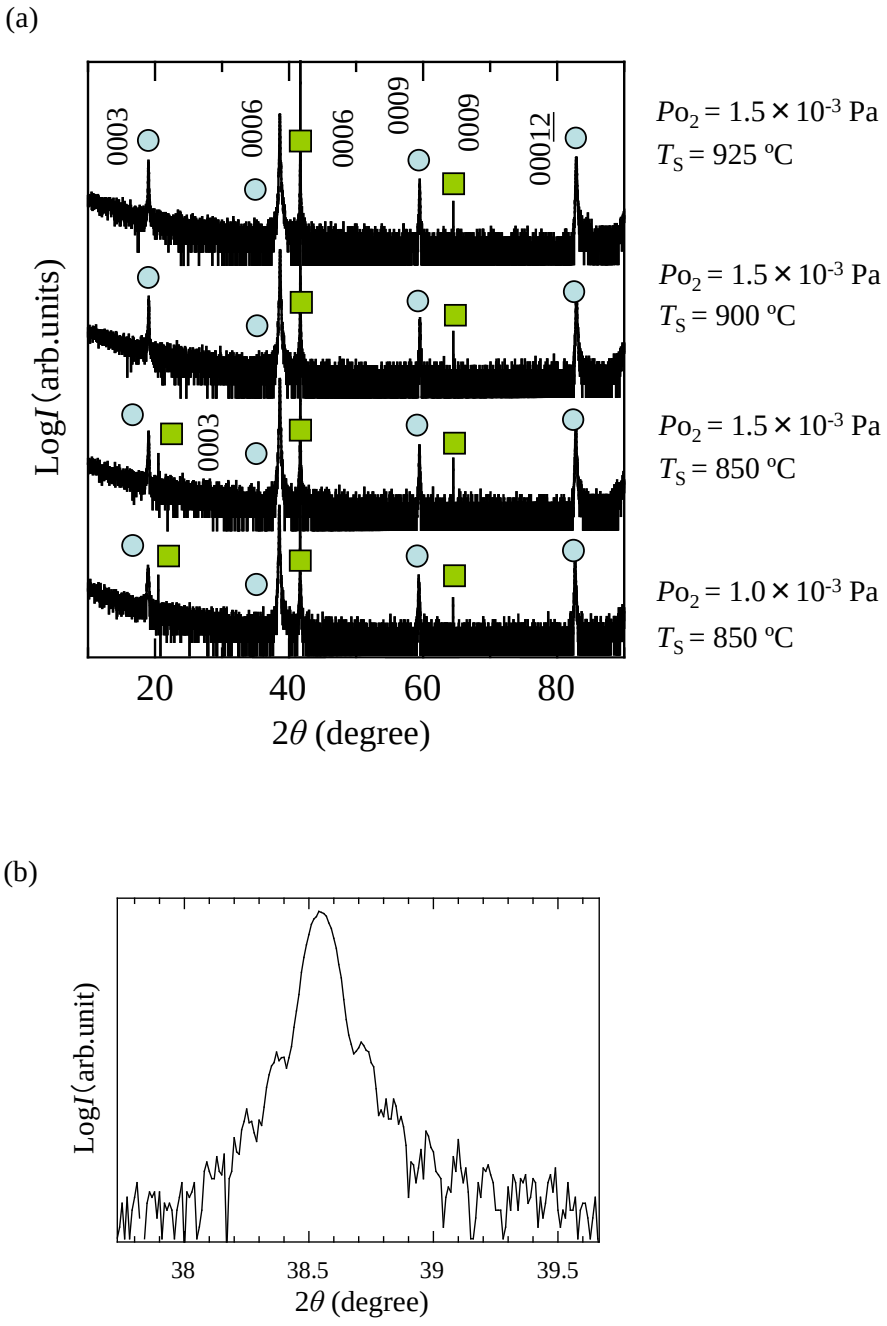

Fig. 3.1 (a) Out-of-plane XRD patterns for $FeTiO_3$–Fe_2O_3 solid solution thin films grown at various deposition conditions; ○: ordered-phase of solid solution, ■: α–Al_2O_3.
(b) Magnified image of 0006 peak for thin film grown at P_{O_2} = 1.5 × 10^{-3} Pa and T_S = 925 °C.

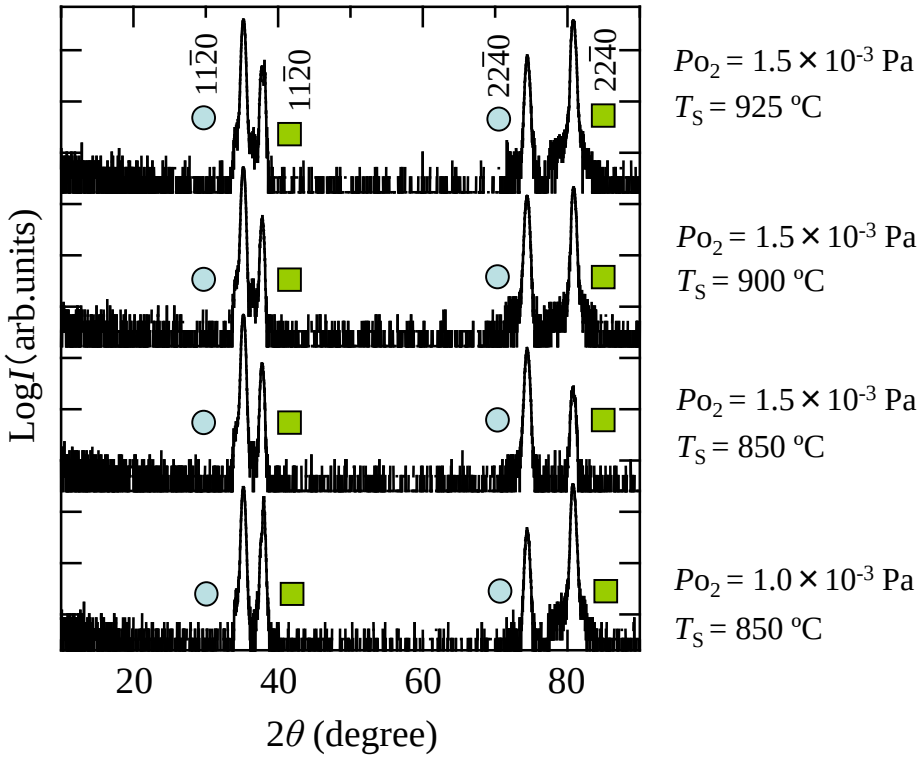

Fig. 3.2 In-plane XRD patterns for $FeTiO_3$–Fe_2O_3 solid solution thin films grown at various deposition conditions; ○: ordered-phased solid solution, □: α–Al_2O_3.

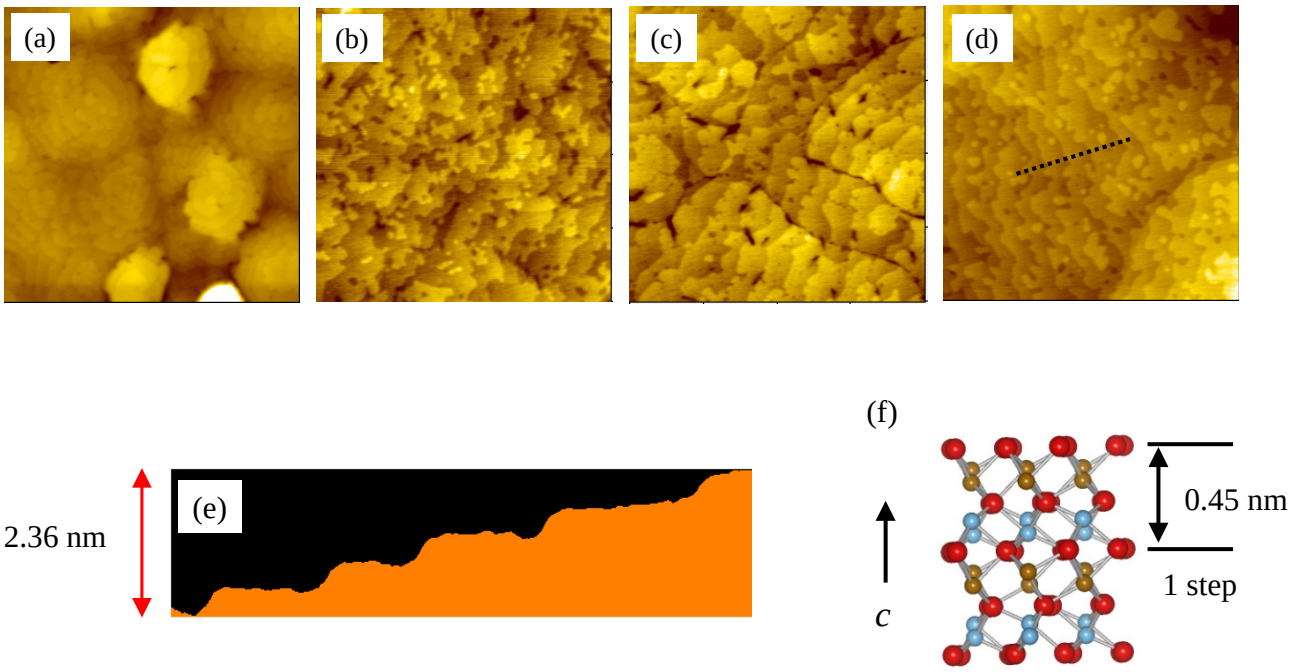

Fig. 3.3 AFM images for the solid solution thin films grown at (a) Po_2 = 1.0 × 10^{-3} Pa and T_S = 850 ºC, (b) Po_2 = 1.5 × 10^{-3} Pa and T_S = 850 ºC, (c) Po_2 = 1.5 × 10^{-3} Pa and T_S = 900 ºC, and (d) Po_2 = 1.5 × 10^{-3} Pa and T_S = 925 ºC. (e) Cross-section view along the broken line in Fig. 3.3 (d). (f) Schematic image of one charge-neutral unit of $FeTiO_3$ (indicated by a double-headed arrow) depicted by VESTA software [11].

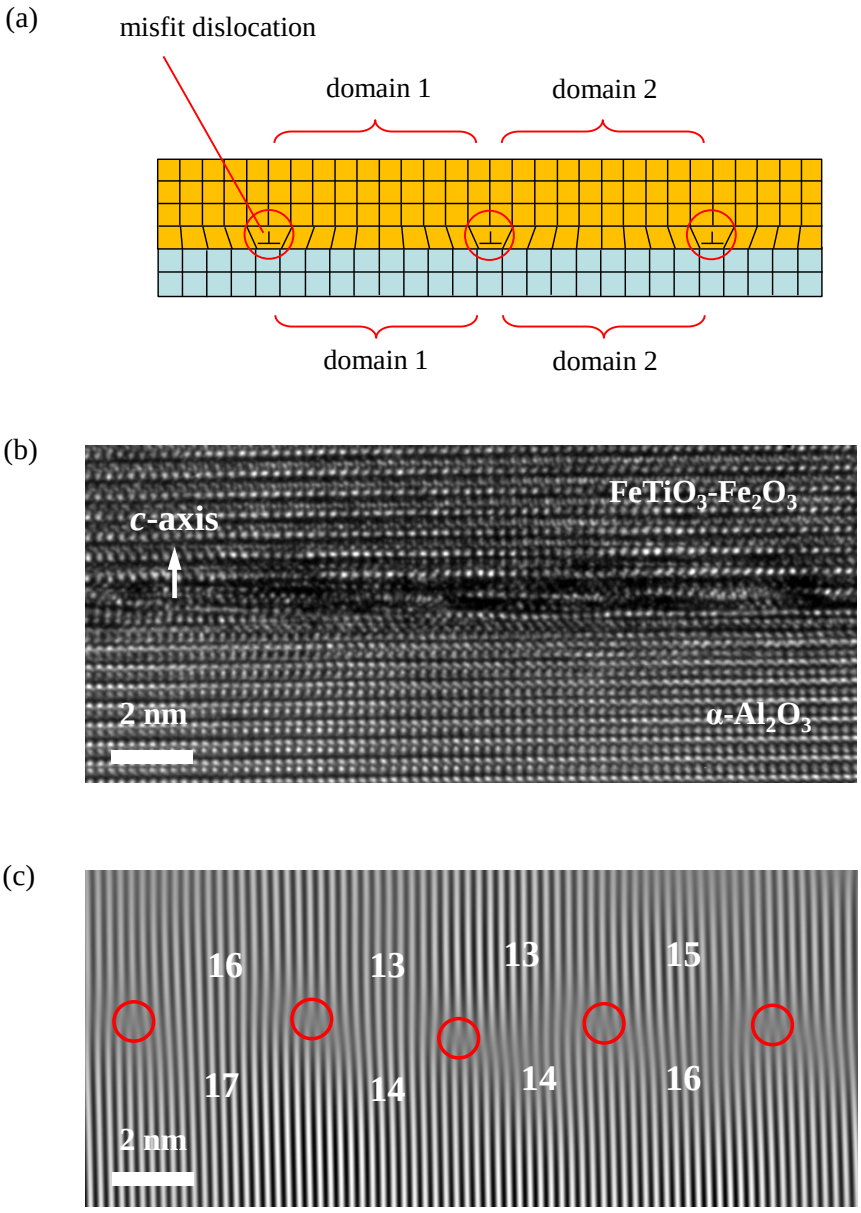

Fig. 3.4 (a) Schematic image of the lattice-strain relaxation mechanism in domain-matching epitaxy. (b) Cross-sectional HR-TEM image of the interface between $FeTiO_3$–Fe_2O_3 solid solution thin film and α–Al_2O_3 substrate. (c) Fourier-filtered TEM image corresponding to the HR-TEM image of Fig. 3.4 (b). Misfit dislocation is indicated by the red open circles.

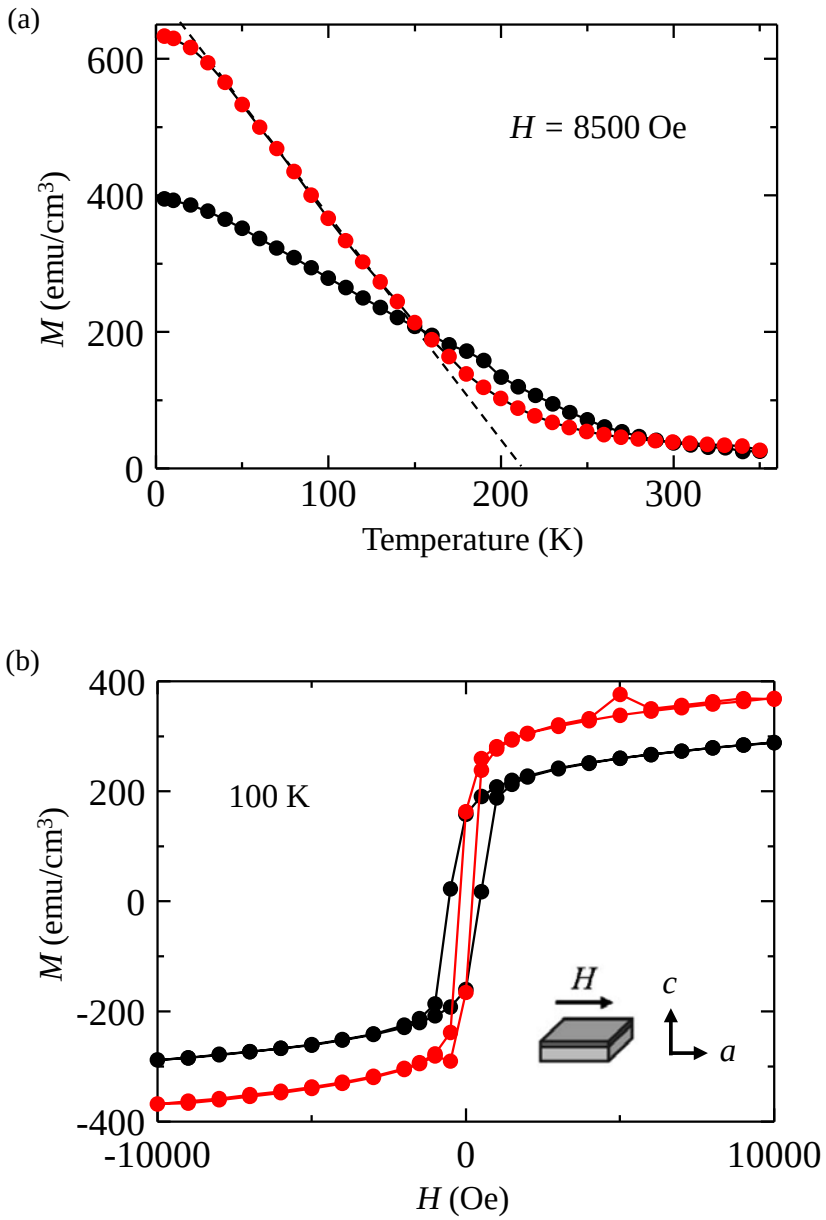

Fig. 3.5 (a) M-T curves for the thin films grown at P_{O_2} = 1.5 × 10^{-3} Pa and T_S = 925 ºC (red closed circle), and P_{O_2} = 1.0 × 10^{-3} Pa and T_S = 700 ºC (black closed circle). The external magnetic field of 8500 Oe was applied parallel to the film surface. (b) M-H curves at 100 K for the thin films grown at P_{O_2} = 1.5 × 10^{-3} Pa and T_S = 925 ºC (red closed circle), and P_{O_2} = 1.0 × 10^{-3} Pa and T_S = 700 ºC (black closed circle).

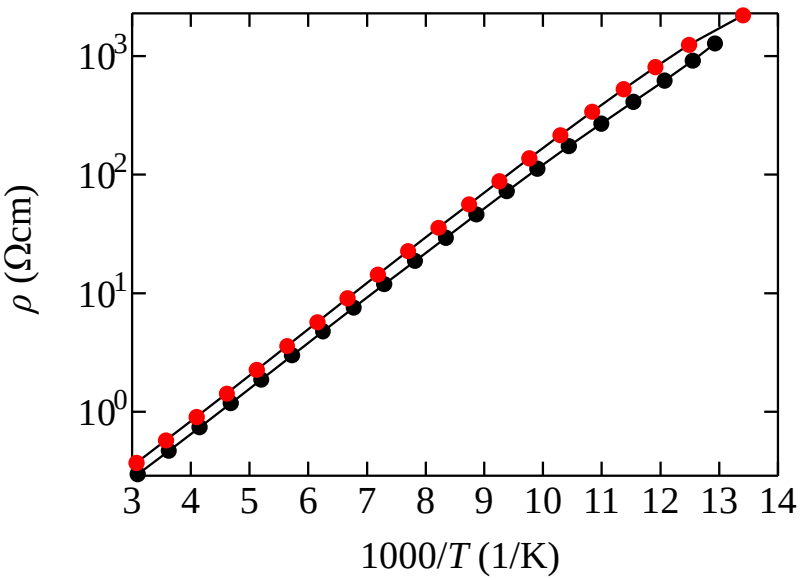

Fig. 3.6 Reciprocal T-dependence of ρ for the thin films grown at $P\mathrm{o}_2 = 1.5 \times 10^{-3}$ Pa and $T_S = 925$ ºC (red closed circle), and $P\mathrm{o}_2 = 1.0 \times 10^{-3}$ Pa and $T_S = 700$ ºC (black closed circle).

3.5 References

1. T. Oshima, N. Arai, N. Suzuki, S. Ohira, and S. Fujita, *Thin Solid Films* **516**, 5768 (2008).
2. J. Narayan, and B. C. Larson, *J. Appl. Phys.* **93**, 278 (2003).
3. N.E. Brown, A. Navrotsky, G. L. Nord, and S. K. Banerjee, *Am. Miner.* **78**, 941 (1993).
4. Y. Ishikawa, *J. Phys. Soc. Jpn.* **12**, 1083 (1957).
5. Y. Ishikawa, *J. Phys. Soc. Jpn.* **13**, 37 (1958).
6. http://home.rzg.mpg.de/~mam/index.html
7. H. Hojo, K. Fujita, K. Tanaka, and K. Hirao, *Appl. Phys. Lett.* **89**, 082509 (2006).
8. H. Hojo, K. Fujita, K. Tanaka, and K. Hirao, *Appl. Phys. Lett.* **89**, 142503 (2006).
9. H. Hojo, K. Fujita, K. Tanaka, and K. Hirao, *J. Magn. Magn. Mater.* **310**, 2105 (2007).
10. K. Tanaka, K. Fujita, S. Nakashima, H. Hojo, and T. Matoba, *J. Magn. Magn. Mater.* **321**, 818 (2009).
11. http://www.geocities.jp/kmo_mma/crystal/en/vesta.html
12. J. W. Mathews, and A. E. Blakeslee, *J. Cryst. Growth* **27**, 188 (1974).
13. J. Narayan, P. Tiwari, X. Chen, R. Chowdhury, and T. Zheleva, *Appl. Phys. Lett.* **61**, 1290 (1992).
14. J. Narayan, A. K. Sharma, A. Kvit, C. Jin, J.F. Muth, and O. W. Holland, *Solid State Commun.* **121**, 9 (2002).

Chapter 4. Single crystalline ilmenite-hematite solid solution thin films with atomically smooth surface grown on A-plane sapphire substrates

4.1 lntroduction

In Chapter 3, $FeTiO_3$–Fe_2O_3 solid solution thin films with atomically flat surface were grown on C-plane sapphire [α–Al_2O_3 (0001)] substrates via Domain-Matching Epitaxy (DME) and it is indicated that the careful control of growth condition is a key point in order to obtain high-quality thin films for spintronics application. In this Chapter 4, I introduce the epitaxial growth of high-quality $FeTiO_3$–Fe_2O_3 solid solution thin films on A-plane sapphire [α–Al_2O_3 (11 $\bar{2}$0)] substrates via DME.

As I already introduced in Section 1.2.1 and will discuss in Chapter 5, the mechanism of electric conduction in ordered-phase of $FeTiO_3$–Fe_2O_3 solid solution is considered to be caused by the electron transfer between Fe^{2+} and Fe^{3+} cations in cation layers where only Fe cations exist. Therefore, the electric conduction in $FeTiO_3$–Fe_2O_3 solid solution is also considered to occur easily along the in-plane direction of its C-plane. The schematic illustrations of the electric conduction mechanism of $FeTiO_3$–Fe_2O_3 solid solution thin films on both α–Al_2O_3 (0001) and (11$\bar{2}$0) substrates are shown in Fig. 4.1, where the electric conductive direction is indicated by a red double-headed arrow, and one can see that the electric current direction can be varied from in-plane direction of substrate [current-in-plane (CIP)] to its out-of-plane direction [current-perpendicular-to-plane (CPP)] by changing the growth plane of substrate. The control of electric current direction is also the key technology for spintronics device application. Whereas some spintronics devices such as spin-polarized field-effect transistor require the CIP-type conduction [1], other devices including magnetic tunneling junctions (MTJs) require CPP-type conduction [2]. Therefore, whereas $FeTiO_3$–Fe_2O_3 thin films grown on α–Al_2O_3 (0001) substrates are expected to be more useful for CIP-type device application, $FeTiO_3$–Fe_2O_3 thin films are required to be fabricated on α–Al_2O_3 (11$\bar{2}$0) substrates in order to

be applied for CPP-type spintronics devices.

However, the lattice mismatch between $FeTiO_3$–Fe_2O_3 solid solution and α–Al_2O_3 in their A-plane is as large as 7.0% which is larger than that of C-plane (6.2%) (see also Table 2.1). Although this large lattice mismatch usually prevents $FeTiO_3$–Fe_2O_3 thin films from being grown epitaxially on α–Al_2O_3 (11$\bar{2}$0) substrates as I will briefly introduce in Section 4.3.1, I have fabricated high-quality $FeTiO_3$–Fe_2O_3 thin films with step-and-terrace surface structure on α–Al_2O_3 (11$\bar{2}$0) substrates by carefully controlling the growth conditions. I stress that I have successfully achieved and confirmed the epitaxial growth of $FeTiO_3$–Fe_2O_3 thin films on α–Al_2O_3 (11$\bar{2}$0) substrates for the first time. Although Takada *et al.* also have reported the epitaxial growth of $FeTiO_3$–Fe_2O_3 thin films on α–Al_2O_3 (11$\bar{2}$0) substrates [3], the formation of ordered-phase and the epitaxial relationship between thin film and substrate have not been clarified. I have confirmed them by conducting in-plane X-ray diffraction (XRD) measurement (see Fig. 4.4).

4.2 Experimental procedure

4.2.1 Sample preparation

Thin films were fabricated by PLD method. The preparation condition of PLD targets with $0.8FeTiO_3 \cdot 0.2Fe_2O_3$ composition was also the same as described in Chapter 2. In order to prepare a substrate with atomically flat surface, α–Al_2O_3 (11$\bar{2}$0) substrates (Shinkosha Co. Ltd.) are thermally annealed in air at 1150 ºC for 3h before being loaded on the PLD vacuum chamber. KrF excimer laser (λ = 248 nm, ~2.5 J/cm^2) was focused on the targets at the repetition of 2 Hz. The oxygen partial pressure (P_{O_2}) and substrate temperature (T_S) were varied from 1.0×10^{-3} to 3.0×10^{-3} Pa and from 700 to 900 ºC, respectively.

4.2.2 Sample characterization

The characterizations of fabricated thin films were also the same as described in Chapter 2. The film thickness was evaluated to be about 75 nm using a surface profiler. The composition of thin films determined by Rutherford backscattering measurement (RBS) followed by the fitting simulation using SIMNRA 5.02 software program [4], and it was revealed that thin films

fabricated from $0.8FeTiO_3 \cdot 0.2Fe_2O_3$ composition target included $0.87FeTiO_3 \cdot 0.13Fe_2O_3$ composition. The crystal structure of thin films was analyzed by both out-of-plane (for A-plane of thin films) and in-plane (for C-plane) XRD measurements with Cu Kα radiation (ATX-G, Rigaku) in order to determine the epitaxial relationship between thin films and substrates (In order to avoid confusion, I note that C- and A-planes of fabricated thin films in this chapter are replaced each other compared to those of thin films in Chapter 2 and 3). The surface morphology of thin films was observed using an atomic force microscope (AFM) (SII Nano Technology, SPI3800N). The crystal structure at the interface between thin film and substrate was observed by cross-sectional high-resolution transmission electron microscope (HR-TEM) (JEM-2100F, JEOL). The measurements of magnetization were carried out using a superconducting quantum interference device (SQUID) magnetometer (MPMS, Quantum Design). The electric resistivity was measured by the van der Pauw method (Resitest8300, Toyo).

4.3 Results and Discussion

4.3.1 Crystalline and surface analyses of thin films grown at T_S < 850 ºC

First, the results of $FeTiO_3$–Fe_2O_3 thin films grown at T_S < 850 ºC are shown briefly in this section.

Fig. 4.2 (a) shows the out-of-plane (A-plane) XRD patterns of thin film grown at $Po_2 = 1.0 \times 10^{-3}$ Pa and T_S = 700 ºC and indicates that the *a*-axis oriented thin film without any impurities is obtained. In-plane (C-plane) XRD patterns of the same thin film is shown in Fig. 4.2 (b). 000*3n* (*n* = 1–4) peaks, which were related to the C-plane of solid solution, were observed along with the *c*-axis of α–Al_2O_3, and the appearance of 0003 and 0009 peaks indicates that the fabricated thin film has ordered-phase of $FeTiO_3$–Fe_2O_3 solid solution. However, two excess peaks were also observed at 35 and 74º in Fig. 4.2 (b). By comparing Fig. 4.2 (a) and (b), the positions of these two peaks are coincident with those of the peaks from $11\bar{2}0$ and $22\bar{4}0$ in Fig. 4.2 (a) as indicated by red broken lines. Therefore, the in-plane orientation of crystallographic axis of thin film is not fully locked by substrate, and fabricated thin film is not epitaxial one but textured one. The appearance of $11\bar{2}0$ and $22\bar{4}0$ peaks in the in-plane XRD pattern indicated

that some part of *c*-axis oriented thin film was grown along *a*-axis of substrate as illustrated in Fig. 4.2 (c). It is known that the surface energy of α–Al_2O_3 ($11\bar{2}0$) plane is higher (less stable) than that of α–Al_2O_3 (0001) plane [5, 6], and the surface energy relationship in $FeTiO_3$–Fe_2O_3 solid solution system is also considered to be the same as α–Al_2O_3 because of the crystallographic similarity between them. Therefore, the preferential growth of *c*-axis oriented $FeTiO_3$–Fe_2O_3 thin film is considered to be reasonable in terms of surface energy, and this incoherence in thin film growth orientation indicates that thin films were not grown in a step-flow (two-dimensional) mode but in a three-dimensional mode. Fig. 4.2 (d) is the AFM image of the same thin film and one can see that the surface is apparently rough. Although I have varied the deposition condition, especially T_S widely from 500 ºC to 800 ºC, the epitaxial thin films have not been fabricated.

The main reason of this difficulty in preparing epitaxial $FeTiO_3$–Fe_2O_3 thin film on α–Al_2O_3 ($11\bar{2}0$) substrates is a quite large lattice mismatch between thin film and substrate (7%). It is known that epitaxial growth becomes to be difficult when the lattice mismatch between thin film and substrate exceed around 7–8% [7].

However, as I introduced in Chapter 3, many thin film and substrate systems including ZnO/α–Al_2O_3 (0001) (the lattice mismatch is 17%.) [8, 9] are epitaxially grown via DME growth, and the present $FeTiO_3$–Fe_2O_3 thin films with atomically flat surface morphology also have been grown on α–Al_2O_3 (0001) substrates though DME by careful control of growth conditions. I have considered that T_S is the most crucial factor in order to change the growth mode from three-dimensional to two-dimensional (step-flow), and fabricated thin films with T_S > 850 ºC.

4.3.2 Crystalline and surface analyses of thin films grown at T_S > 850 ºC

Fig. 4.3 shows out-of-plane XRD patterns of thin films grown at T_S > 850 ºC. Whereas no impurities were detected in thin films grown at T_S = 850 ºC, few amount of impurities were observed in thin films grown at T_S = 900 ºC. I cannot identify these impurities but consider that they are due to the less stable surface of $FeTiO_3$–Fe_2O_3 ($11\bar{2}0$) plane. As I noted in Section 4.3.1, $FeTiO_3$–Fe_2O_3 ($11\bar{2}0$) plane surface is considered to be unstable compared to other planes including (0001) or ($1\bar{1}02$) (R-plane), and it is energetically favorable for other crystallographic plane or crystal phase to be exposed as a thin film surface at too high T_S such as

900 ºC. On the other hand, $FeTiO_3$–Fe_2O_3 (0001) plane, which is considered to be the most stable crystallographic plane in $FeTiO_3$–Fe_2O_3, is still stable under even T_S > 900 ºC, and higher T_S is more suitable for thin films to grow by step-flow mode. Indeed, $FeTiO_3$–Fe_2O_3 thin films with the most atomically flat surface have been fabricated on α–Al_2O_3 (0001) substrates at Po_2 = 1.5×10^{-3} Pa and T_S = 925 ºC, as I introduced in Chapter 3.

In-plane XRD patterns of the same thin films in Fig. 4.3 are shown in Fig. 4.4. As opposed to the thin films grown at T_S < 850 ºC, no peaks derived from A-plane of $FeTiO_3$–Fe_2O_3 ($11\bar{2}0$ and $22\bar{4}0$) were observed at all deposition conditions described in Fig. 4.4. Therefore, $FeTiO_3$–Fe_2O_3 thin films have been epitaxially grown on α–Al_2O_3 ($11\bar{2}0$) substrates when T_S > 850 ºC. From these out-of-plane and in-plane XRD patterns, I can safely say that thin films with single phase of ordered phase were epitaxially grown on α–Al_2O_3 ($11\bar{2}0$) substrates with the deposition conditions of 1.0×10^{-3} Pa < Po_2 < 3.0×10^{-3} Pa and T_S = 850 ºC.

Fig. 4.5 shows the AFM images of the surface structure for the same thin films in Fig. 4.3 and 4.4. Although previous out-of-plane and in-plane XRD patterns indicate that epitaxial thin films with single phase of ordered-phase were grown on α–Al_2O_3 ($11\bar{2}0$) substrates at 1.0×10^{-3} Pa < Po_2 < 3.0×10^{-3} Pa and T_S = 850 ºC, their surface structure were quite different to each other. Whereas the step-and-terrace surface structure was observed in thin films grown at T_S = 850 ºC, the same surface structure almost disappeared in thin films grown at T_S = 900 ºC. This tendency is also considered to be due to the less stable surface energy for $FeTiO_3$–Fe_2O_3 ($11\bar{2}0$) plane and agrees the out-of-plane XRD results in Fig. 4.3. With carefully controlling Po_2 and T_S, thin films with the clearest step-and-terrace surface structure could be prepared at Po_2 = 2.0×10^{-3} Pa and T_S = 850 ºC. One step height of this thin film is estimated to be 0.3 nm from Fig. 4.5 (h), and this height is consistent with the planar distance of ($11\bar{2}0$) plane (0.25 nm), which means surface of this thin film is atomically flat.

4.3.3 Cross-sectional HR-TEM observation at the interface and DME mechanism

From Section 4.3.1 and 4.3.2, $FeTiO_3$–Fe_2O_3 thin films with atomically flat surface were epitaxially grown on α–Al_2O_3 ($11\bar{2}0$) substrates when films are grown at 1.0×10^{-3} Pa < Po_2 < 3.0×10^{-3} Pa and T_S = 850 ºC, although there is a quite large lattice mismatch of 7% between thin film and substrate. I consider that those thin films also have been grown by the same

DME as in the case of thin films on α–Al_2O_3 (0001) substrates. In order to investigate the DME mechanism in $FeTiO_3$–Fe_2O_3/α–Al_2O_3 ($11\bar{2}0$) system, I carried out cross-sectional HR-TEM observation at the interface between thin film and substrate. Fig. 4.6 (a) shows the cross-sectional HR-TEM image of the interface between $FeTiO_3$–Fe_2O_3 thin film and α–Al_2O_3 ($11\bar{2}0$) substrate. The electron beam was irradiated along *c*-axis of substrate, and the displayed image of Fig. 4.6 (a) corresponds to the C-plane of thin film and substrate. White balls correspond to O^{2-} anions and one can see the distorted hexagonal close packed aligned structure of them (see also Section 1.2.1 for the better understanding of the crystal structure of $FeTiO_3$–Fe_2O_3). As opposed to the HR-TEM image of thin film grown on α–Al_2O_3 (0001) in Fig. 3.3 (b), clear dislocation cores which are indicated by red open circles were observed along the interface, and the interval between two of them is estimated to be around 4.5 nm. Fig. 4.6 (b) is the schematic illustration for C-plane of α–Al_2O_3 and $FeTiO_3$–Fe_2O_3 depicted with VESTA software [10]. Although C-plane of them consists of the distorted hexagonal close packed structure of O^{2-} anions, they are also aligned as regular hexagons indicated by the black broken lines, and the edge length corresponds to the *a*-axis lattice constant of them (4.760 Å for α–Al_2O_3 and 5.078 Å for $FeTiO_3$–Fe_2O_3). Therefore, the average distance between two O^{2-} anions along the blue broken line in Fig. 4.6 (b) is calculated as;

$$\alpha\text{–}Al_2O_3;\ (4.760 \times \sqrt{3})/3 = 2.748\ \text{Å}$$
$$FeTiO_3\text{–}Fe_2O_3;\ (5.078 \times \sqrt{3})/3 = 2.931\ \text{Å}$$

Fig. 4.6 (c) is the magnified image around two adjacent dislocation cores in Fig. 4.6 (a), and there are about 15 O^{2-} anions between them (the distance is around 4.5 nm). This is because the every 15 units of O^{2-} anions aligned along the interface in $FeTiO_3$–Fe_2O_3 ($2.931 \times 15 = 43.976$ Å) is well coincident to the every 16 units of them in α–Al_2O_3 ($2.748 \times 16 = 43.968$ Å). The margin between the lattice constants of these two units is as small as 0.008 Å, and I consider that this accordance leads to the DME growth in the present $FeTiO_3$–Fe_2O_3/α–Al_2O_3 ($11\bar{2}0$) system.

4.3.3 Physical properties of thin films grown at T_S > 850 ºC

The temperature dependence of magnetization (*M*-*T* curve) of thin film grown at P_{O_2} = 2.0 × 10^{-3} Pa and T_S = 850 ºC is shown in Fig. 4.7 (a). An external magnetic field (*H*) of 8500 Oe was applied parallel to the film surface (*c*-axis). Although an increase in *M* depending on a decrease in *T* indicates that thin film possesses a ferrimagnetic ordering, a linear *M*-*T* relationship below T_C as seen for thin films grown on α–Al_2O_3 (0001) substrates were not observed. This is because *c*-axis direction of $FeTiO_3$–Fe_2O_3 corresponds to the hard axis for magnetization, and it is hard for each magnetic moment in Fe^{2+} cation to be aligned in the ferrimagnetic arrangement along the *H* direction [11]. The external magnetic field dependence of magnetization (*M*-*H* curves) at 100 K [Fig. 4.7 (b)] also confirms the ferrimagnetic behavior of the ordered phases. *M* was not saturated even under the *H* of 10,000 Oe and larger coercive force of 2,000 Oe was observed compared to thin film grown on α–Al_2O_3 (0001) substrate under P_{O_2} = 1.5 × 10^{-3} Pa and T_S = 925 ºC. These behaviors also reflect the crystal anisotropy of magnetization in $FeTiO_3$–Fe_2O_3 solid solution.

The temperature dependence of electric resistivity [$\rho(T)$] is shown in Fig. 4.8 for thin film grown at P_{O_2} = 2.0 × 10^{-3} Pa and T_S = 850 ºC. For comparison, the result for thin film grown on α–Al_2O_3 (0001) substrate (the growth condition; P_{O_2} = 1.0 × 10^{-3} Pa and T_S = 700 ºC) is also shown in the same figure. The electric resistivity of thin film on α–Al_2O_3 ($11\bar{2}0$) substrate is higher than that of thin film on α–Al_2O_3 (0001) substrate by one digit in magnitude. This reflects the crystal anisotropy of electric conductivity in $FeTiO_3$–Fe_2O_3 solid solution as I discussed in Section 4.1 and will further discuss in Chapter 5. The schematic images for the electric conductivity measurement (van der Pauw method) are illustrated on both left [for thin film grown on α–Al_2O_3 ($11\bar{2}0$) substrate] and right side [for thin film grown on α–Al_2O_3 (0001) substrate] of Fig. 4.8. The electric conductivity is considered to occur easily along the C-plane direction than *c*-axis direction in $FeTiO_3$–Fe_2O_3 solid solution. Whereas I can measure $\rho(T)$ derived from the electric current along C-plane of $FeTiO_3$–Fe_2O_3 for thin film grown on α–Al_2O_3 (0001) substrate, I measure $\rho(T)$ derived from the electric current both along C-plane and *c*-axis of $FeTiO_3$–Fe_2O_3 for thin film grown on α–Al_2O_3 ($11\bar{2}0$) substrate. As opposed to Arrhenius type dependence of $\rho(T)$ for thin film grown on α–Al_2O_3 (0001) substrate, the gradient in the log ρ vs. 1000/*T* plot, therefore, the activation energy is gradually changing around 140 K (1000/*T* = 7.14) in the case of thin film grown on α–Al_2O_3 ($11\bar{2}0$) substrate. The

same behavior is observed in the $\rho(T)$ measurement for sintered $FeTiO_3$–Fe_2O_3 bulk specimen reported by Ishikawa [12], and the magnitude of ρ in his report is also the same as the result for thin film grown on α–Al_2O_3 (11$\bar{2}$0) substrate. Therefore, the electric properties of the thin film sample are similar to those of the bulk specimen and reflect the anisotropy in electric conduction of $FeTiO_3$–Fe_2O_3 solid solution.

Although it is difficult to investigate physical properties of thin films grown on α–Al_2O_3 (11$\bar{2}$0) substrates because the easy axis for both magnetization and electric conductivity is perpendicular to the substrate surface, the physical property measurement indicated that the thin films exhibited ferrimagnetism and electric resistivity similarly to sintered bulk specimen. From these results, I have also confirmed the formation of ordered-phase of $FeTiO_3$–Fe_2O_3 solid solution as indicated by in-plane XRD measurements in Fig. 4.4.

4.4 Conclusion

I have fabricated high-quality $FeTiO_3$–Fe_2O_3 epitaxial thin films on α–Al_2O_3 (11$\bar{2}$0) substrates by careful control of the deposition conditions. Although there is a large lattice mismatch around 7.0% between thin film and substrate in their A-planes, thin films with atomically flat step-and-terrace surface have been epitaxially grown at $P_{O_2} = 2.0 \times 10^{-3}$ Pa and T_S = 850 ºC. I have confirmed the epitaxial growth and formation of ordered-phase of $FeTiO_3$–Fe_2O_3 thin films on α–Al_2O_3 (11$\bar{2}$0) substrates for the first time by carrying out in-plane XRD analysis. I consider that those thin films are also grown via two-dimensional DME mechanism which is suggested by cross-sectional HR-TEM observation. The magnetic properties measurements revealed that fabricated thin film exhibited ferrimagnetism, also indicating the formation of order-phase. The electric resistivity measurement showed that fabricated thin film also possessed the transport property similar to that of the sintered bulk specimen.

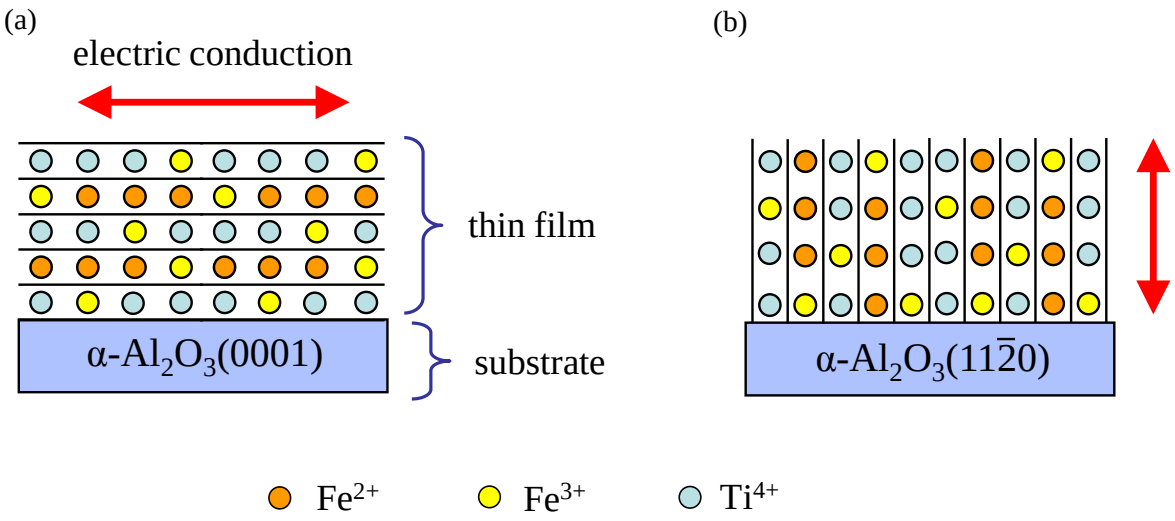

Fig. 4.1 Schematic images of $FeTiO_3$–Fe_2O_3 solid solution thin films grown on (a) α–Al_2O_3 (0001) (C-plane) substrates, and (b) α–Al_2O_3 (11$\bar{2}$0) (A-plane) ones. Red double-headed arrows indicate the direction of electric conduction in $FeTiO_3$–Fe_2O_3 solid solution.

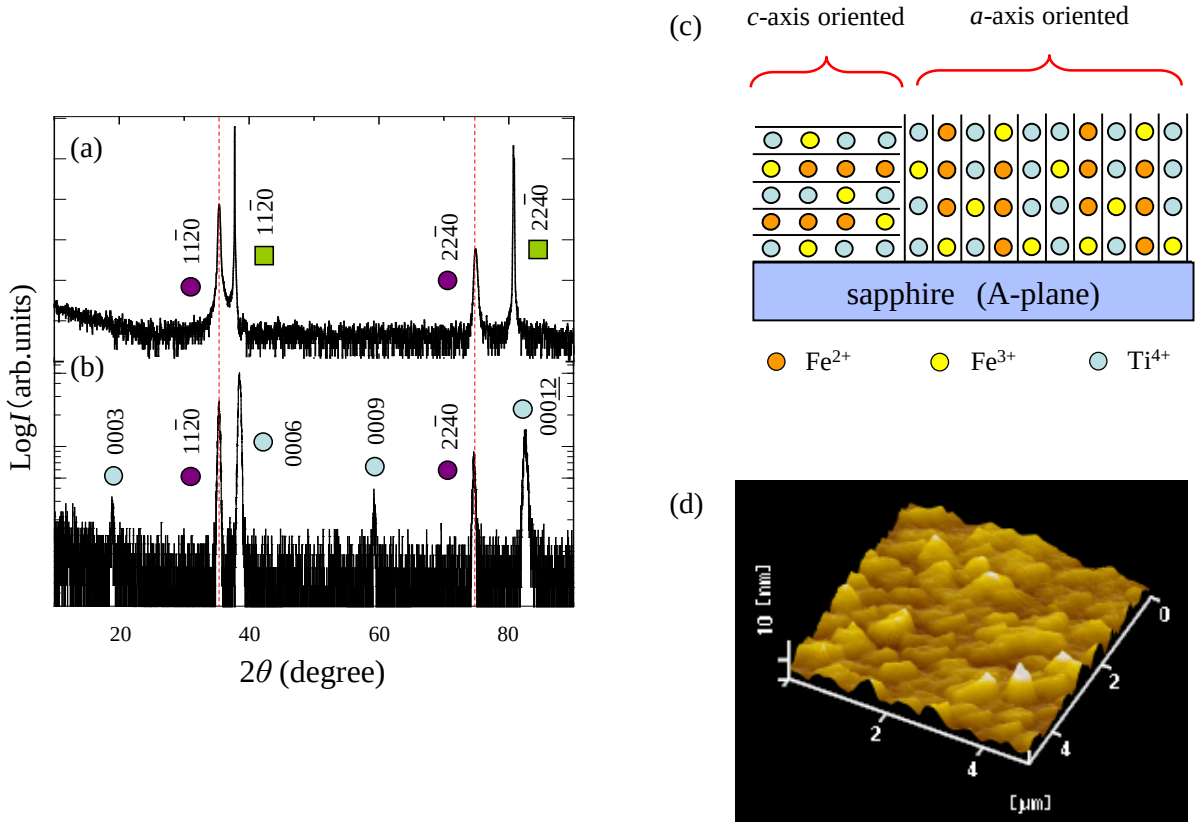

Fig. 4.2 (a) Out-of-plane (A-plane), and (b) in-plane (C-plane) XRD patterns of thin film grown under Po_2 = 1.0 × 10^{-3} Pa and T_S = 700 ºC; ■ : α–Al_2O_3 substrate, ● : C-plane of $FeTiO_3$–Fe_2O_3, ● : A-plane of $FeTiO_3$–Fe_2O_3. Red broken lines indicate the peak position of the diffraction from $11\bar{2}0$ and $22\bar{4}0$. (c) Schematic image of *a*- and *c*-axis oriented $FeTiO_3$–Fe_2O_3 solid solution thin film grown along *a*-axis of α–Al_2O_3 substrate. (d) AFM image of the surface of $FeTiO_3$–Fe_2O_3 thin film. The observed region is 5 × 5 μm.

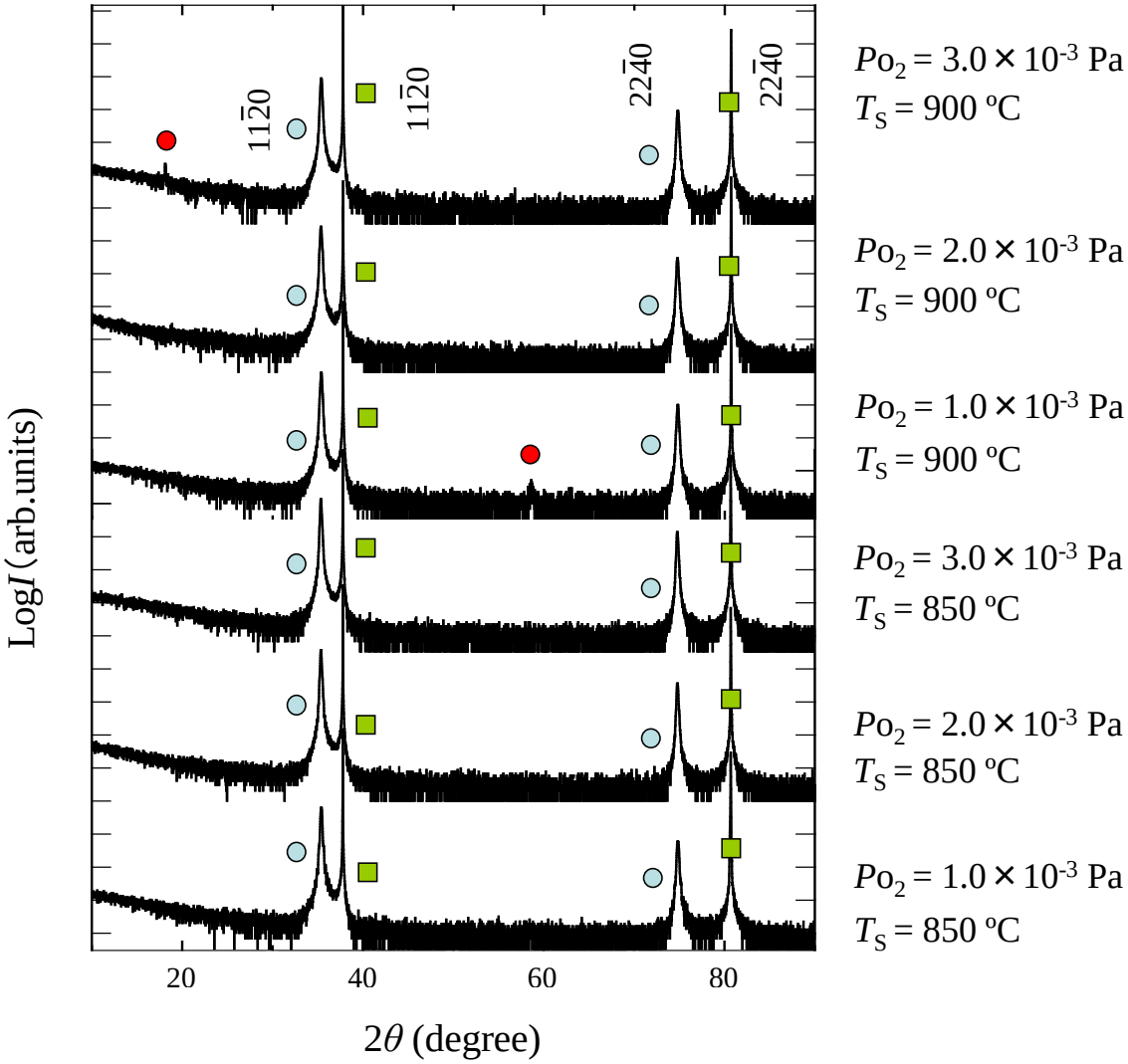

Fig. 4.3 Out-of-plane (A-plane) XRD patterns of $FeTiO_3$–Fe_2O_3 thin films grown on α–Al_2O_3 ($11\bar{2}0$) substrates; ■ : α–Al_2O_3 substrate, ○ : $FeTiO_3$–Fe_2O_3, ● : impurities.

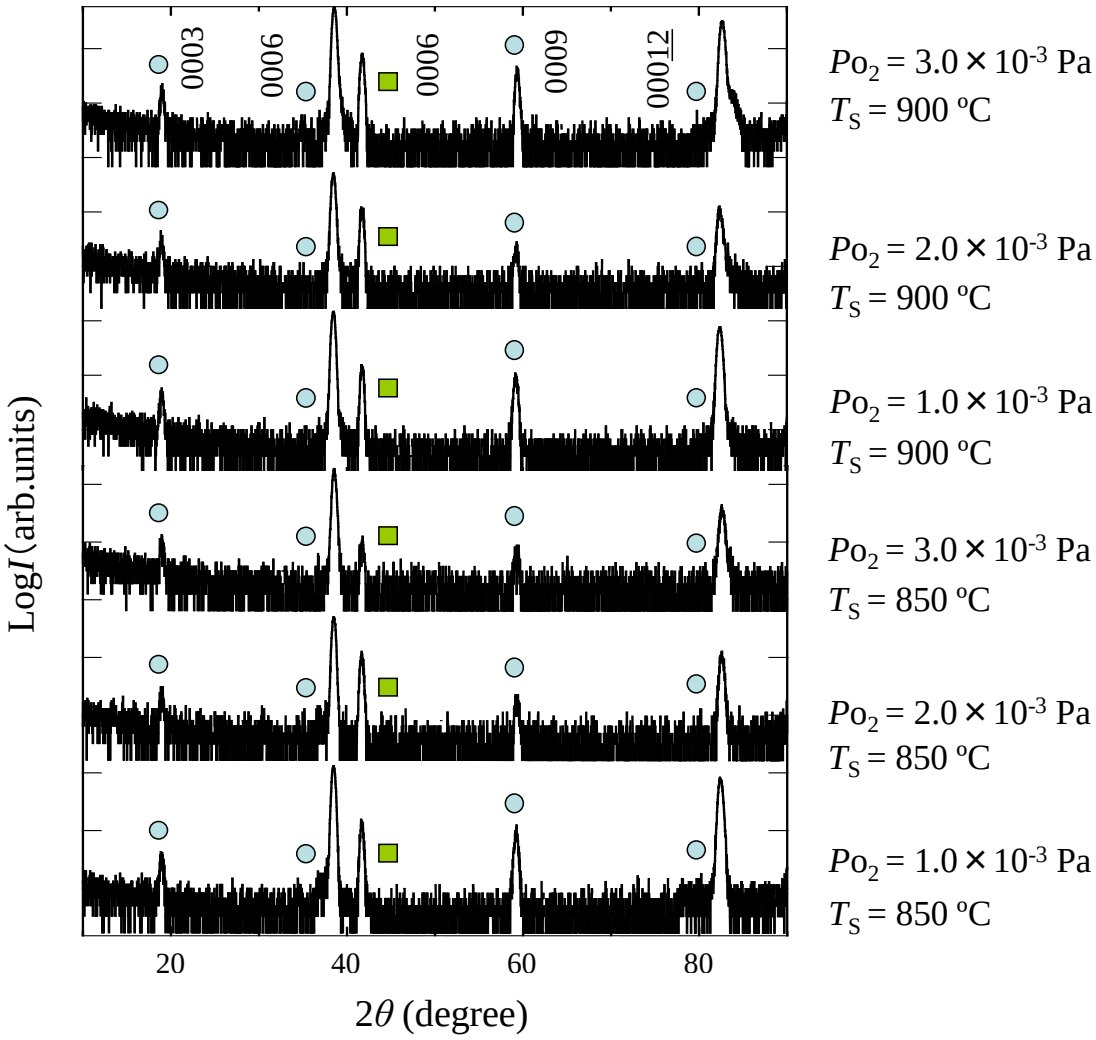

Fig. 4.4 In-plane (C-plane) XRD patterns of $FeTiO_3$–Fe_2O_3 thin films grown on α–Al_2O_3 (11 $\bar{2}$0) substrates; ■ : α–Al_2O_3 substrate, ○ : $FeTiO_3$–Fe_2O_3.

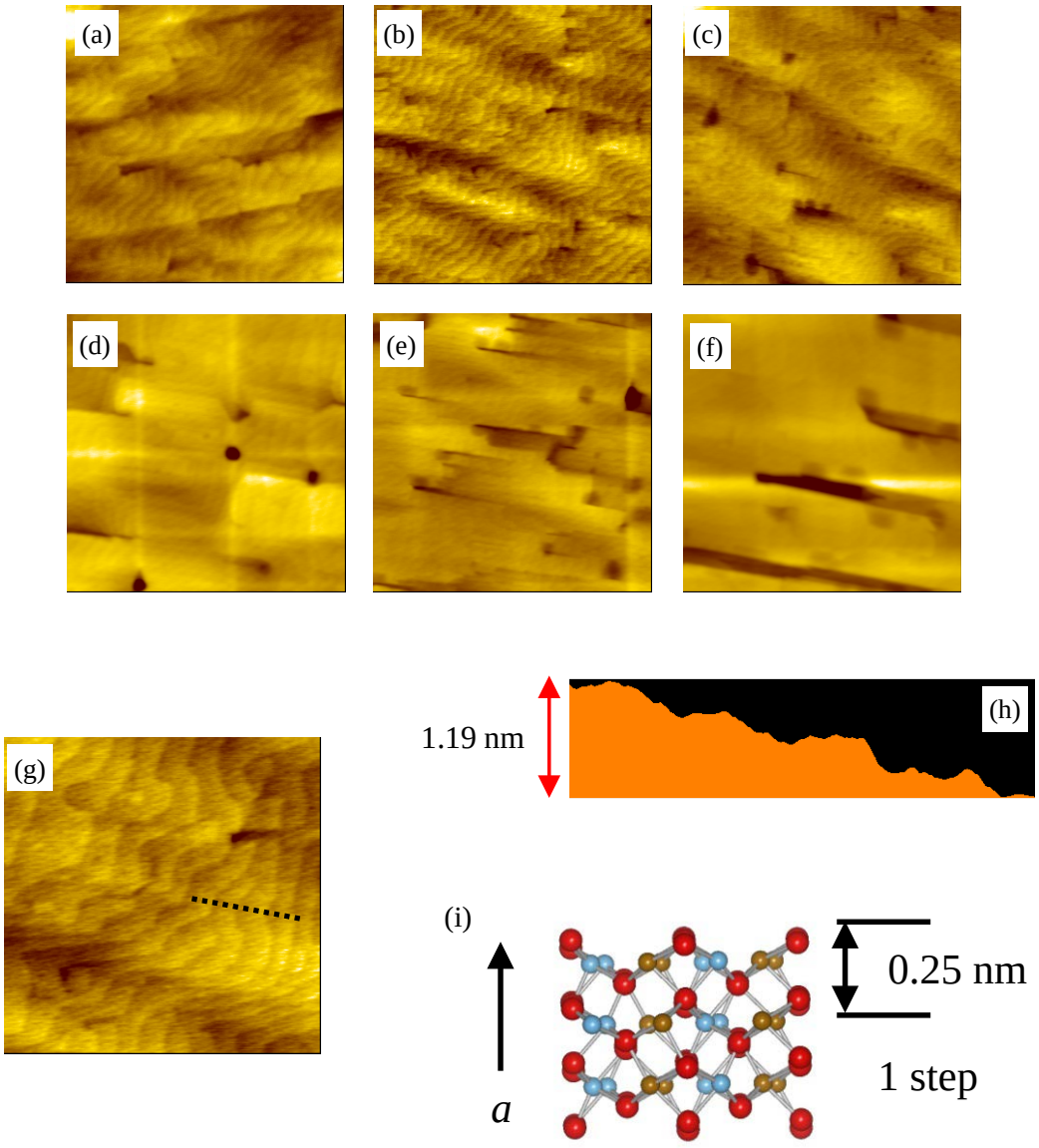

Fig. 4.5 AFM images of the surface morphology for $FeTiO_3$–Fe_2O_3 thin films grown at (a) Po_2 = 1.0 × 10^{-3} Pa and T_S = 850 ºC, (b) Po_2 = 2.0 × 10^{-3} Pa and T_S = 850 ºC, (c) Po_2 = 3.0 × 10^{-3} Pa and T_S = 850 ºC, (d) Po_2 = 1.0 × 10^{-3} Pa and T_S = 900 ºC, (e) Po_2 = 2.0 × 10^{-3} Pa and T_S = 900 ºC, and (f) Po_2 = 3.0 × 10^{-3} Pa and T_S = 900 ºC. (g) The magnified image of Fig. 4.5 (b). (h) The cross-section image along the black broken line in Fig. 4.5 (g). (i) Schematic illustration of $FeTiO_3$ depicted by VESTA software [10].

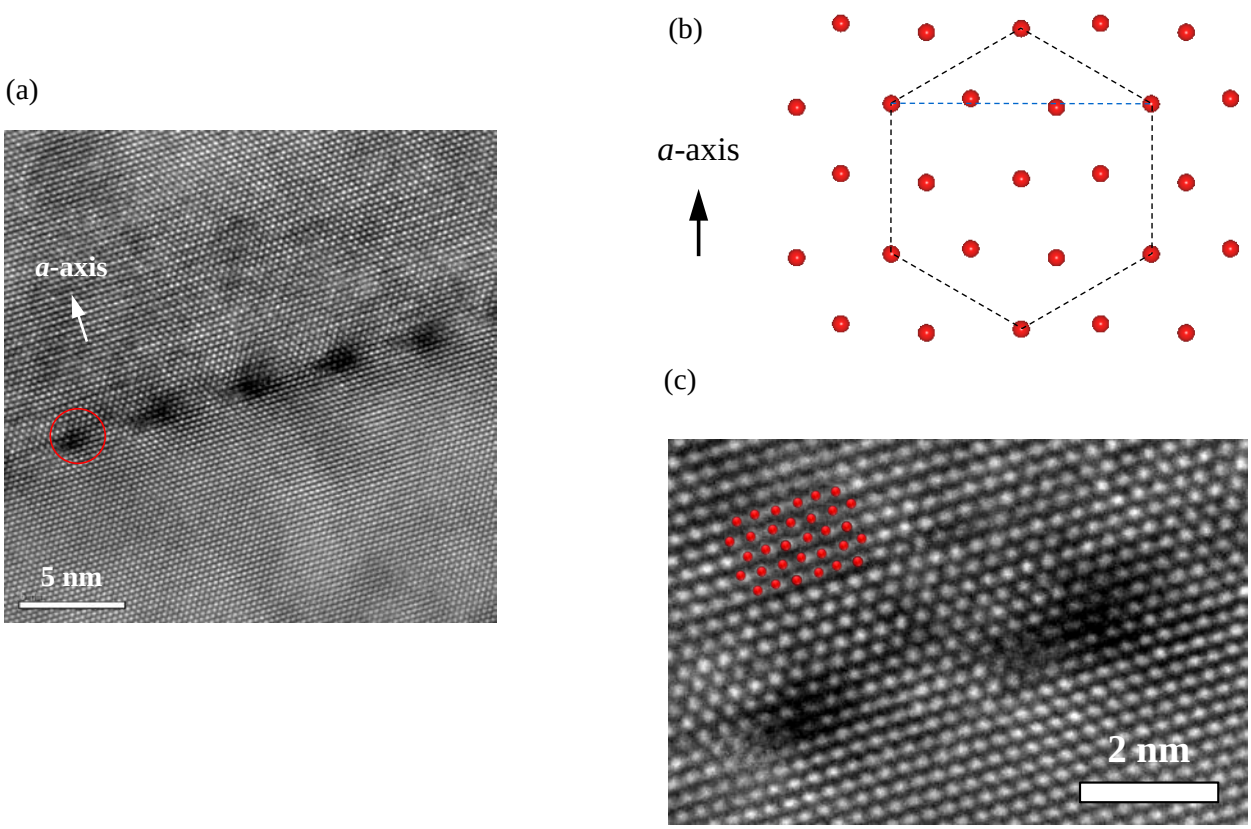

Fig. 4.6 (a) Cross-sectional HR-TEM image of the interface between $FeTiO_3$–Fe_2O_3 thin film and α–Al_2O_3 $(11\bar{2}0)$ substrate. The electron beam was irradiated along *c*-axis of substrate. The red open-circle indicates one of dislocation cores at the interface. (b) Schematic illustration for the hexagonal close-packed lattice plane (C-plane) of O^{2-} anions (red balls) in α–Al_2O_3 and $FeTiO_3$–Fe_2O_3 depicted VESTA software [10]. The black broken line indicates the regular hexagon of O^{2-} anions. (c) The magnified image around adjacent two dislocation cores in Fig. 4.6 (a). The schematic image of Fig. 4.6 (b) is superimposed on the upper left of the image.

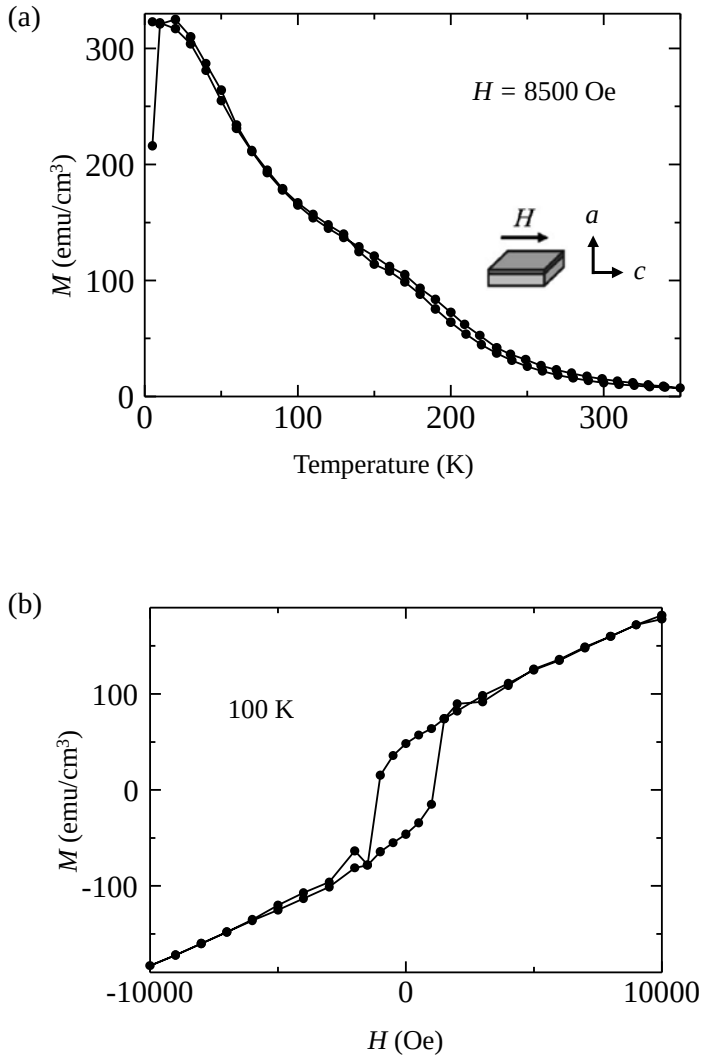

Fig. 4.7 (a) M-T curves for $FeTiO_3$–Fe_2O_3 thin film grown at $Po_2 = 2.0 \times 10^{-3}$ Pa and T_S = 850 ºC. The external magnetic field of 8500 Oe was applied parallel to the film surface (c-axis). (b) M-H curves at 100 K for the same thin film. The external magnetic field was also applied along c-axis of thin film.

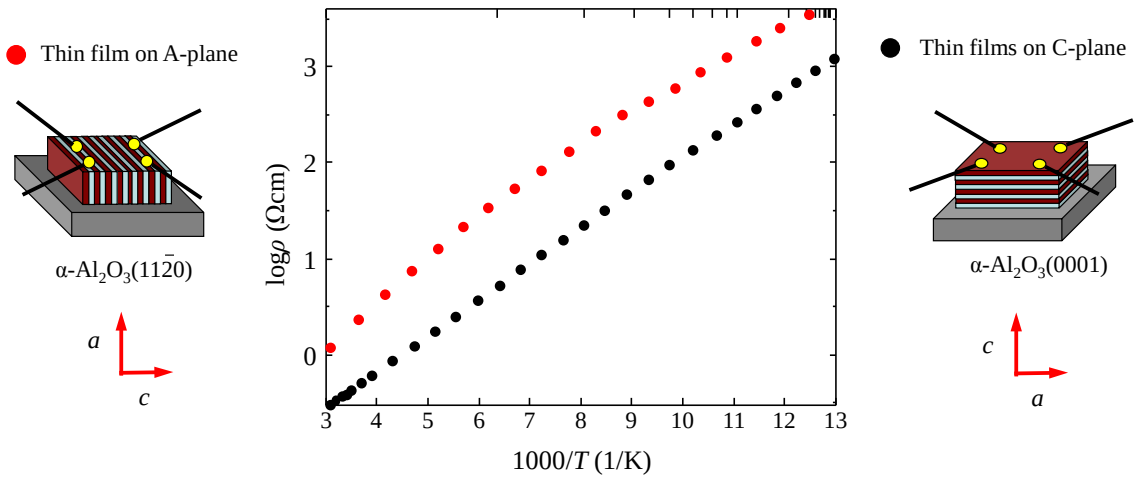

Fig. 4.8 Reciprocal T-dependence of ρ for $FeTiO_3$–Fe_2O_3 thin film grown on α–Al_2O_3 (11$\bar{2}$0) substrate at $Po_2 = 2.0 \times 10^{-3}$ Pa and T_S = 850 ºC (red closed circle), and thin film grown on α–Al_2O_3 (0001) substrate at $Po_2 = 1.0 \times 10^{-3}$ Pa and T_S = 700 ºC (black closed circle). The schematic images for van der Pauw method are illustrated on both left [for thin film grown on α–Al_2O_3 (11$\bar{2}$0) substrate] and right side [for thin film grown on α–Al_2O_3 (0001) substrate] of log ρ vs. 1000/T plot.

4.5 References

1. S. Datta, and B. Das, *Appl. Phys. Lett.* **56**, 665 (1990).
2. T. Miyazaki, and N. Tezuka, *J. Magn. Magn. Mater.***139**, L231 (1995).
3. Y. Takada, M. Nakanishi, T. Fujii, and J. Takada, *Appl. Phys. Lett.* **92**, 252102 (2008).
4. http://home.rzg.mpg.de/~mam/index.html
5. K. Simeonov, and D. Lederman, *Surf. Sci.* **603**, 232 (2009).
6. M. Kitayama, and A. M. Glaeser, *J. Am. Ceram. Soc.* **85**, 611 (2002).
7. J. W. Mathews, and A. E. Blakeslee, *J. Cryst. Growth* **27**, 188 (1974).
8. J. Narayan, and B. C. Larson, *J. Appl. Phys.* **93**, 278 (2003).
9. J. Narayan, A. K. Sharma, A. Kvit, C. Jin, J.F. Muth, and O. W. Holland, *Solid State Commun.* **121**, 9 (2002).
10. http://www.geocities.jp/kmo_mma/crystal/en/vesta.html
11. A. Goguitchaichvili, and M. Prévot, *J. Geophys. Res.* **105**, B2761 (2000).
12. Y. Ishikawa, *J. Phys. Soc. Jpn.* **13**, 37 (1958).

Chapter 5. The investigation of the electronic structure of ilmenite and ilmenite-hematite solid solution using hard X-ray photoemission spectroscopy

5.1 Introduction

5.1.1 Background

Transition-metal oxides with strongly correlated electrons have been intensively investigated in resent solid-state physics [1]. They have not only the degree of freedom in charge but also the one in spin. These two freedoms correlate to each other and enable the electric conduction of transition-metal oxides to be controlled by external magnetic field. This phenomenon is an essential operating principle of spintronics devices and now widely observed in a lot of transition-metal oxides such as $La_{1-x}Sr_xMnO_3$ [2–4].

As I have explained up to previous chapters, $FeTiO_3$–Fe_2O_3 solid solution has been considered as a promising material for spintronics application among the various kinds of transition-metal oxides [5–7], and fabrication of $FeTiO_3$–Fe_2O_3 thin films and investigations of their physical properties have been reported by lots of research groups including us [8–14]. In terms of the electric conduction mechanism in $FeTiO_3$–Fe_2O_3 solid solution, Ishikawa has carried out the electric property measurements in order to determine the valence states of cations in $FeTiO_3$ ($Fe^{2+}Ti^{4+}O_3$ or $Fe^{3+}Ti^{3+}O_3$) which cannot be clarified from the magnetic property measurements [6], as I introduced in Section 1.2.2.2. Ishikawa has concluded that the valence states of $FeTiO_3$ as $Fe^{2+}Ti^{4+}O_3$, and that the transfer of carriers between Fe^{2+} and Fe^{3+} is the main mechanism of electric conduction in $FeTiO_3$–Fe_2O_3 solid solution. First, if the valence state of cations in $FeTiO_3$ is $Fe^{3+}Ti^{3+}O_3$, the electric conduction will be hard to occur when $x < 0.73$ (*n*-type carrier) where Fe^{3+} and Ti^{3+} cations of $FeTiO_3$ are mixed into Fe^{3+} of α–Fe_2O_3. On the other hand, the carrier transfer is expected to occur between Fe^{2+} and Fe^{3+} in the case of $Fe^{2+}Ti^{4+}O_3$ dissolves into α–$Fe^{3+}{}_2O_3$, and the carrier is considered to be extra electrons on Fe^{2+}. In the range of $x > 0.73$ (*p*-type carrier) where $FeTiO_3$ is the host material, two conduction

models are expected; carrier transfer between (Fe^{2+} and Fe^{3+}) pair or (Ti^{3+} and Ti^{4+}) one. However, the former is expected to occur because the activation energy (E) estimated from the temperature-dependence of electric resistivity ρ (ρ–T) measurement is almost the same between the specimens with $x < 0.73$ and $x > 0.73$ [see also Fig. 1.2.6 (a)]. The E of carrier transfer between (Fe^{2+} and Fe^{3+}) pair or (Ti^{3+} and Ti^{4+}) one seems different and should change with the composition if the transfer mechanism changes from the former to the latter by $x = 0.73$. Therefore, the carrier transfer is considered to occur between Fe^{2+} and Fe^{3+} even when $x > 0.73$ where the extra holes of Fe^{3+} are considered to transfer to Fe^{2+}.

Although Ishikawa has suggested above electric conduction mechanism for $FeTiO_3$–Fe_2O_3 solid solution, its electronic structure has not been clarified experimentally nor investigated by using theoretical calculations, which are important for understanding the mechanism of electron conduction in $FeTiO_3$–Fe_2O_3 solid solution. In this chapter, I carried out hard X-ray photoemission spectroscopy (HX-PES) measurement on $FeTiO_3$ and $x FeTiO_3 \cdot (1–x) Fe_2O_3$ (x = 0.6 and 0.8) samples in order to investigate the electronic structure and electric conduction mechanism of $FeTiO_3$ and $FeTiO_3$–Fe_2O_3 solid solution.

5.1.2 Previous reports on the electric structure of $FeTiO_3$

As opposed to $FeTiO_3$–Fe_2O_3 solid solution, many theoretical and experimental researches have been dedicated to the investigation of the electronic structure and electric conduction mechanism on $FeTiO_3$ [15–20]. In this section, I briefly introduce some representative reports.

Fig. 5.1 illustrates the schematic image for the crystal structure of $FeTiO_3$ depicted by VESTA software [21]. $FeTiO_3$ has a corundum-based structure where oxide anions arrange into a distorted hexagonal close packed sublattice, and the two-third of their octahedral interstices is occupied by cations. $FeTiO_3$ is composed of alternatively stacked Fe and Ti cation octahedra along its c-axis as illustrated in Fig. 1.2.1. One Fe octahedron (brown one in Fig. 5.1) shares three edges with other Fe octahedra inside the same layer, a face with a Ti octahedron (blue one in Fig. 5.1) in the adjacent layer and the opposite face with an empty octahedral site. Therefore, it is expected that the charge transfer will occur between Fe and Ti octahedra through the shared face where Fe and Ti 3d orbitals overlap, and many research group have suggested the charge transfer notated by $Fe^{2+}+Ti^{4+} \rightarrow Fe^{3+}+Ti^{3+}$ through the shared octahedral face [17–20].

In terms of the investigation for the electronic structure of $FeTiO_3$, one of the most representative reports is the molecular-orbital calculation by Sherman [15]. Sherman explained the charge transfer mechanism in Fe-Ti oxides and silicates including $FeTiO_3$ using $(FeTiO_{10})^{14-}$ cluster model of Fig. 5.2 (a). In this model, Fe 3*d* state splits to lower Fe 3*d* α-state overlapping with O 2*p* band and higher Fe 3*d* β-state by the intra-atomic exchange energy [Fig. 5.2 (b)], and $Fe^{2+}+Ti^{4+} \rightarrow Fe^{3+}+Ti^{3+}$ charge transfer is considered to occur by exciting an electron from $16a_1$ orbital (Fe t_{2g}) to $17a_1$ one (Ti t_{2g}) as illustrated in Fig. 5.2 (c). Recently, Wilson *et al.* have also calculated the DOS of $FeTiO_3$ [Fig. 5.3] by first-principal calculation using Becke's three parameter hybrid functional (B3LYP) approximation [16]. Their DOS is similar to Sherman's molecular-orbital diagram, and they have also confirmed the split of Fe 3*d* state.

5.1.3 HX-PES

PES is one of the most effective methods in order to investigate the electronic structure of materials. It analyzes the kinetic energy (E) of electrons emitted from the materials which is described as,

$$E = h\nu - E_b$$

where $h\nu$ and E_b means the excitation energy of the light source and the binding energy of emitted electron, respectively. Because the magnitude of $h\nu$ is constant, the value of E_b, therefore, the electronic state of materials can be estimated by analyzing E via PES experiment. The knowledge on band structure of materials can be extracted from PES spectrum for the valence band of materials, whereas the chemical bond state or valence of each atom can be estimated from the core-level spectrum of materials. The main problem for PES experiment is its too short probe length which is usually less than several nm. The specific X-ray of Mg-Kα [excitation energy ($h\nu$): 1.25 keV] or Al-Kα ($h\nu$ = 1.48 keV) is generally utilized as an excitation light source for PES measurement because of its narrow band width which gives higher energy resolution for PES spectrum. However, in the case of such soft X-ray light sources with low $h\nu$, the inelastic mean free path of emitted electrons is as short as several nm

or even can be less than 1 nm because of the low *E* of them. Therefore, obtained PES spectrum mainly derives from the surface of materials which is often deteriorated (oxidized) by exposed to the air. On the other hand, HX-PES utilizes hard X-ray with *hv* of around 8 keV and the band width of several 10 meV, which enables the probe length to be several 10 nm and high energy resolution for PES spectrum. Therefore, the surface deterioration of specimens can be excluded in HX-PES experiment; which means obtain spectra reflect the bulk nature of materials compared to the usual PES.

5.2 Experimental procedure

5.2.1 Sample preparation and characterizations

$FeTiO_3$ bulk specimen was prepared by usual solid-state reaction method. The powder reagents of α–Fe_2O_3 (Kojundo Chemical Laboratory Co. Ltd., purity: 99.99%) and TiO_2 (Kojundo Chemical Laboratory Co. Ltd., purity: 99.9%) were mixed with alumina mortar and pestle and heated in air at 900 ºC for 12 h. The mixture was re-grounded and pressed into pellet. The pellet was sintered in alumina tube furnace in CO + CO_2 (CO = 40%) atmosphere at 1300 ºC for 24 h [22]. $0.6FeTiO_3 \cdot 0.4Fe_2O_3$ and $0.8FeTiO_3 \cdot 0.2Fe_2O_3$ thin films were fabricated on α–Al_2O_3 (0001) single crystal substrates by pulsed laser deposition (PLD) method using KrF excimer laser (λ = 248 nm, 2 Hz, 2 J/cm). The preparation condition of PLD targets and thermal annealing condition of α–Al_2O_3 (0001) substrates were the same as described in Chapter 2. The substrate temperature and oxygen partial pressure during deposition were kept at 700 ºC and 1.0×10^{-3} Pa, respectively.

The crystal structures of these samples were characterized by X-ray diffraction (XRD) with Cu Kα radiation; RINT2500 (Rigaku) for bulk $FeTiO_3$ and ATX-G (Rigaku) for $FeTiO_3$–Fe_2O_3 thin films, respectively. The measurements of magnetization were carried out using a superconducting quantum interference device (SQUID) magnetometer (MPMS, Quantum Design). The film thickness was evaluated to be about 70 nm using a surface profiler.

5.2.2 HX-PES measurement

The HX-PES measurement was carried out at BL47XU beam-line of SPring-8 (*hv* = 7.94

keV) at room temperature. The total energy resolution was set to 250.06 meV. The take-off angle of photoelectrons was set at 87º to reduce the effect of surface contamination on the HX-PES spectrum as illustrated in Fig. 5.4. The peak position of the obtained spectra was calibrated using C 1*s* peak position (binding energy: 284.6 eV).

5.3 Results and Discussion

5.3.1 Crystal structure and magnetic properties of HX-PES samples

Fig. 5.5 shows the XRD pattern and the temperature dependence of magnetization (*M-T* curve) for $FeTiO_3$ bulk sample. It can be safely said that the sample is almost single phase of $FeTiO_3$ which includes little impurity (Although the reflection from rutile 110 appears at 2θ = 27.5º, the amount of it is quite a little. Note that the vertical axis is logarithmic scale.). The Néel temperature of the bulk sample is 59 K [Fig. 5.5 (b)], which is well coincident with the one of previous reports [23].

Out-of-plane XRD patterns for $0.6FeTiO_3{\cdot}0.4Fe_2O_3$ and $0.8FeTiO_3{\cdot}0.2Fe_2O_3$ thin films were shown in Fig. 5.6, and the formation of (0001)-oriented ordered phase was confirmed. Fig. 5.6 (b) is the magnified image around 0006 peaks in Fig. 5.6 (a) where the slight deviation of peak position between two thin films indicates the difference of $FeTiO_3$ composition ratio (the lattice constants of $0.6FeTiO_3{\cdot}0.4Fe_2O_3$ is smaller than those of $0.8FeTiO_3{\cdot}0.2Fe_2O_3$, resulting in the 0006 peak position of $0.6FeTiO_3{\cdot}0.4Fe_2O_3$ in higher angle). The magnetic properties of fabricated thin films [Fig. 5.7] are identical to those of thin films I reported previously [12, 13], indicating both thin films are ferrimagnets.

From XRD and magnetic property measurements, the samples for HX-PES measurement are identical to the sample in previous reports whose crystal structure and physical properties have been well investigated. This indicates that the results of HX-PES measurement for the present samples can be applied to a clarification of the origin of physical properties in $FeTiO_3$ and $FeTiO_3$–Fe_2O_3 solid solution which have been reported by many research groups. In the following sections, I denote $0.6FeTiO_3{\cdot}0.4Fe_2O_3$ and $0.8FeTiO_3{\cdot}0.2Fe_2O_3$ samples as “6 : 4” and “8 : 2” respectively.

5.3.2 HX-PES spectra for $FeTiO_3$ and $FeTiO_3$–Fe_2O_3 solid solution samples

Fig. 5.8 shows the entire HX-PES spectra for $FeTiO_3$, 8 : 2 and 6 : 4 samples. Because all peaks except for C 1*s* (around 285 eV) are derived from Fe, Ti and O, it is confirmed that the samples contains no other elements besides Fe, Ti and O as impurities (C 1*s* peak is derived from the organic compound in the air which is adsorbed on the sample surface). Especially, peaks derived from Al were not observed in the case of thin film samples, and this means that the hard X-ray did not reach to α–Al_2O_3 substrate. Therefore, the probe depth is estimated to be less than 70 nm.

Fe 2*p* and Ti 2*p* core-level HX-PES spectra are shown in Fig. 5.9. In Fig. 5.9 (a), Fe^{3+} component increases whereas the Fe^{2+} component decreases, as the composition ratio of α–Fe_2O_3 in the samples increases. Because $FeTiO_3$ and α–Fe_2O_3 are nominally described as $Fe^{2+}Ti^{4+}O^{2-}{}_3$ and α–$Fe^{3+}{}_2O^{2-}{}_3$, the increase in the ratio of Fe^{3+}/Fe^{2+} observed in Fig. 5.9 (a) is reasonable. On the other hand, there is no difference among three Ti 2*p* spectra [Fig. 5.9 (b)] dominantly consisting of Ti^{4+} component, which means that Ti cations are still tetravalent even in $FeTiO_3$–Fe_2O_3 solid solution. No variation was also observed in O 1*s* core-level spectra of these samples (not shown).

Fig. 5.10 shows the valence band spectra of these samples. As contrast to Fe 2*p* and Ti 2*p* spectra in Fig. 5.9, the peak position shift indicated by arrows in Fig. 5.10 (b) was observed in these valence band spectra.

5.3.3 The electric conduction mechanism of $FeTiO_3$–Fe_2O_3 solid solution

By comparing Fig. 5.3 with 5.10 (a), one can see that the valence band spectrum for bulk $FeTiO_3$ sample is coincident with the theoretical spectra calculated by Wilson *et al.*, where the valence structure consists of strongly mixed Fe 3*d* and O 2*p* component. Therefore, the experimental spectrum for $FeTiO_3$ sample within 2–9 eV is mainly attributed to mixed Fe 3*d* α-state and O 2*p* component, whereas the one within 0–1.5 eV is due to Fe 3*d* β-state. Because the shape of valence band spectra for 8 : 2 and 6 : 4 thin films is also the same as that of bulk $FeTiO_3$, the origin and components of electronic structure of $FeTiO_3$–Fe_2O_3 solid solution are considered to be the same as that of $FeTiO_3$. However, the peak corresponding to the Fe 3*d* β-state shifts toward the lower binding energy, as $FeTiO_3$ composition ratio x ($0 < x <$

1) decreases from 1 to 0.6. I consider that the peak shift among three samples is due to the shift in Fe 3*d* components corresponding to the variation in the electron correlation while $FeTiO_3$ forms solid solution with α–Fe_2O_3. Therefore, I also consider that the electric conduction in $FeTiO_3$–Fe_2O_3 solid solution mainly due to the electron hopping between Fe^{2+} and Fe^{3+} rather than between Fe^{2+} and Ti^{4+}.

As I introduced in Section 5.1.2, the electron conduction mechanism in $FeTiO_3$ is considered to the charge transfer between Fe^{2+} (d^6) and Ti^{4+} (d^0) ($Fe^{2+}+Ti^{4+} \rightarrow Fe^{3+}+Ti^{3+}$) through the shared face between Fe and Ti octahedra where their 3*d* orbital overlaps moderately, and the same charge transfer is expected to occur in the electric conduction in $FeTiO_3$–Fe_2O_3 solid solution. Indeed, I have conducted soft X-ray magnetic circular dichroism (XMCD) measurement for $FeTiO_3$–Fe_2O_3 solid solution thin films in order to investigate magnetic and electronic structure of $FeTiO_3$–Fe_2O_3, and confirmed that Ti^{4+} cations (d^0) have 3*d* electrons due to the hybridization of 3*d* orbital between Ti^{4+} and Fe^{2+} cations. Fig. 5.11 shows the Ti-$L_{2,3}$ edge X-ray absorption spectroscopy (XAS) and XMCD spectra for $0.6FeTiO_3 \cdot 0.4Fe_2O_3$ thin film. The experimental spectra were compared to theoretical spectra calculated by first-principles multi-electron calculation based on density functional theory (DFT) and configuration interaction (CI) method [24, 25]. The details of experimental procedure and theoretical calculation are given elsewhere [26]. Because the shape of experimental XAS spectrum is not similar to that of theoretical Ti^{3+} spectrum but Ti^{4+} one, the valence of Ti cations is 4+, which is identical to Ti 2*p* core-level HX-PES spectrum in Fig. 5.9 (b). However, Ti-$L_{2,3}$ edge XMCD spectrum, which should not be observed in the case of non-magnetic d^0 cations, was obtained. This indicates that Ti^{4+} cations partly contain electrons and that they are magnetically polarized. Therefore, I have experimentally confirmed that $Fe^{2+}+Ti^{4+} \rightarrow Fe^{3+}+Ti^{3+}$ charge transfer also occur in the case of $FeTiO_3$–Fe_2O_3 solid solution.

However, the lower electric resistivity (ρ) of $FeTiO_3$–Fe_2O_3 solid solution than that of $FeTiO_3$ by 2-digits in magnitude as shown in Fig. 1.2.6 (a) cannot be explained, if the dominant electric conduction mechanism is $Fe^{2+}+Ti^{4+} \rightarrow Fe^{3+}+Ti^{3+}$ charge transfer along crystallographic *c*-axis of them. Fig. 5.12 (a) illustrates the schematic image of cation arrangement in ordered-phase of $FeTiO_3$–Fe_2O_3 solid solution. As I explained in Section 1.2.1, it has alternating Fe-only [layer A in Fig. 5.12 (a)] and Ti-rich cation (layer B) layers. The valence of Fe cations is only 3+ in

layer B, whereas the mixture of Fe^{2+} and Fe^{3+} exists in layer A. Therefore, there are two Fe octahedra which share one face along its *c*-axis, and the charge transfer between Fe^{2+} in layer A and Fe^{3+} in layer B is also considered to occur due to the overlap of two Fe 3*d* orbitals. However, these adjacent layer A and B are antiferromagnetically coupled; which means the electron transfer between these layers is prevented as illustrated in Fig. 5.12 (c).

On the other hand, Fe cations in the same layer A are ferromagnetically coupled, and the electron transfer is considered to be allowed along in-plane direction [Fig. 5.12 (b)]. I consider that this in-plane electron transfer between Fe cations is the dominant electron conduction mechanism in $FeTiO_3$–Fe_2O_3 solid solution, which also have been suggested by Mukerjee [27]. The difference in the magnitude of ρ between $FeTiO_3$ and $FeTiO_3$–Fe_2O_3 solid solution can be explained by the variation of the electron correlation between two Fe cations. In $FeTiO_3$, all Fe cations are Fe^{2+}, and the electron correlation keeps electrons localized on their own Fe^{2+} site where one electron already exists in β-state t_{2g} orbital. In $FeTiO_3$–Fe_2O_3 solid solution, however, Fe^{3+} (d^5) reduce this electron correlation somewhat and the electron transfer is considered to occur within ferromagnetically coupled Fe^{2+} and Fe^{3+} mixed cation layer. I consider that insulator $FeTiO_3$ turns into semiconductor with forming $FeTiO_3$–Fe_2O_3 solid solution by this mechanism, and that the peak shift toward the lower binding energy in the valence band HX-PES spectra [Fig. 5.10 (b)] corresponds to the narrowing of the Mott-Hurbbard gap. Similar peak shift at valence band spectra was reported by Takaobushi *et al.* for $Fe_{3-x}M_xO_4$ (*M* = Mn, Zn) spinel oxide, where the authors have also attributed the peak shift to the variation in the electron correlation [28]. The tendency in Fig. 5.10 (b) is coincident with the composition dependence of ρ measurement for bulk $FeTiO_3$–Fe_2O_3 solid solution specimens conducted by Ishikawa, where ρ decreases as *x* decreases from 1 and reaches minimum when $x = 0.5$ [see also Fig. 1.2.6 (b)] [6].

5.4 Conclusions

I have conducted the HX-PES measurement on $FeTiO_3$ and $x FeTiO_3 \cdot (1-x)Fe_2O_3$ ($x = 0.6$ and 0.8) samples in order to investigate the electronic structure and electric conduction mechanism of $FeTiO_3$–Fe_2O_3 solid solution. The valence band structures of $FeTiO_3$ and $FeTiO_3$–Fe_2O_3

solid solution are similar to each other, and correspond to the previous theoretical DOS of $FeTiO_3$, indicating that the electronic structure of $FeTiO_3$–Fe_2O_3 solid solution also consists of strongly mixed Fe 3*d* and O 2*p* component. A peak shift was observed in the valence band spectra of those samples, whereas such a shift was not observed in the Fe 2*p*, Ti 2*p* and O 1*s* core-level spectra. I consider that the observed peak shift is due to the variation in the electron correlation of Fe 3*d* components while $FeTiO_3$ forms solid solution with α–Fe_2O_3. The intermixture of Fe^{2+} and Fe^{3+} reduces the electric correlation, and electron transfer between Fe^{2+} and Fe^{3+} occurs easily within the C-plane direction of $FeTiO_3$. I propose that insulator $FeTiO_3$ turns into semiconductor with forming $FeTiO_3$–Fe_2O_3 solid solution by this mechanism, and the electron transfer between Fe^{2+} and Fe^{3+} in C-plane direction is the dominant electric conduction mechanism in $FeTiO_3$–Fe_2O_3 solid solution rather than that between Fe^{2+} and Ti^{4+} in *c*-axis direction, which is considered to be the dominant electric conduction mechanism in $FeTiO_3$.

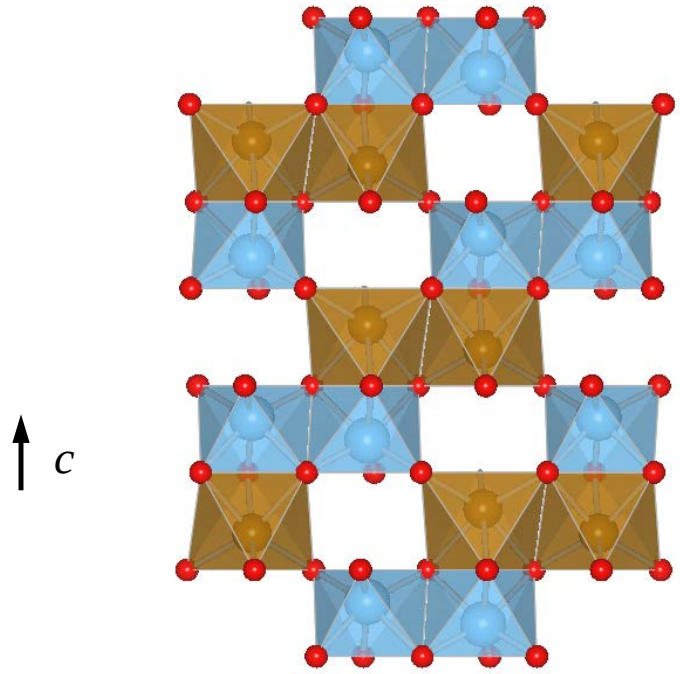

Fig. 5.1 Schematic illustration for the crystal structure of $FeTiO_3$ depicted by VESTA software [21]. Red, brown and blue balls indicate O^{2-}, Fe^{2+} and Ti^{4+} ions, respectively. Upper direction on the plane of paper corresponds to *c*-axis of $FeTiO_3$.

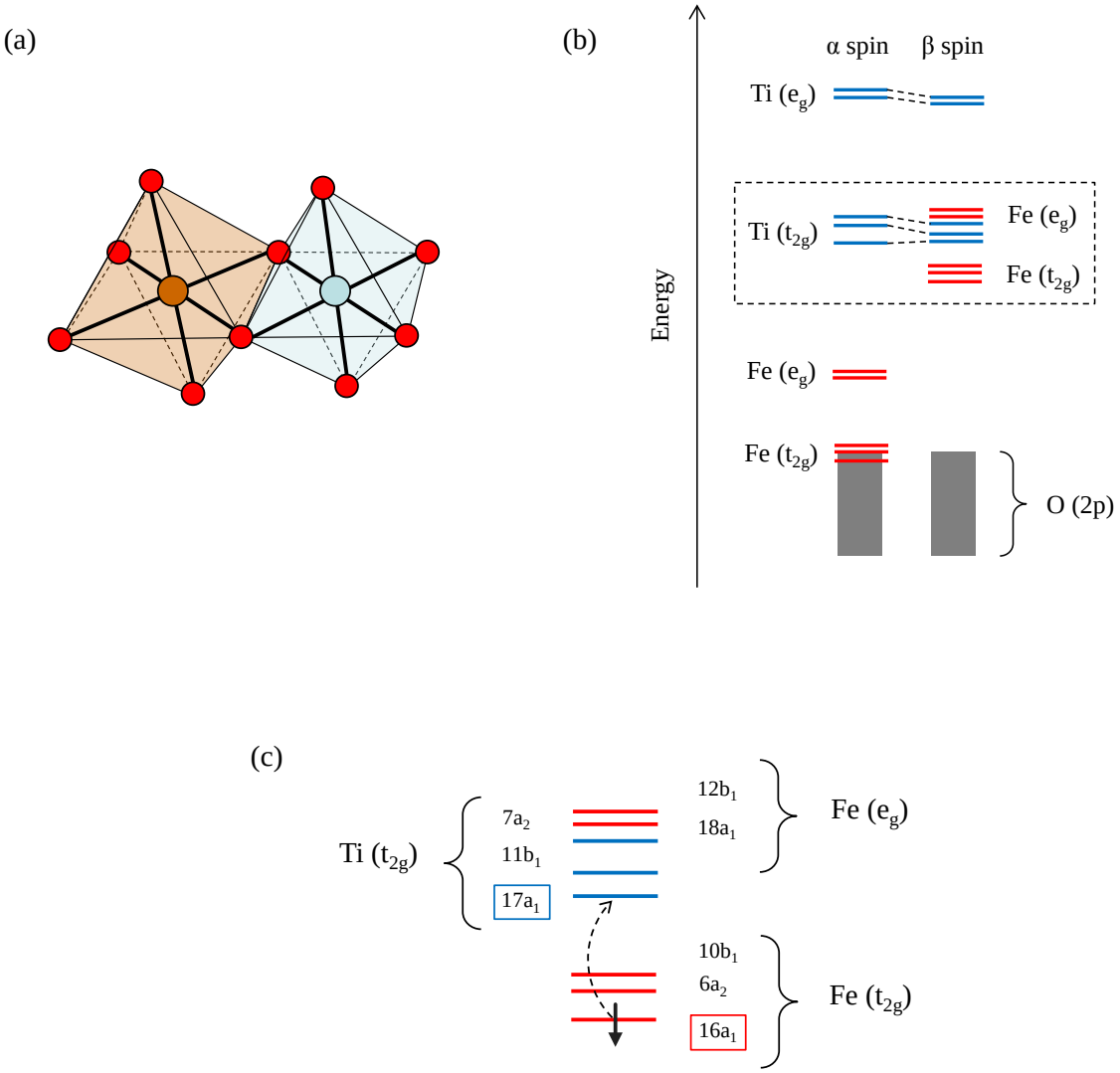

Fig. 5.2 (a) Schematic illustration for Sherman's $(FeTiO_{10})^{14-}$ cluster model [15]. Red, brown and blue balls indicate O^{2-}, Fe^{2+} and Ti^{4+} ions, respectively. (b) Molecular orbital diagram based on $(FeTiO_{10})^{14-}$ cluster model. Red and blue lines indicate Fe and Ti band, respectively. (c) Magnified image for the β–state molecular orbital diagram surrounded by broken line in Fig. 5.2 (b). Black solid arrow indicates an electron located on $16a_1$ orbital of Fe t_{2g}.

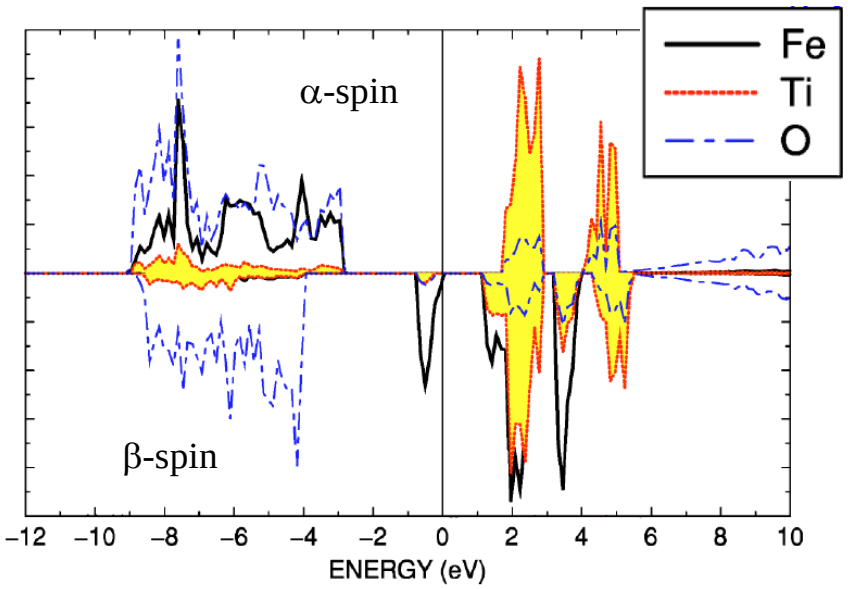

Fig. 5.3 The DOS of $FeTiO_3$ calculated by Wilson *et al.* with first-principal calculation using B3LYP approximation [16].

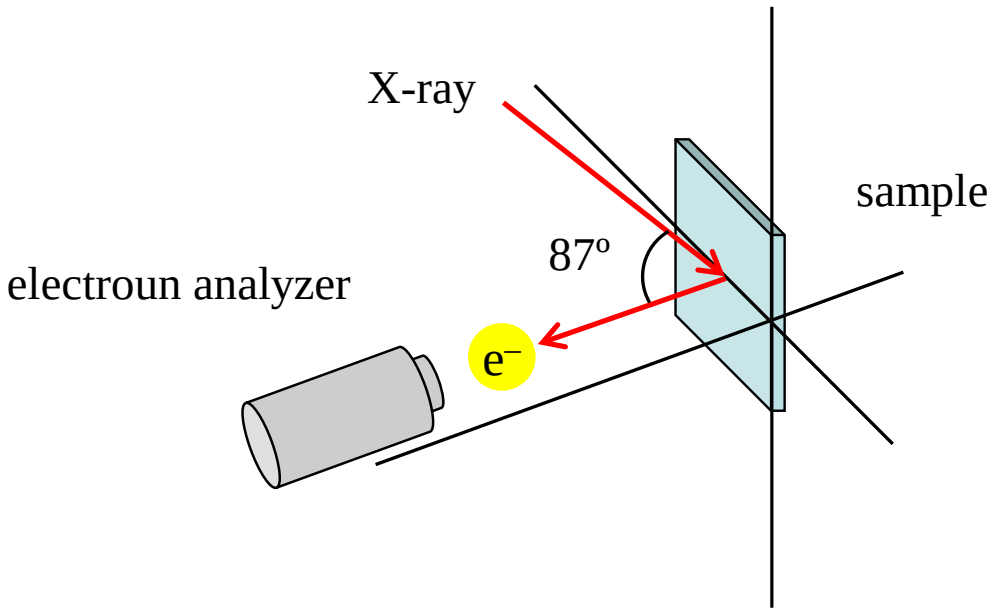

Fig. 5.4 Schematic illustration of the experimental configuration for HX-PES measurement.

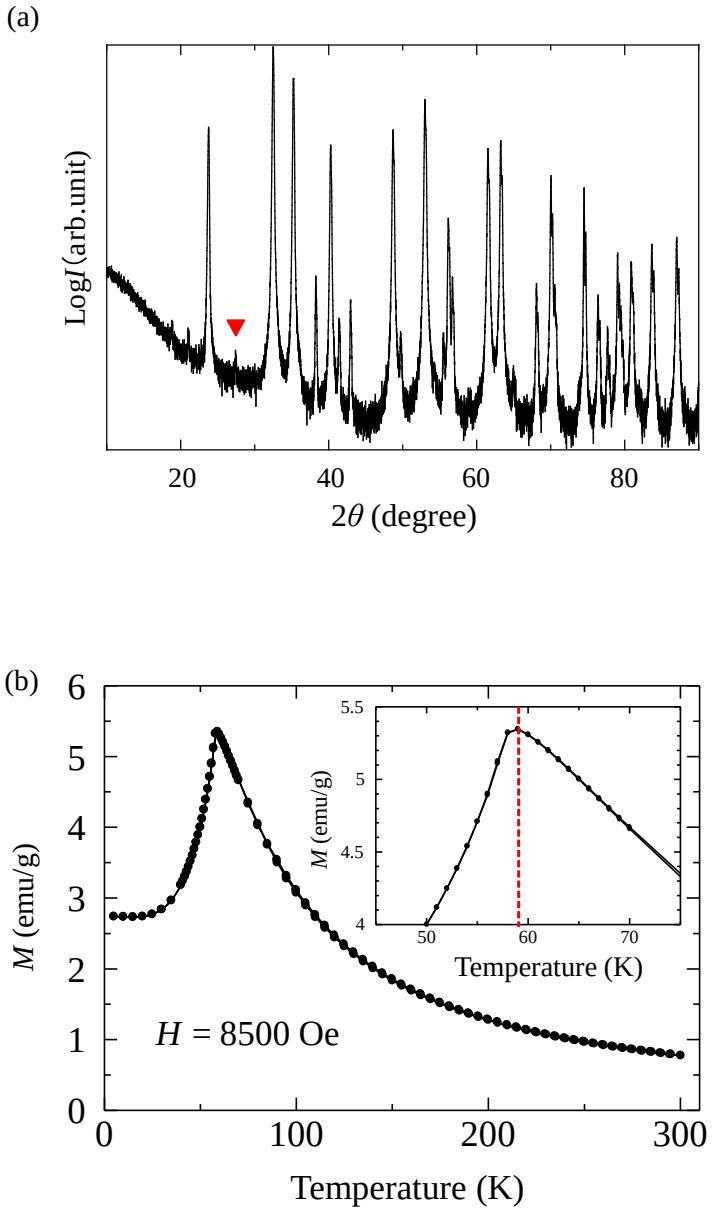

Fig. 5.5 (a) XRD pattern of $FeTiO_3$ bulk specimen. The peak indicated by red inverted triangle is the diffraction from rutile 110. (b) The *M-T* curve of $FeTiO_3$ bulk specimen. The applied external magnetic field is 8500 Oe. The inset shows the magnified part around Néel temperature.

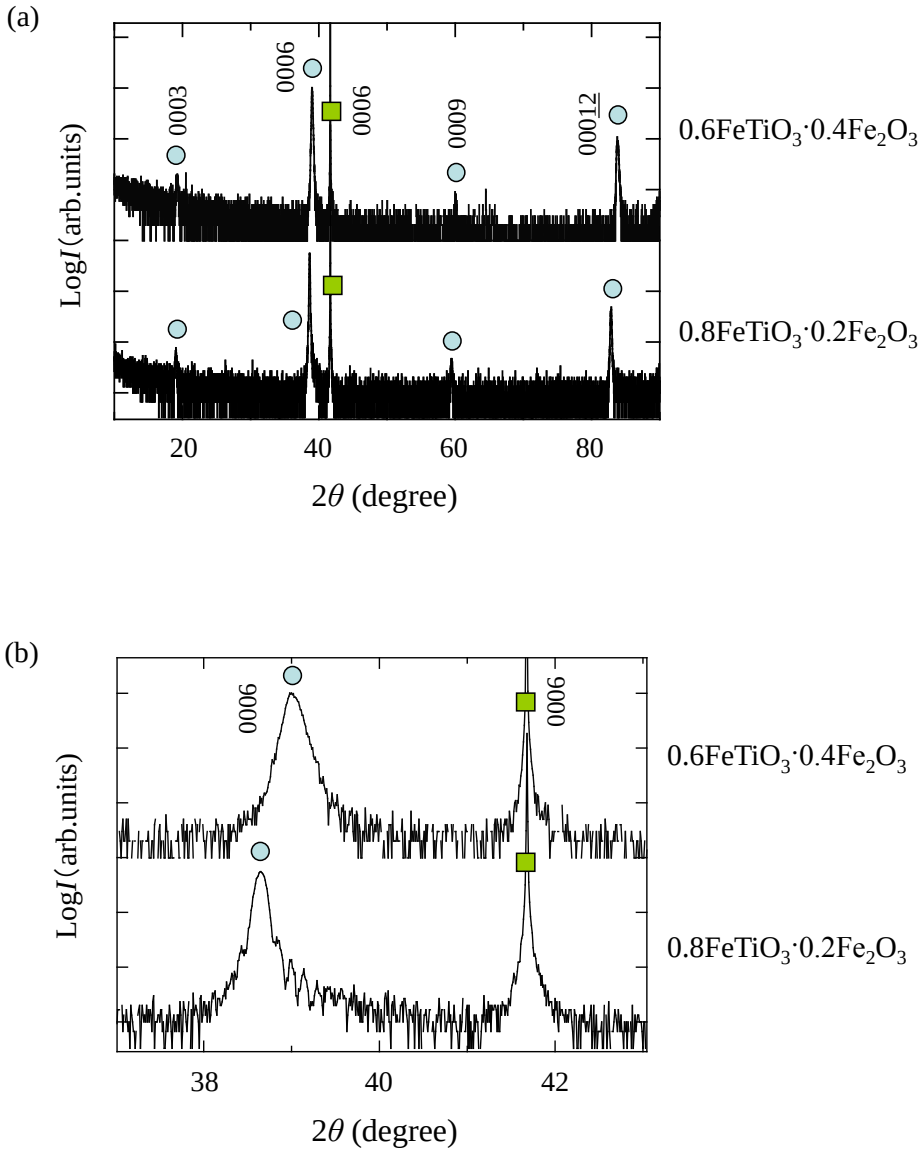

Fig. 5.6 (a) Out-of-plane XRD patterns for $0.6FeTiO_3 \cdot 0.4Fe_2O_3$ and $0.8FeTiO_3 \cdot 0.2Fe_2O_3$ thin films grown on α–Al_2O_3 (0001) substrates; ■: substrate, ○: ordered phase. (b) The magnified images around 0006 peaks in Fig. 5.6 (a).

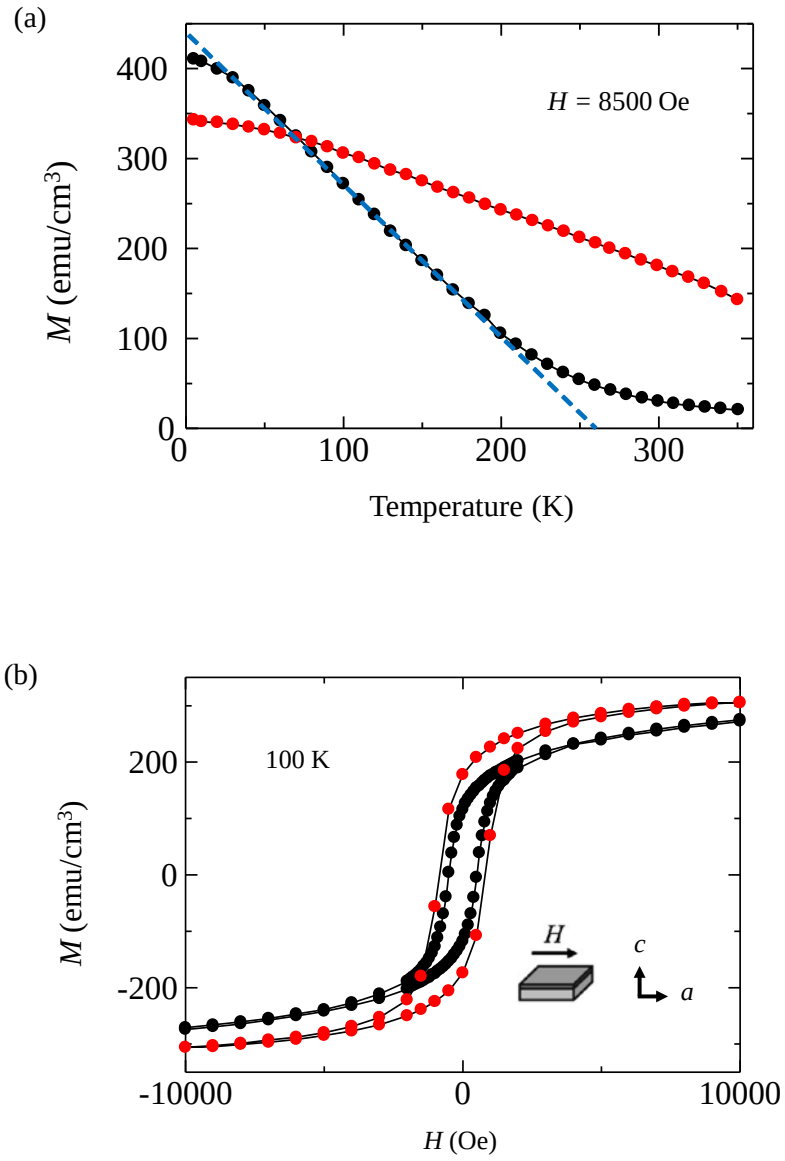

Fig. 5.7 (a) *M*–*T* curves for $0.6FeTiO_3 \cdot 0.4Fe_2O_3$ (red closed circle) and $0.8FeTiO_3 \cdot 0.2Fe_2O_3$ (black closed circle) thin films. The external magnetic field of 8500 Oe was applied parallel to the film surface. The ferrimagnetic Curie temperature of $0.8FeTiO_3 \cdot 0.2Fe_2O_3$ thin film is estimated to be 260 K from the intercept between the extrapolation of the linear part of *M* (blue broken line) and abscissa. (b) *M*–*H* curves at 100 K for the same thin films.

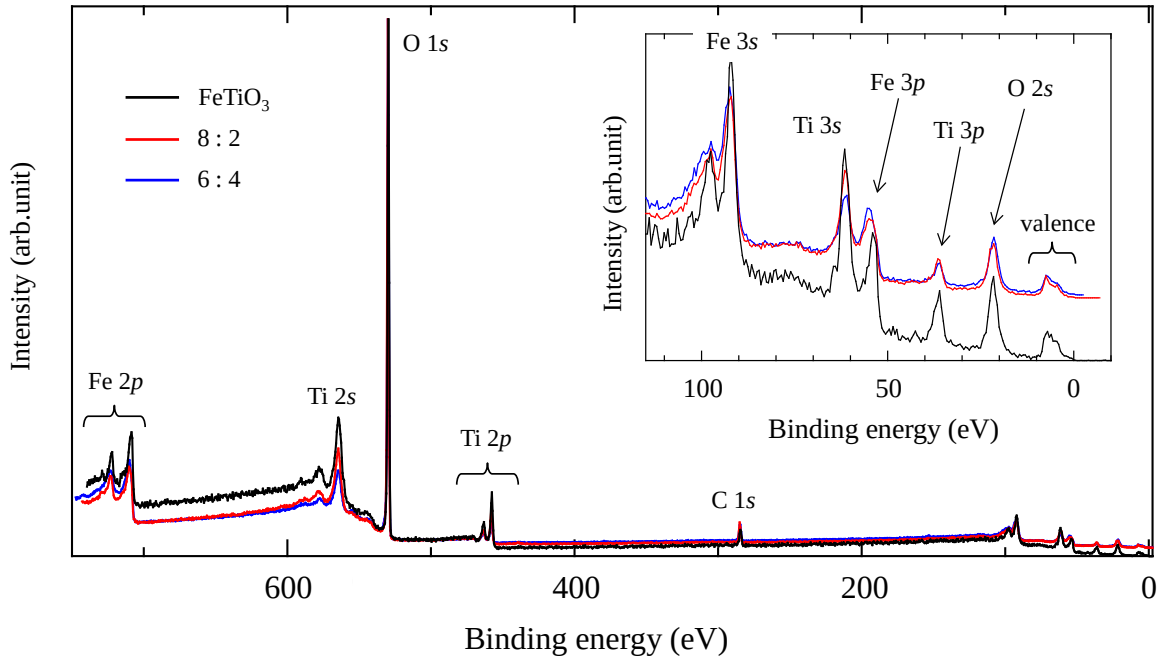

Fig. 5.8 The entire HX-PES spectra for $FeTiO_3$ (black line), $0.8FeTiO_3 \cdot 0.2Fe_2O_3$ (8 : 2) (red line) and $0.6FeTiO_3 \cdot 0.4Fe_2O_3$ (6 : 4) (blue line) samples. The inset shows the magnified image for the binding energy of 0-115 eV.

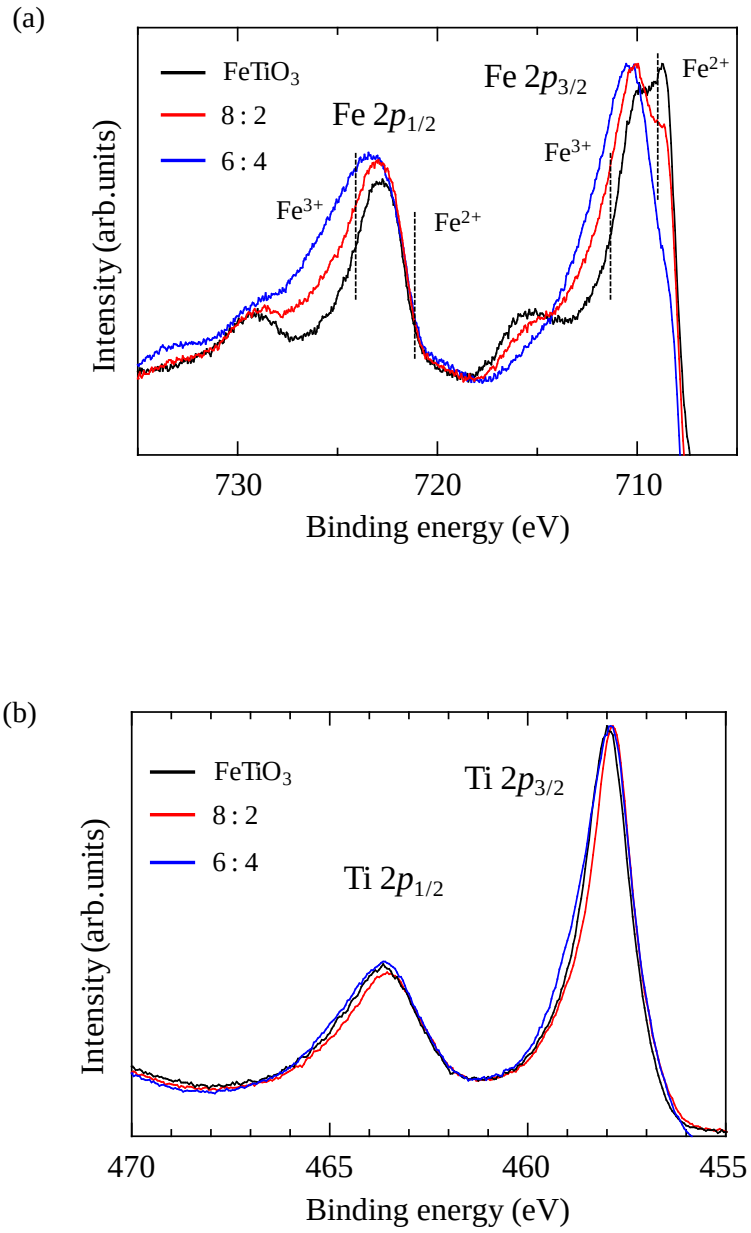

Fig. 5.9 (a) Fe 2*p* and (b) Ti 2*p* core-level spectra for $FeTiO_3$ (black line), $0.8FeTiO_3 \cdot 0.2Fe_2O_3$ (8 : 2) (red line) and $0.6FeTiO_3 \cdot 0.4Fe_2O_3$ (6 : 4) (blue line) samples. The components derived from Fe^{2+} and Fe^{3+} are indicated by black broken lines in Fig. 5.9 (a).

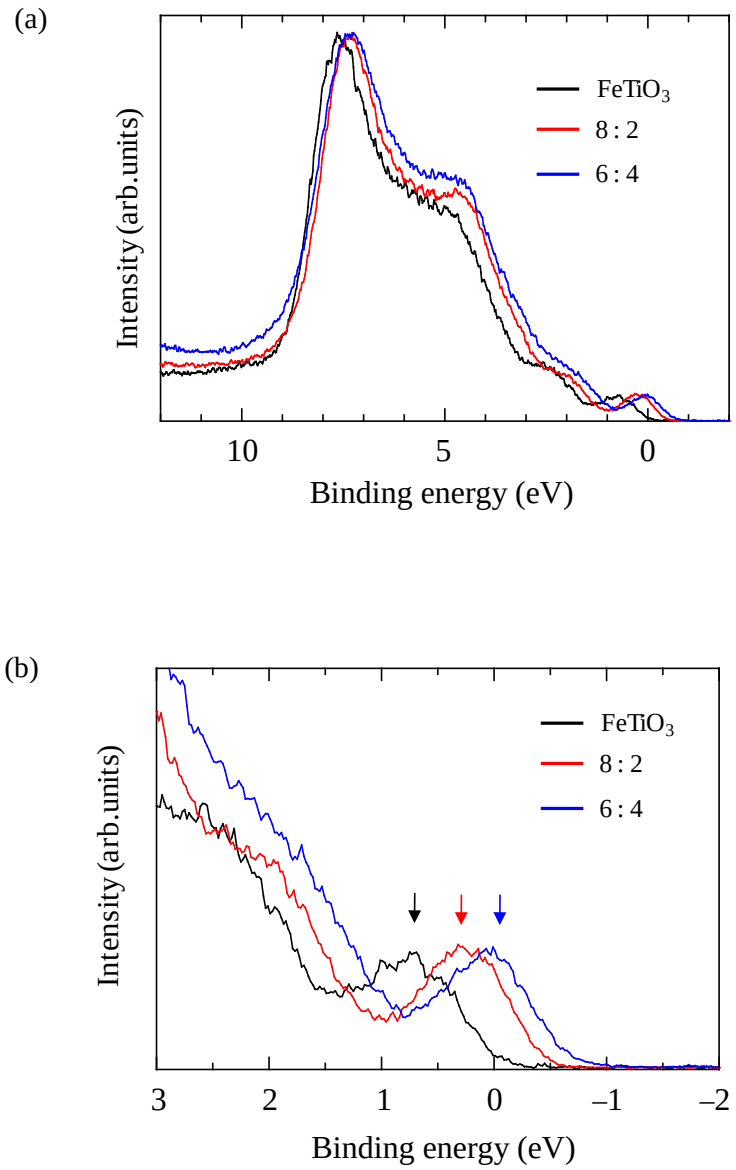

Fig. 5.10 (a) Valence band spectra for $FeTiO_3$ (black line), $0.8FeTiO_3 \cdot 0.2Fe_2O_3$ (8 : 2) (red line) and $0.6FeTiO_3 \cdot 0.4Fe_2O_3$ (6 : 4) (blue line) samples. (b) The magnified image of Fig. 5.10 (a) showing around binding energy of 0 eV. The peaks indicated by arrows correspond to the Fe 3d β-state.

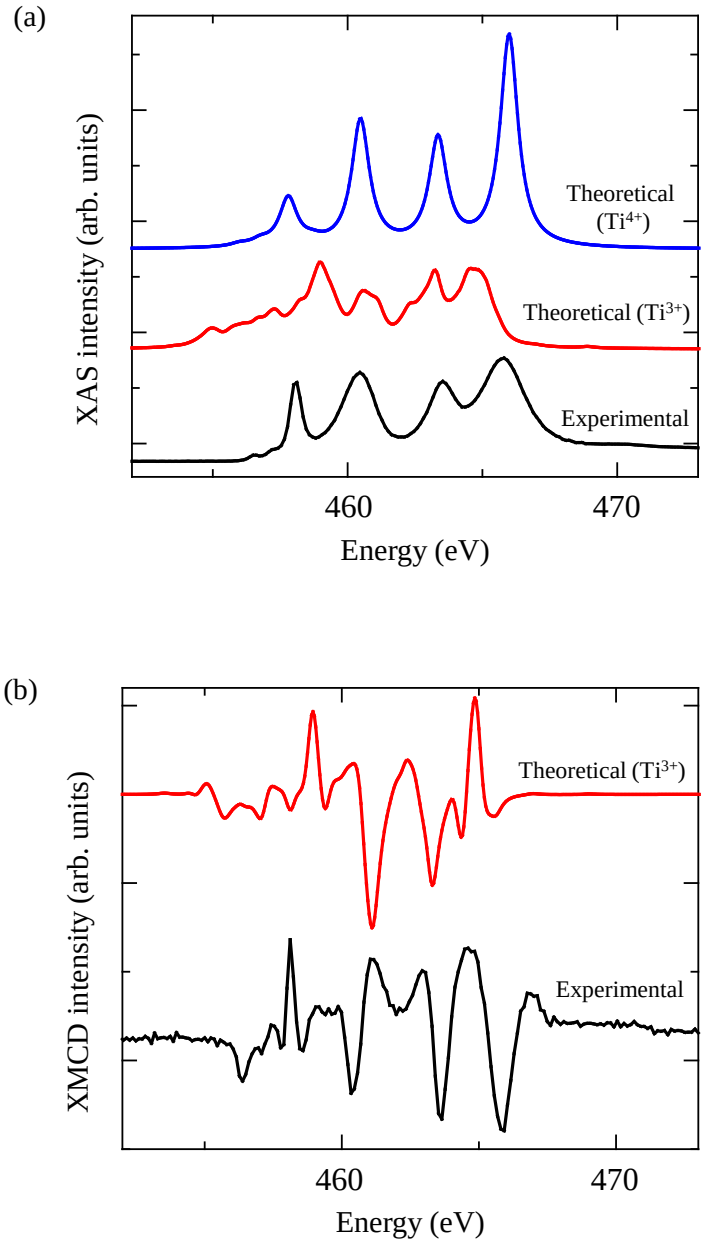

Fig. 5.11 Ti-$L_{2,3}$ edge (a) XAS, and (b) XMCD spectra for $0.6FeTiO_3 \cdot 0.4Fe_2O_3$ thin film sample. Black, red and blue solid lines indicate the experimental, theoretical Ti^{3+}, and theoretical Ti^{4+} spectra, respectively.

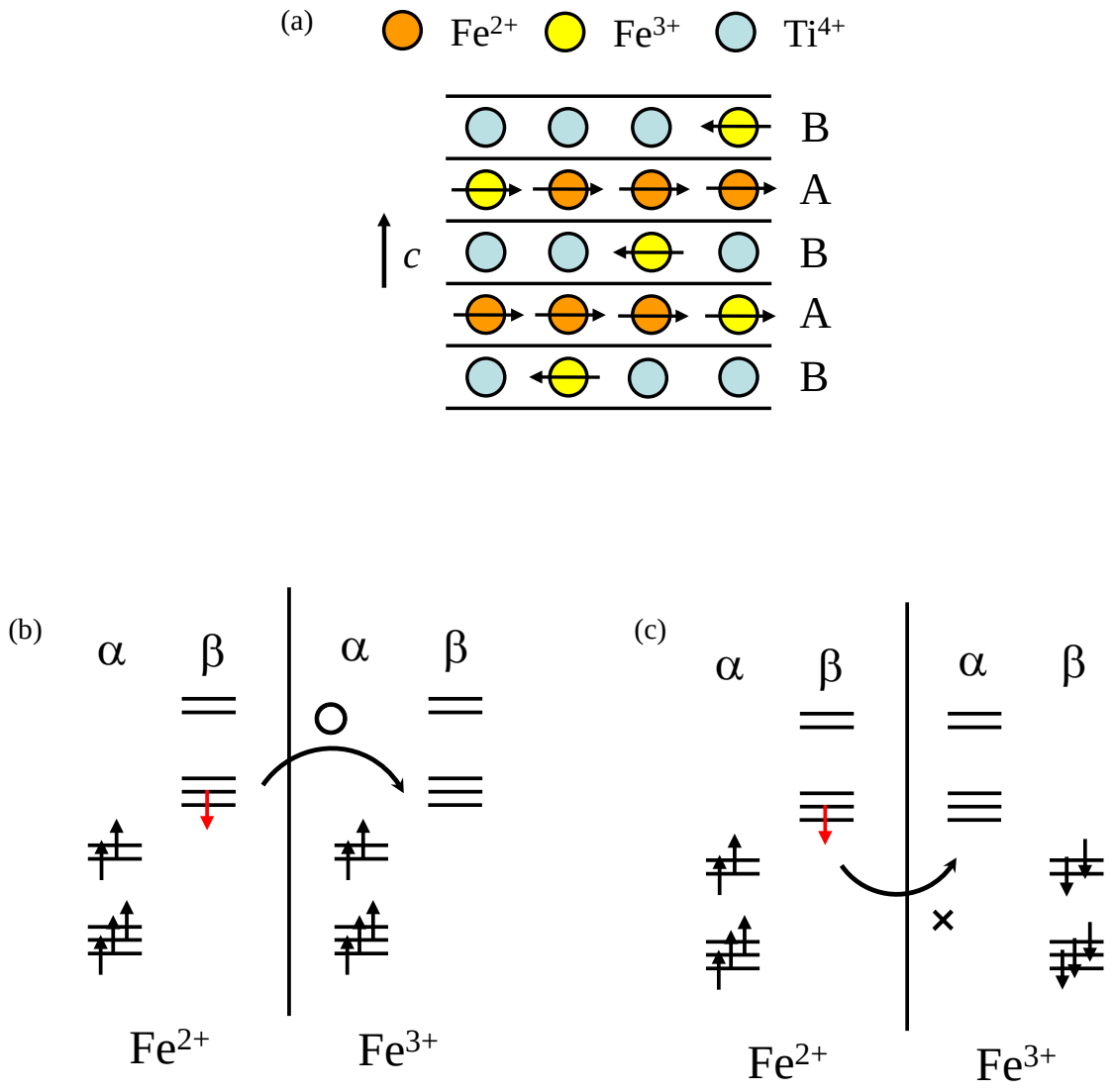

Fig. 5.12 (a) The schematic image of cation arrangement in ordered-phase of $FeTiO_3$–Fe_2O_3 solid solution. (b), (c) The schematic image of electron transfer between Fe^{2+} and Fe^{3+} when Fe^{2+} and Fe^{3+} are ferromagnetically coupled [Fig. 5.12 (b)] or antiferromagnetically coupled [Fig. 5.12 (c)].

5.5 References

1. E. Dagotto, *Science* **309**, 257 (2005).
2. J.-H. Park, E. Vescovo, H.-J. Kim, C. Kwon, R. Ramesh, and T. Venkatesan, *Nature* **392**, 794 (1998).
3. G. H. Jonker, and J. H. van Santen, *Physica* **16**, 337 (1950).
4. J. Cibert, J.-F. Bobo, and U. Lüders, *C. R. Phys.* **6**, 977 (2005).
5. Y. Ishikawa, and S. Akimoto, *J. Phys. Soc. Jpn.* **12**, 1083 (1957).
6. Y. Ishikawa, *J. Phys. Soc. Jpn.* **13**, 37 (1958).
7. W. H. Butler, A. Bandyopadhyay, and R. Srinivasan, *J. App. Phys.* **93**, 7882 (2003).
8. F. Zhou, S. Kotru, and R. K. Pandy, *Thin Solid Films* **408**, 33 (2002).
9. T. Fujii, M. Kayano, Y. Takada, M. Nakanishi, and J. Takada, *J. Magn. Magn. Mater.* **272-276**, 2010 (2004).
10. T. Fujii, M. Kayano, Y. Takada, M. Nakanishi, and J. Takada, *Solid State Ionics* **172**, 289 (2004).
11. H. Hojo, K. Fujita, K. Tanaka, and K. Hirao, *Appl. Phys. Lett.* **89**, 082509 (2006).
12. H. Hojo, K. Fujita, K. Tanaka, and K. Hirao, *Appl. Phys. Lett.* **89**, 142503 (2006).
13. H. Hojo, K. Fujita, K. Tanaka, and K. Hirao, *J. Magn. Magn. Mater.* **310**, 2105 (2007).
14. K. Tanaka, K. Fujita, S. Nakashima, H. Hojo, and T. Matoba, *J. Magn. Magn. Mater.* **321**, 818 (2009).
15. D. M. Sherman, *Phys. Chem. Miner.* **14**, 364 (1987).
16. N. C. Wilson, J. Muscat, D. Mkhonto, P. E. Ngoepe, and N. M. Harrison, *Phys. Rev. B* **71**, 075202 (2005).
17. G. Radtke, S. Lazar, and G. A. Botton, *Phys. Rev. B* **74**, 155117 (2006).
18. T. Seda, and G. R. Hearne, *J. Phys.: Condens. Matter.*, **16**, 2707 (2004).
19. B. Zhang, T. Katsura, A. Shatskiy, T. Matsuzaki, and X. Wu, *Phys. Rev. B* **73**, 134104 (2006).
20. A. Agui, T. Uozumi, M. Mizumaki, and T. Käämbre, *Phys. Rev. B* **79**, 092402 (2009).
21. http://www.geocities.jp/kmo_mma/crystal/en/vesta.html
22. R. J. Harrison, S. A. T. Redfern, and R. I. Smith, *Am. Mineral.* **85**, 194 (2000).
23. H. Bizette, and B. Tsai, *C. R. Acad. Sci.* **242**, 2124 (1956).

24. K. Ogasawara, T. Iwata, Y. Koyama, T. Ishii, I. Tanaka, and H. Adachi, *Phys. Rev. B* **64**, 115413 (2001).
25. H. Ikeno, I. Tanaka, Y. Koyama, T. Mizoguchi, and K. Ogasawara, *Phys. Rev. B* **72**, 075123 (2005).
26. H. Hojo, K. Fujita, H. Ikeno, T. Matoba, T. Mizoguchi, I. Tanaka, Y. Ikuhara, T. Nakamura, and K. Tanaka, to be submitted to *Phys. Rev. B* as "Soft X-ray Magnetic Circular Dichroism of Ilmenite-Hematite Solid Solution Epitaxial Thin Films".
27. A. K. Mukerjee, *Indian J. Phys.* **38**, 10 (1964).
28. J. Takaobushi, M. Ishikawa, S. Ueda, E. Ikenaga, J. Kim, M. Kobata, Y. Takeda, Y. Saitoh, M. Yabashi, Y. Nishino, D. Miwa, K. Tamasaku, T. Ishikawa, I. Satoh, H. Tanaka, K. Kobayashi, and T. Kawai, *Phys. Rev. B* **76**, 205108 (2007).

Summary and future work

In this thesis, for the purpose of spintronics application, high-quality $FeTiO_3$–Fe_2O_3 solid solution, that is xFeTiO$_3$·(1–x)Fe$_2$O$_3$ ($0 < x < 1$), thin films have been fabricated via pulsed laser deposition (PLD) method. Generally, atomically smooth surface of thin films is required in order to realize high-performance devices, because the rough interface between thin films seriously degrades the transport properties of materials. The lattice mismatches between $FeTiO_3$–Fe_2O_3 solid solution thin films and the substrates, α–Al_2O_3, are as large as 6.2% (in C-plane) and 7% (in A-plane), and this large lattice mismatch makes it difficult to accomplish $FeTiO_3$–Fe_2O_3 solid solution thin films epitaxially grown on α–Al_2O_3 substrates. However, I have successfully fabricated $FeTiO_3$–Fe_2O_3 solid solution thin films with atomically smooth surface on both C- and A-plane α–Al_2O_3 substrates by optimizing the deposition conditions of PLD method. I also have suggested the electrical conduction mechanism in $FeTiO_3$–Fe_2O_3 solid solution through hard X-ray photoemission spectroscopy (HX-PES) study. The results obtained by the present study are summarized as follows,

In Chapter 1, the outlines of spintronics and $FeTiO_3$–Fe_2O_3 solid solution were briefly reviewed. Especially, I focused on the tunneling magnetoresistive effect and the operating principle of magnetoresistive random access memory (MRAM), which is a key technology for a next-generation non-volatile memory. In order to achieve effective MRAM, the spin polarization of materials should be near 100%. As one of such high spin polarization materials, I have paid attention to $FeTiO_3$–Fe_2O_3 solid solution which has unique physical properties. First, its carrier type can be changed by simply varying its composition; *n*-type carrier when $x < 0.73$ and *p*-type carrier when $x > 0.73$. This ability to tune carrier type in $FeTiO_3$–Fe_2O_3 solid solution indicates that homo *p*-*n* junction device is expected to be realized by utilizing $FeTiO_3$–Fe_2O_3 thin films with different compositions. Secondly, $FeTiO_3$–Fe_2O_3 solid solution has relatively high ferrimagnetic Curie temperature (T_C), which is varied linearly with x, and T_C is higher than room temperature when $x < 0.73$. This high T_C makes $FeTiO_3$–Fe_2O_3 solid

solution a promising material for spintronics application which can operate at room temperature.

In Chapter 2, the low-temperature growth of $FeTiO_3$–Fe_2O_3 thin films on C-plane sapphire, α–Al_2O_3 (0001), substrates was shown. I demonstrated that highly crystallized thin films without deep pits could be fabricated by lowering the growth temperature from 700 ºC to 550 ºC. This low-temperature growth method is one of the directions toward the achievement of high-quality thin films suitable for device application.

In Chapters 3 and 4, I fabricated $FeTiO_3$–Fe_2O_3 thin films with atomically flat surface on α–Al_2O_3 (0001) and $(11\bar{2}0)$ (A-plane) substrates by extremely high-growth temperature higher than 850 ºC. It is particularly worth noting that the epitaxial growth of $FeTiO_3$–Fe_2O_3 thin films on α–Al_2O_3 $(11\bar{2}0)$ substrates has been realized for the first time. The atomic force microscopy study revealed that the obtained thin films possessed step-and-terrace surfaces whose one step height corresponded to one charge-neutral unit. I consider that the thin films were grown by Domain-Matching Epitaxy (DME) growth, where the integer multiple of lattice constants of thin film and substrate is matching across the interface and the lattice strain is relaxed in the initial stage of the thin film growth. I also carried out cross-sectional high-resolution transmission electron microscope study for the interface between thin film and substrate in order to investigate the DME mechanism in $FeTiO_3$–Fe_2O_3/α–Al_2O_3 system. I confirmed that the dislocation cores existed across the interface with a regular interval which was equal to unit domain length of $FeTiO_3$–Fe_2O_3. The results in Chapters 3 and 4 will be effectively applied to the growth of other thin film and substrate systems having quite large lattice mismatch.

In Chapter 5, in order to investigate the electronic structure and electrical conduction mechanism of $FeTiO_3$–Fe_2O_3 solid solution, I conducted the HX-PES measurements on $FeTiO_3$ and $FeTiO_3$–Fe_2O_3 samples. It was revealed that the valence band structures of both $FeTiO_3$ and $FeTiO_3$–Fe_2O_3 solid solution consisted of strongly mixed Fe 3*d* and O 2*p* components. A peak shift was observed in the valence band spectra of those samples, whereas such a shift was not observed in the Fe 2*p*, Ti 2*p* and O 1*s* core-level spectra. I consider that the observed peak shift is due to the variation in the electron correlation of Fe 3*d* components brought about when $FeTiO_3$ forms solid solution with α–Fe_2O_3. I have proposed that insulator $FeTiO_3$ is converted into semiconductor accompanied by the forming of $FeTiO_3$–Fe_2O_3 solid solution due to the

intermixture of Fe^{2+} and Fe^{3+} which reduces the electron correlation, and that the electron transfer between Fe^{2+} and Fe^{3+} within the C-plane is the dominant electrical conduction mechanism for $FeTiO_3$–Fe_2O_3 solid solution.

In the future, with utilizing the results obtained by this study, the development of spintronics device based on $FeTiO_3$–Fe_2O_3 solid solution will be expected. For example, homo *p*-*n* junction device with sharp interface is expected to be realized by growing $FeTiO_3$–Fe_2O_3 thin film with the growth temperature of 550 ºC (as introduced in Chapter 2) on the thin film grown on α–Al_2O_3 substrate with the growth temperature of higher than 850 ºC (as introduced in Chapter 3). The extremely high-temperature growth of bottom thin film will lead to atomically flat surface and the low-temperature growth of upper thin film will prevent the intermixture of constituent ions in the two thin films at their interface. The combination of these different thin film growths will make it possible to achieve the sharp interface suitable for spintronics device application.

List of publications

Chapter 1.

1. "Development of Ferromagnetic Oxide Semiconductor Thin Films Towards Spintronics Applications"
   Koji Fujita, Hajime Hojo, Tomohiko Matoba, Kazuyuki Hirao, and Katsuhisa Tanaka
   Materials Science & Technology Conference and Exhibition (MS&T'08) (2008), pp.134-143.

2. "Magnetic properties of disordered ferrite and ilmenite-hematite thin films"
   Katsuhisa Tanaka, Koji Fujita, Seisuke Nakashima, Hajime Hojo, and Tomohiko Matoba
   Journal of Magnetism and Magnetic Materials **321**, 818-821 (2009).

Chapter 2.

3. "Low-temperature growth of highly crystallized $FeTiO_3$–Fe_2O_3 solid solution thin films with smooth surface morphology"
   Tomohiko Matoba, Koji Fujita, Shunsuke Murai, and Katsuhisa Tanaka
   Journal of Physics: Conference Series **200**, 062011 (2010).

Chapter 3.

4. "Ilmenite-hematite solid solution thin films with atomically smooth surface grown on C-plane sapphire substrates"
   Tomohiko Matoba, Koji Fujita, Shunsuke Murai, and Katsuhisa Tanaka
   To be submitted to *Applied Physics Express* (2013).

Chapter 4.

5. "High-quality ilmenite-hematite solid solution thin films grown on A-plane sapphire substrates"
   Tomohiko Matoba, Koji Fujita, Shunsuke Murai, and Katsuhisa Tanaka
   To be submitted to *Applied Physics Express* (2013).

Chapter 5.

6. "Soft x-ray magnetic circular dichroism of ilmenite-hematite solid solution epitaxial thin films"
   Hajime Hojo, Koji Fujita, Hidekazu Ikeno, Tomohiko Matoba, Teruyasu Mizoguchi, Isao Tanaka, Yuichi Ikuhara, Tetsuya Nakamura, and Katsuhisa Tanaka
   Submitted to *Physical Review B* (2013).

7. "Electronic structure of ilmenite and ilmenite-hematite solid solution using hard X-ray photoemission spectroscopy"
   Tomohiko Matoba, Koji Fujita, Shunsuke Murai, and Katsuhisa Tanaka
   Journal of the Japan Society of Powder and Powder Metallurgy (2013), in press.

Other publications

8. "Enhancement of Optical Birefringence in Tellurite Glasses Containing Silver Nanoparticles Induced via Thermal Poling"
   Shunsuke Murai, Ryosuke Hattori, Tomohiko Matoba, Koji Fujita, and Katsuhisa Tanaka
   Journal of Non-Crystalline Solids **357**, 2259 (2011).

9. Plasmonically Controlled Lasing Resonance with Metallic-Dielectric Core-Shell Nanoparticles
   Xiangeng Meng, Koji Fujita, Shunsuke Murai, Tomohiko Matoba, and Katsuhisa Tanaka
   Nano Letters **11**, 1374 (2011).

10. “Oblique angle deposition of zinc oxide on silver nanoparticles for plasmonically enhanced optical birefringence”

    Shunsuke Murai, Takuya Komine, Tomohiko Matoba, Christopher Tobias Nelson, Xiaoqing Pan, Koji Fujita, and Katsuhisa Tanaka

    To be submitted to *Journal of the Ceramic Society of Japan* (2013).

Acknowledgement

The present thesis has been carried out under the direction of Professor Katsuhisa Tanaka at Graduate School of Engineering, Kyoto University. First of all, the author wishes to express his sincere gratitude to Professor Katsuhisa Tanaka for his continuous encouragement and valuable advice all through the duration of the present work.

The author is also grateful to Professor Kazuyuki Hirao and Professor Toshinobu Yoko for guidance and discussion in preparation of the present thesis. The author also appreciates Associate Professor Koji Fujita for his informative discussion, helpful advice, and sincere supports.

The author also thanks Dr. Shunsuke Murai, Dr. Hajime Hojo, Dr. Xiangeng Meng, Dr. Kazuma Kugimiya, Dr. Hirofumi Akamatsu, Dr. Hideaki Murase, and Dr. Yanhua Zong, for helpful assistance. Experimental supports for hard X-ray photoemission spectroscopy measurements by Dr. Eiji Ikenaga are greatly acknowledged. The author would like to thank Professor Akio Ito and Associate Professor Hidetsugu Tsuchida for RBS measurements.

The author also thanks Mr. Hideo Murakami, Mr. Naoto Imada, Mr. Ryosuke Hattori, Mr. Naoki Wakasugi, Mr. Naohiro Takemoto, Mr. Yuya Maruyama, Mr. Yoshiro Kususe, Mr. Junya Morishita, Mr. Takahiro Kawamoto, Mr. Ryuichiro Yasuhara, and Mr. Masaharu Watanabe for their experimental supports and fruitful discussions.

Hearty thanks are made to all the students of Hirao laboratory and Tanaka laboratory for their collaboration and everyday activities. Especially his colleagues, Ms. Chie Ito, Mr. Satoshi Oku, Mr. Shigehiro Fukuoka and Mr. Yutaka Fujimoto contributed to his happiest time. The author also would like to thank Professor Xiaoqing Pan and the members of his research group at the Department of Materials Science and Engineering, the University of Michigan. The author is grateful for “Young Researcher Overseas Visits Program for Vitalizing Brain Circulation” of Japan Society for Promoting Science.

Finally, the author would like to express his sincere gratitude to his parents Koichi Matoba

and Kazuko Matoba, for their understanding, supports, and hearty encouragements.

Kyoto, 2013 Tomohiko Matoba